

**2D Squeezing-flow of a Non-Newtonian Fluid Between Collapsed Viscoelastic Walls:
Numerical Simulations**

By

Copyright 2013

Zouhair Talbi

Submitted to the graduate degree program in Bioengineering and the Graduate Faculty of the
University of Kansas in partial fulfilment of the requirements for the degree of Master of
Science.

Chairperson Dr. Sarah L. Kieweg

Dr. Elizabeth A. Friis

Dr. Sara E. Wilson

Date Defended: May 30, 2013

The Thesis Committee for Zouhair Talbi

certifies that this is the approved version of the following thesis:

2D Squeezing-flow of a Non-Newtonian Fluid Between Collapsed Viscoelastic Walls:
Numerical Simulations

Chairperson Dr. Sarah L. Kieweg

Date approved: May 30, 2013

Abstract

This study is part of a broader research plan to design and develop microbicides to prevent against HIV (Human Immunodeficiency Virus) and other sexually transmitted infections (STIs). A microbicide is a topical compound that contains active ingredients to protect against STIs. The active ingredients are suspended in a delivery vehicle, such as creams and polymeric gels. The efficacy of a microbicide gel depends on the extent of the spreading, the amount of the epithelial surfaces coated, and the retention on the vulnerable epithelial surfaces. The effectiveness of a microbicide gel to coat and adhere to the epithelium is affected by several factors, such as the rheological properties of gel, gravity, biomechanical properties of the vaginal tissue, vaginal geometry, effects of the neighbouring tissues, and dilution.

This thesis presents an engineering approach to help understand the impact of the viscoelastic characteristics of the vaginal tissue on the spreading of different formulations of a microbicide gel. This study focuses on the relative effects of the tissue biomechanical properties and gravity on the spreading behaviour of a gel with different rheological properties. In this study, a numerical model was developed to investigate the flow of the gel under different conditions.

A 2D numerical flow model (1D spreading) was developed to simulate the flow under the influence of gravity and the squeezing forces due to the biomechanical properties of the vaginal tissue. The gel was modelled as a non-Newtonian fluid using the power-law constitutive model. The viscoelastic characteristic of the soft tissue was represented by the Voigt model. This study is an initial attempt to incorporate the viscoelastic characteristics of the vaginal tissue in the development of a microbicide drug delivery vehicle.

The results of the numerical simulations were analysed based on a series of coupling parametric studies. Based on the results of the parametric studies, the tissue viscoelastic parameters have a different impact on the flow behaviour of the gel depending on the relative magnitudes of the tissue elastic and viscous components. For a higher tissue viscous-coefficient, the tissue viscous effect resulted in less spreading and as the tissue elasticity increased, the impact of the tissue viscous component diminished.

The impact of the tissue viscous component depended on the fluid rheological properties. The impact of the tissue viscous-coefficient was more noticeable at a lower fluid consistency and at a higher fluid shear-thinning index. Once applied to the vaginal canal the gel is expected to dilute after it mixes with vaginal fluids. The dilution of the gel would decrease its consistency and increase its shear-thinning index and consequently increase the impact of the tissue viscous component on the spreading of the gel.

In conclusion, the results of this study strongly suggest the need to determine the biomechanical properties *in vivo*. The importance and the significance of measuring the biomechanical properties are two fold; 1) the characterization of the tissue viscoelastic properties would help in developing more accurate and more relevant theoretical models and 2) knowing the biomechanical properties of the vaginal tissue would play a key role in validating the numerical studies and in evaluating the performance of microbicidal gels in a clinical setting. The results of this study would ultimately serve as a tool in designing and optimizing microbicidal gels.

Acknowledgement

I want to thank my advisor, Dr. Sarah L. Kieweg, for her support and continuous guidance during my research. I would also like to thank my committee, Dr. Elizabeth A. Friis and Dr. Sara E. Wilson, for their time and input.

Additionally, I would like to thank my parents Halima Hadni and Abdurrahman Talbi for their love and encouragement. My wife, Sarah, who always believed in me and encouraged me through it all.

I would also like to thank Dr. Kieweg's research group members: Bin Hu, Anwar Md Rajib, Todd McDonald, Mark Pacey, Thora Whitmore, and Derek Taylor for their suggestions and exchange of ideas in the lab.

This work was funded by NIH R21/R33 AI082697. The KU ITTC high performance computing resources were funded by NSF MRI 0821625.

Table of Contents

Abstract.....	iii
Acknowledgement	v
List of Figures	viii
List of Tables	ix
Chapter 1: Introduction	1
1.1 Introduction:	1
1.2 Guide to thesis document.....	3
Chapter 2: Background	5
2.1 Vaginal anatomy and vaginal tissue properties	6
2.2 Soft tissue viscoelastic characteristics	7
2.2.1 Viscoelasticity modelling.....	7
2.2.2 Review of relevant literature for soft tissue viscoelasticity.....	9
2.2.3 Microbial gels and vaginal tissue properties	14
Chapter 3: The effects of the tissue viscoelastic properties on the flow of a microbicidal gel	17
3.1 Introduction	17
3.2 Methods.....	21
3.2.1 Problem formulation	21
3.2.2 Numerical method and model validation	25
3.2.3 Parametric study method	26
3.3 Results and discussion	28
3.3.1 The impact of elastic and viscoelastic boundary	28
3.3.2 The influence of the tissue viscous-coefficient η on the flow of the fluid with varying rheological properties.....	32
3.3.3 Dimensionless analysis.....	37
3.4 Conclusions	41
4. Model validation and additional results	46
4.2 Convergence study.....	46
4.2 Conservation of mass check.....	49
4.3 Numerical Methods	50
4.3.1 Discretization: <i>the theta-method (the θ-method)</i>	51
4.3.2 Backward Euler method vs. Crank-Nicolson method	55
4.4 Additional results	56
4.4.1 The difference between the viscoelastic and the elastic properties of the tissue on the flow behaviour of the fluid	57

4.4.2 The influence of the tissue viscous component on the flow of the fluid with different consistencies	67
4.4.3 The influence of the tissue viscous component on the flow of the fluid with different shear-thinning indices	70
4.4.4 Non-dimensional analysis	77
Chapter 5: Conclusions, limitations, and future work	78
Appendices	81
Appendix A. Examples of spreading profiles with different tissue and fluid properties	81
Appendix B. Examples of the change in the maximum length with changing boundary properties for various fluid properties.....	84
Appendix C. The influence of the tissue viscous component on the fluid with different consistencies	85
Appendix D. The influence of the tissue viscous component on the fluid with different shear-thinning indices	86
Appendix E. Derivation of the evolution equation (in the dimensional and non-dimensional forms) with the Ellis constitutive model	89
References	91

List of Figures

Figure 3.1: Initial geometry of the bolus and tissue. The bolus is symmetrical about the vertical line at all times. The pressure from the boundary and gravity are the driving forces of the flow.	22
Figure 3.2: The Voigt model for viscoelastic materials	23
Figure 3.3: Example of flow profiles of a power-law fluid ($n = 0.6, m = 100 \text{ P}\cdot\text{s}^{n-1}$) with two different sets of tissue elastic E and viscous η components illustrating the difference in the impact of the elastic model and the viscoelastic model of the tissue.	30
Figure 3.4: Example of change in the spreading length of a power law fluid ($n = 0.6, m = 300 \text{ P}\cdot\text{s}^{n-1}$) with various values of tissue elasticity E and viscous-coefficient η	31
Figure 3.5: (a) – (b) The change in the maximum spreading length L_{max} of the bolus for various values of consistency m , tissue viscous-coefficient η and with different combinations of tissue elasticity E and fluid’s shear-thinning index n	33
Figure 3.6: (a) – (b) the change in the maximum bolus height h_{max} as a function of the consistency m for different shear-thinning indices and tissue properties (viscous-coefficient η and elasticity E).....	34
Figure 3.7: (a) – (b) The change in the maximum spreading length L_{max} of the bolus with various fluid shear-thinning index n , tissue viscous-coefficient η for different combinations of tissue elasticity E and fluid consistency m	36
Figure 3.8: (a) - (b) The dimensionless spreading length due to the boundary elasticity only ($Z = 0$) as a function of $W = T\rho gxE$ (starting with the lowest value $W = 0.00294$) at different dimensionless time t relative to the dimensionless length at the initial condition ($t = 0$), for different fluid shear-thinning index n . L_{max} is the maximum dimensional length and H is the bolus initial maximum height.	39
Figure 3.9: (a) – (b) The dimensionless spreading length (L_{max}/H) at dimensionless time $t = 5000$ as function of the variable Z for two different values of W and different cases of fluid shear-thinning index. $Z = \eta E E H T m 1 n, W = T\rho gxE$	41
Figure 4.1: (a) – (b) The convergence results with different combinations of tissue viscoelastic parameters (E and η) and fluid’s properties (shear-thinning index n and consistency m) elasticity.	47
Figure 4.2: The conservation of mass of the fluid-bolus over the computational time.....	50

List of Tables

Table 2.1: The constitutive equations of the standard linear viscoelastic models, where the E is the modulus of elasticity, η is the viscous-coefficient, σ and ε are the mechanical stress and strain, respectively (Adapted from [28]).....	8
Table 2.2: A selected summary of values of the viscoelastic parameters (E : Modulus of elasticity, and η : Viscous-coefficient) of various materials with the method of testing or application and model used for representation	13
Table 3.1: The constant parameters of the numerical model	27
Table 3.2: Maximum percentage change in the maximum length L_{max} with tissue viscous-coefficient $\eta = 10 \text{ P}\cdot\text{s}^{-1}$ for different tissue elasticity E and all combinations of fluid's shear-thinning index n and consistency m	32
Table 4.1: Spatial mesh refinement for a power-law fluid with shear-thinning $n = 0.8$ and consistency $m = 400 \text{ P}\cdot\text{s}^{-1}$	48
Table 4.2: Spatial mesh refinement for a case of Newtonian fluid ($n = 1$) with a consistency $m = 600 \text{ P}\cdot\text{s}^{-1}$	48
Table4.3: Computational time required with different mesh resolutions.....	49
Table4.4: Comparison between Backward-Euler method and the Crank-Nicolson method	55

Chapter 1: Introduction

1.1 Introduction:

This study is part of a broader research plan to design and develop effective gel formulations as drug delivery systems that would act as active barriers against HIV and other sexually transmitted infections (STIs). Such drug delivery systems are commonly known as microbicides. Microbicides are agent-containing compounds and preparations (e.g. gels, creams, films, suppositories, or foams) designed to be locally deployed to either the vaginal or the rectal areas in order to prevent HIV and other STIs infections [1, 2]. Anti-STIs microbicides are delivered with the goal to cover and coat the epithelial surfaces to prevent physical interactions between the pathogens and vulnerable epithelium, and at the same time to destroy the pathogens or inhibit potential infections.

It was reported that by the end of 2011, 34 million people were living with HIV and that 1.7 million individuals died with causes linked to AIDS during the same year [3]. Even though the number of people acquiring HIV has been decreasing in previous years, 2.5 million individuals contracted HIV in 2011[3]. Therefore, HIV continues to be a global pandemic. Over half of newly infected adults are women [4], and the majority of these women live in the developing world [5]. About 70% of the infected women live in sub-Saharan Africa [6]. Due to gender inequality, women in many countries are unable to adjudicate the use of condoms [7]. Unlike condoms, microbicides are self-administered, making microbicides convenient methods of prevention against HIV and other STIs, especially for women who can't control or negotiate the use of condoms. The current absence of an effective HIV vaccine makes the development of an effective and a safe microbicide essential [4]. Microbicides have become preferred methods in providing women with protection against HIV transmission [5]. However, there isn't a universal microbicide that is approved for general public use. Microbicides are expected to remain an important mean of

protection against HIV, even after the discovery of an effective HIV vaccine, as they perform complementary roles to combat HIV on a global platform [8]. Therefore, there is an evident and urgent need in designing and developing microbicides against HIV primarily, and other STIs in general.

This study is part of an engineering approach to address the need to design and develop effective microbicides. The efficacy of a microbicide gel is measured by the extent of the spreading and the retention of the gel over epithelial surfaces. By developing mathematical models and performing numerical simulations, we were able to describe and predict the flow behaviour of microbicides with different properties and under different flow conditions.

The ultimate goal of our research is to develop reliable and effective microbicides as drug delivery vehicles. In order to achieve this goal, it is of great importance to recognize and identify the critical factors that would affect gel flow and incorporate these factors into our models.

The main objective of this study is to examine and evaluate the effects of the vaginal tissue viscoelasticity, especially the degree of impact of the tissue viscous component on the flow of a microbicide gel. It is expected that the viscoelastic boundaries would have different effects on the flow of a gel compared to the effects of pure elastic boundaries, and therefore it is anticipated that the flow and spreading behaviour of a gel between viscoelastic boundaries would be different than the flow behaviour between pure elastic boundaries.

The following research questions were addressed in this work:

- i. Is there a difference in impact between the linear viscoelastic and the pure linear elastic tissue on the overall spreading behaviour of a microbicidal gel?

And if so:

- ii. How does the impact of the tissue viscous component depend on the tissue elasticity?
- iii. How does the tissue viscous component influence the flow of the fluid with different consistencies?
- iv. How does the tissue viscous component influence the flow of the fluid with different shear-thinning indices?

1.2 Guide to thesis document

Chapter 2: Background

This chapter provides first, a brief introduction about vaginal drug delivery systems, with an extra focus on vaginal microbicidal gels. Then a description of the human vaginal anatomy is presented and discussed in terms of size, shape, biological composition of the vaginal tissue and the importance of the biomechanical properties of the vaginal tissue in the field of microbicidal gels. Finally, an introduction to soft tissue viscoelasticity properties and viscoelasticity modelling is presented.

Chapter 3: The effects of the tissue viscoelastic properties on the flow of a microbicidal gel

This chapter was written in a manuscript-like format. The introduction provides background information related to vaginal microbicidal gels. The method section includes the mathematical derivation steps to formulate the flow model in addition to the description of the parametric study method. In the results and discussion section, major findings are presented and discussed. Finally, in the last section conclusions of the parametric study

results are presented and the limitations of the model as well as direction of future work are discussed.

Chapter 4: Model validation

This chapter provides detailed description and discussion of the convergence study and of the mass-conservation check. The two methods were used to verify and validate our mathematical model.

Chapter 5: Conclusions, limitations and future work

This chapter provides a summary of this study's overall conclusions. The limitations of and the challenges with the current model are also presented and discussed. Additionally, this chapter provides potential directions for future work in the field of microbicide delivery vehicles.

Chapter 2: Background

Since ancient times, the vagina has been known to be a drug delivery route, and more recently, this route of delivery has been rediscovered for delivery of therapeutic substances [9]. Several recent studies considered various drug release methods using the female genital tract as the primary route of delivery. The release modes include intravaginal ring [10-12], mucoadhesive polymers [13, 14], and wall coating microbicides [15-18], which are the focus of our research.

The efficacy of a microbicide gel depends greatly on the extent of the spreading and the retention of the gel over the coated epithelial surfaces. In the vaginal tract, a microbicide gel is subjected to gravitational effects as well as squeezing forces, which are directly related to the biomechanical properties of the tissue [15]. In addition to the biomechanical properties of the vaginal tissue, the rheological properties of a microbicide gel play an important role in the overall performance of a gel as a drug delivery vehicle.

In a previous study, completed by S. Karri, a former member of Dr. Kieweg's research group, the combined effects of gravity and vaginal tissue elasticity on the flow of various gel formulations were investigated [19]. In the current study, the investigation of the impact and the influence of the tissue mechanical properties on the gels spreading behaviour was expanded by considering the tissue's viscoelasticity rather than just its elasticity. The vaginal tissue, like many other human soft tissues, is anticipated to exhibit viscoelastic characteristics [20]. Therefore, it was important to investigate the potential effects of the viscoelastic parameters of the tissue on the spreading of various formulations of microbicide gels. This study was a first step in incorporating the viscoelastic characteristics of the vaginal tissue in a microbicide gel delivery system.

2.1 Vaginal anatomy and vaginal tissue properties

The human female genital tract in its relaxed state is described as a thin-walled, fibromuscular, asymmetric, collapsed tube that can easily be dilated [21, 22]. The shape of the vaginal tube doesn't conform to any known conventional geometric shape, yet the cross section of the vagina has been generally represented as an "H" shape [21]. In terms of size, the length of the human vagina can range between 7-10 cm with a wall thickness between 0.5 – 2.0 cm [15, 22].

The human vaginal tissue is comprised of four major layers: (i) the vaginal mucosa, a region of stratified epithelial tissue; (ii) the vaginal submucosa, a vascularised connective tissue region; (iii) the muscularis layer, a region comprised of smooth muscle; and (iv) the adventitia, which consists of loose connective tissue [23]. The composition and the geometry of the female genital tract are factors that strongly affect the biomechanical properties of the vaginal tissue [24].

Describing and characterizing the behaviour of soft biological tissues including vaginal tissue is essential in the field of biomechanics [25]. For a microbicide delivery vehicle, such as the one considered in this study, the biomechanical properties of the soft tissue are of great importance. The vaginal walls compliance, in other words the walls elasticity, and the pressure from the neighbouring tissues are expected to have a significant impact on the spreading and distribution of a microbicide gel [26]. In fact, Szeri *et al.* [15] and Karri [19] showed that the tissue elasticity has a substantial influence on the spreading extent on the flow of a microbicide gel. Since other experimental studies have characterized the vaginal tissue as a viscoelastic soft tissue [20, 27], this study addresses the need to consider the tissue viscoelasticity and not only elasticity.

2.2 Soft tissue viscoelastic characteristics

2.2.1 Viscoelasticity modelling

A viscoelastic solid is a material that possesses the following three characteristics: *(i)* stress relaxation, which describes the decrease in stress when the material is subjected to a constant strain; *(ii)* creep, the ability to continuously deform under constant stress; *(iii)* hysteresis, a phenomenon that describes the change in the stress-strain relationship after a material undergoes a cyclic loading [28].

The viscoelastic features of a solid can generally be categorized as linear or non-linear characteristics. These characteristics are described and represented using either mechanical or mathematical models. The representations of the mechanical models vary from simple linear and non-linear to complex linear and non-linear models. The most common simple models are known as the three standard linear viscoelastic models which include the Kelvin model, the Maxwell Model, and the Voigt model (also known as the Kelvin-Voigt model). Complex mechanical models are generally comprised of a combination of one or more of the simple models. Complex mechanical models include models such as the Burger's model, the generalized n-element Voigt model, and the generalized n-element Maxwell model [28]. The representations of the mathematical models are based on the strain-energy function, which is often used for materials with complex behaviour.

The mechanical models are comprised of various combinations of springs representing the elasticity of the material, and dashpots representing the viscous-coefficient of the material. With the mechanical models, the stress-strain relationship for a given material is explicitly expressed in terms of the modulus of elasticity E and the coefficient of viscosity η . For instance, the strain-stress constitutive equations for the standard linear viscoelastic models are defined in Table 2.1 [28].

	Mechanical model	Stress-Strain relationship
Voigt		$\sigma = E\varepsilon + \eta\dot{\varepsilon}$
Maxwell		$\dot{\varepsilon} = \frac{\dot{\sigma}}{E}\varepsilon + \frac{\sigma}{\eta}$
Kelvin		$\sigma + \frac{\eta}{E_1}\dot{\sigma} = E_0\varepsilon + \eta\left(1 + \frac{E_0}{E_1}\right)\dot{\varepsilon}$

Table 2.1: The constitutive equations of the standard linear viscoelastic models, where the E is the modulus of elasticity, η is the viscous-coefficient, σ and ε are the mechanical stress and strain, respectively (Adapted from [28]).

With the strain-energy function however, the stress-strain relationship is given by:

$$S_{ij} = \frac{\partial(\rho_0 W)}{\partial E_{ij}} \quad (2.1)$$

where S_{ij} represents stress, E_{ij} represents strain, and $(\rho_0 W)$ represents the strain-energy function per unit of mass for a given material [28, 29].

In this study, we chose to model the vaginal tissue with the Voigt model for several reasons. First, this basic model was an initial step in investigating the effects of the

viscoelastic features of the vaginal tissue on the flow behaviour of microbicidal gels. Secondly, this model provided a convenient way to incorporate the viscoelastic parameters (i.e. modulus of elasticity E and viscous-coefficient η) of the tissue into our flow model. The constitutive equation of the Voigt model as given in Table 2.1 allowed us to write the stress-strain relationship as a pressure term in the derivation of the equation that governs the flow (see section 3.2.1). Additionally, this approach allowed us to directly compare the findings of this study to the results of our group's previous study, in which the vaginal tissue was modelled as a pure elastic medium, completed by Karri [19].

2.2.2 Review of relevant literature for soft tissue viscoelasticity

It is well known that most biological tissues exhibit viscoelastic characteristics. These characteristics are generally non-linear, anisotropic, and time-dependent [28]. Therefore, characterizing the biomechanical properties and modelling human tissue is a challenging task [30]. There are numerous studies and investigations that describe the biomechanical properties of soft tissues in general, but only a few studies focus on characterizing the viscoelasticity of the human vaginal tissue. In fact, research in the field of vaginal biomechanics is limited [11].

Many biological tissues are better represented with complex non-linear mechanical models or with strain-energy function based models, because they describe and capture the viscoelastic characteristics of these tissues more accurately. Nonetheless, simple mechanical models, mainly the standard linear viscoelastic models, are extensively used to study and investigate soft tissue response under specific loading conditions and over certain parameter ranges (e.g. [25, 31-35]).

Current studies and investigations to characterize and/or incorporate the viscoelastic characteristics of biological tissues involved a variety of experimental setups, materials, and theoretical models. According to Kiss *et al*, the published data vary with the different

methods and approaches used for biological soft tissue characterization [30]. Due to the limited literature and data related to the biomechanics of the human vaginal tissue, we considered studies and investigations that focused on the viscoelasticity of soft tissue in general, including animal tissue. Additionally, we considered tissue-mimicking materials.

In the following literature review, we describe and present various experimental methods and theoretical models utilized in investigating soft tissue viscoelastic characteristics. However, for the theoretical models we focus mainly on studies in which the basic mechanical viscoelastic models were considered since we chose to represent the vaginal tissue as a Voigt-body in our flow model.

When considering the viscoelastic properties of soft tissue either *in vivo* or *in vitro* the viscoelastic properties are generally represented by either mechanical models (spring-dashpot arrangements) or by mathematical models (strain function based formulations). These models can be linear or non-linear and are used to model the behaviour of a viscoelastic material under a specific condition or to fit experimental data for a given material. For instance, Anssari *et al.* determined the viscoelastic properties of porcine aortic valve *in vitro*, in the circumferential and in the radial directions, under tensile elongation. They successfully fitted the experimental data to the Voigt model and reported the viscoelastic parameters at different strain rates [36]. Similarly, Kiss *et al.* studied canine liver viscoelastic response *in vitro* using the Voigt model to fit the experimental data obtained by performing a series of compressive tests at different frequencies [30].

Several studies, involving *in vivo* experiments to measure and examine soft tissue viscoelasticity, also relied on mechanical viscoelastic models to study tissue viscoelasticity and fit experimental data. For example, Sack *et al.* determined the viscoelastic response of bulk human brain *in vivo* using magnetic resonance elastography (MRE). Their experimental data were fitted to the Voigt model [35]. Similarly, Klatt *et al.* fitted experimental data

collected *in vivo* using MRE on the brain and liver of several human subjects. The data collected for the living tissues were fitted to several mechanical models including the Maxwell and Voigt models [37]. Boyer *et al.* also used the Voigt model to fit data which was collected *in vivo* and obtained by subjecting human skin to a constant indentation for a range of frequencies [31].

In addition to using mechanical models for data-fitting with the purpose of characterizing tissue viscoelasticity properties, mechanical models are also selected to represent the viscoelastic behaviour of a given tissue under certain loading conditions. For instance, Canic *et al.* incorporated the viscoelasticity of the artery walls in a pulsatile blood flow model by representing the artery with the Voigt model to capture the stress-strain response of the artery walls [34]. Similarly, Alastruey *et al.* utilized the Voigt model to incorporate the viscoelasticity of artificial arteries in the simulation of pulse wave propagation in order to compare the results of the simulation to their experimental data [38]. Likewise, Wang *et al.* used the Voigt model to represent the viscoelasticity of tissue in a simulation model. They incorporated the tissue of human finger as a Voigt body in a finite element model to simulate the response of the finger model under different conditions of indentation [39].

Besides studying the mechanical properties of soft biological tissues, numerous studies explored soft tissue-mimicking materials, known as phantoms, and their viscoelastic properties to develop and optimize measurement devices and techniques associated with tissue viscoelasticity characterization. Recently, a study by Leclerc *et al.* considered phantom samples to optimize magnetic resonance elastography (MRE) techniques for *in vivo* investigations of living organs and other tissues [33]. The phantoms were represented by three simple mechanical models and subjected to compressive loads using shear waves to determine the viscoelastic parameters for each model [33]. Previously, Girnyk *et al.* also used

tissue-mimicking materials to replicate tissue properties. They applied acoustic radiation to generate pressure on a gelatine phantom and on animal soft tissue samples. They proposed an algorithm to reconstruct the elasticity and viscous parameters of soft tissue based on “acoustic radiation force-based methods.”[40]

As mentioned before, the viscoelasticity of a material can be represented by either a mechanical model or by a strain-energy function. Various studies made use of the strain-energy function concept to predict the viscoelastic behaviour of soft tissues. For instance Haslach derived an empirical evolution model able to represent creep as well as stress relaxation of non-linear viscoelastic biological materials using maximum strain-energy dissipation [32]. Likewise, Vena *et al.* employed the strain-energy function concept to derive a constitutive model able to predict the non-linear response of soft tissues [41]. Also, Pena *et al.* proposed a viscoelastic model based on the strain-energy function to represent the viscoelastic properties of human vaginal tissue using the results of uniaxial tensile tests performed on excised human vaginal tissue specimens [20]. The viscoelasticity data reported were the parameters of the finite strain anisotropic visco-hyperelastic model, in which the elasticity and viscous parameters are not differentiated [20]. Therefore, the data are not applicable to the viscoelastic mechanical models, since the mechanical models require distinct parameter values for the elasticity and viscous components.

To the best of our knowledge, there are no studies in which the vaginal tissue viscoelasticity was modelled by either a simple or a complex mechanical model. Therefore, no data are available on the viscoelastic parameters for such models, and the data presented in Table 2.2 from the summarized literature for biological soft tissues and tissue-mimicking materials inform our selection of the values used in this study for the viscoelastic parameters.

Tissue/ phantom	Source	Viscoelastic Parameters	Model	Method	Ref.
Liver	Animal	$E=5.5\text{kPa}$, $\eta=13\text{ Pa}\cdot\text{s}$	Kelvin–Voigt	Elastography	Kiss <i>et al.</i> [30]
Aortic valve	Animal	<i>Circumferential</i> : $E=20.55\text{ MPa}$, $\eta=675.06\text{MPa}\cdot\text{s}$ <i>Radial</i> : $E=0.75\text{ MPa}$, $\eta=49.12\text{ MPa}\cdot\text{s}$	Kelvin–Voigt	Tension	Anssari <i>et al.</i> [36]
Brain	Human	$E=1.17\text{kPa}$, $\eta=3.1\text{ Pa}\cdot\text{s}$	Voigt	Elastography	Sack <i>et al.</i> [35]
Gelatine Phantom	-	$E=3.24\text{ kPa}$, $\eta=1.84\text{ Pa}\cdot\text{s}$ $E=4.48\text{ Pa}$, $\eta=18.09\text{ Pa}\cdot\text{s}$ $E_1=3.23\text{kPa}$, $E_2=3.23\text{kPa}$, $\eta=1.18\text{ Pa}\cdot\text{s}$	Voigt Maxwell Zener	Elastography	Leclerc <i>et al.</i> [33]
Lung	Animal	$E=7.99\text{kPa}$, $\eta=10.37\text{Pa}\cdot\text{s}$	Voigt	Shear waves (pressure)	Zhang <i>et al.</i> [42]
Brain	Human	$E=2.28\text{kPa}$, $\eta=15.1\text{Pa}\cdot\text{s}$ $E=1.81\text{kPa}$, $\eta=2.9\text{Pa}\cdot\text{s}$ $E_1=0.84\text{kPa}$, $E_2=2.03\text{kPa}$, $\eta=6.7\text{Pa}\cdot\text{s}$	Maxwell Voigt Zener	Elastography	Klatt <i>et al.</i> [37]
Liver	Human	$E=2.52\text{kPa}$, $\eta=21.3\text{Pa}\cdot\text{s}$ $E=2.09\text{kPa}$, $\eta=2.8\text{Pa}\cdot\text{s}$ $E_1=1.36\text{kPa}$, $E_2=1.86\text{kPa}$, $\eta=5.5\text{Pa}\cdot\text{s}$	Maxwell Voigt Zener	Elastography	Klatt <i>et al.</i> [37]
Bulk Muscle	Animal	$E: 25 - 49\text{ kPa}$, $\eta: 3.3 - 15\text{ Pa}\cdot\text{s}$	Voigt	Elastography	Catheline <i>et al.</i> [43]
Finger tissue/skin	Human	Tissue: $E=3.4\text{kPa}$, $\eta=1 - 100\text{ kPa}\cdot\text{s}$ Skin: $E=136\text{ kPa}$, $\eta=1 - 100\text{ kPa}\cdot\text{s}$	Voigt	Indentation	Wang <i>et al.</i> [39]
Silicone	-	$E=1.2\text{ MPa}$, $\eta=3.3 - 24\text{ kPa}\cdot\text{s}$	Voigt	pressure	Alustruey <i>et al.</i> [38]

Table 2.2: A selected summary of values of the viscoelastic parameters (E : Modulus of elasticity, and η : Viscous-coefficient) of various materials with the method of testing or application and model used for representation

2.2.3 Microbial gels and vaginal tissue properties

In his study, Karri modelled the tissue as a linear and non-linear elastic material to investigate the relative effects of the vaginal tissue elasticity and gravity of on the flow of different gels [19]. This kind of fluid-structure interaction modelling approach, known as “elastohydrodynamic lubrication over soft substrates” was first employed in a vaginal drug delivery system by Szeri *et al.* [15]. In their study, Szeri *et al.* investigated the combined effects of body forces acting on the fluid due to gravity and the transverse squeezing forces exerted by the vaginal walls [15]. The main differences between the two studies were the constitutive models chosen for the non-Newtonian fluid, the parameter sets studied, and the numerical methods employed to solve the governing equations. However, both studies considered a wide range of values for the modulus of elasticity (1 – 100 kPa). This range was based on the elastic modulus determined for human soft tissue in general [15, 44]. The literature review of this document also confirms this range as appropriate (see Table 2.2).

There are several methods and techniques in determining the biomechanical properties of soft tissues (e.g. tensile test, elastography, indentation), but understanding and describing the properties of soft tissue under compressive deformations are more relevant for this study. Effort in determining the properties of vaginal soft tissue *in vivo* with such an approach was recently explored by Egorov *et al.* using a “Vaginal Tactile Imaging” probe to determine the linear elasticity of the vaginal tissue [45]. They presented a new method to measure and quantify the elasticity of the vaginal tissue for normal and prolapsed cases *in vivo* [45]. That study included 31 subjects with normal and with “pelvic organ prolapsed conditions (stage I-III)” [45]. Even though Egorov’s instrument was expected to measure elastic modulus within the range of 2 – 40 kPa, the reported data didn’t span the entire range. It was reported that for normal conditions, the average value for elasticity of the anterior compartment was 7.4 ± 4.3 kPa and for the posterior compartment was 6.2 ± 3.1 kPa. For Stage III prolapse, the average

values were lower 1.8 ± 0.7 kPa for the anterior compartment and 1.8 ± 0.5 kPa for the posterior compartment [45].

Currently, a device intended to measure the biomechanical properties of the vaginal tissue is under development by Mark Pacey (The University of Kansas), a member of Dr. Kieweg's research group. This device is similar to Egorov's instrument in the sense that both instruments apply compressive pressure on the tissue to generate a measurable response. However, the instrument under development is expected to capture and measure both the elasticity and the viscous parameters. Once the development of this novel instrument is completed, we would be able to specify and incorporate the exact biomechanical properties of the vaginal tissue viscoelastic parameters in our flow models, which would help us in further developing the rheological characteristics of our microbicidal gel formulations.

Since we chose to represent the viscoelasticity properties of the vaginal tissue with the Voigt model, which requires distinct parameters (i.e. the modulus of elasticity E and viscous-coefficient η) and due to the lack of value ranges for the elastic and viscous components of the vaginal tissue, it was necessary to estimate parameter ranges based on relevant literature related to biological soft tissues (see section 2.2.2 and summarized data in Table 2.2).

In this study we considered relatively broad ranges for both the modulus of elasticity and the viscous-coefficient. We estimated tissue elasticity between 1 and 50 kPa and this range is within a larger range (1 – 100 kPa for soft tissue) considered by Karri [19] and Szeri *et al.* [15]. For the tissue viscous component we considered values between 0 and 10 kPa·s, which are well within the wide range of viscous-coefficient values reported in Table 2.2 for soft tissues. Since this study was a first attempt in incorporating the tissue viscous component, we were conservative with the range of the tissue viscous-coefficient η . These parameter values were used to bracket a range of values for the viscoelastic parameters, while waiting the completion of the development of our measuring device and the publication of

more relevant data related to the vaginal tissue biomechanical properties. Besides examining the interaction between the tissue viscoelasticity and the fluid with different rheological properties, the results of this study would serve also as an indication of the significance of the vaginal tissue viscous component and therefore inform our research group about the importance in pursuing the development that would make the instrument able to measure the viscoelastic properties rather than just the elastic properties.

Chapter 3: The effects of the tissue viscoelastic properties on the flow of a microbicidal gel

3.1 Introduction

According to the 2012 United Nations report on AIDS, 34 million people were living with HIV and 1.7 million individuals died with causes linked to AIDS by the end of 2011 [3]. Over the past several years, the number of people acquiring HIV has showed a continuous decline. Even with this steady decline 2.5 million individuals contracted HIV in 2011[3]. Thus, HIV continues to be a global pandemic. Over half of newly infected adults are women [4], and the majority of these women live in the developing world [5]. In fact, about 70% of the infected women live in sub-Saharan Africa [6]. Due to gender inequality, women in many countries are unable to adjudicate the use of condoms [7]. Unlike condoms, microbicides are self-administered, making microbicides convenient methods of prevention against HIV and other STIs, especially for women who can't control or negotiate the use of condoms. The current absence of an effective HIV vaccine makes the development of effective and safe microbicides essential [4].

Microbicides have become preferred methods in providing women with protection against HIV transmission [5]. However, there isn't a universal microbicide that is approved for general public use. Microbicides are expected to remain an important mean of protection against HIV, even after the discovery of an effective HIV vaccine, as they perform complementary roles to combat HIV on a global platform [8]. Therefore, there is an evident and urgent need in designing and developing microbicides against HIV primarily, and other STIs in general.

Since ancient times, the vagina has been known to be a drug delivery route, and more recently, this route of delivery has been rediscovered for delivery of therapeutic substances [9]. Several recent studies considered various drug release methods using the female genital

tract as the primary route of delivery. The release modes include intravaginal ring [10-12], mucoadhesive polymers [13, 14], and wall-coating microbicides [15-18].

The human female genital tract in its relaxed state is described as a thin-walled, fibromuscular, asymmetric, collapsed tube that can easily be dilated [21, 22]. The shape of the vaginal tube doesn't conform to any known conventional geometric shape, yet the cross section of the vagina has been generally represented as an "H" shape [21]. In terms of size, the length of the human vagina can range between 7-10 cm with a wall thickness between 0.5 – 2.0 cm [15, 22]. One of the main determinants of tissue thickness is age. After menopause, women undergo a reduction in estrogen levels causing the volume of cytoplasm to decrease and the epithelium to become atrophic making the tissue thinner. However, currently there are no data that quantitatively compare the thickness in women pre and post menopause [46].

The human vaginal tissue is comprised of four major layers: (i) the vaginal mucosa, a region of stratified epithelial tissue; (ii) the vaginal submucosa, a vascularised connective tissue region; (iii) the muscularis layer, a region comprised of smooth muscle; and (iv) the adventitia, which consists of loose connective tissue [23]. The composition and the geometry of the female genital tract are factors that strongly affect the biomechanical properties of the vaginal tissue [24].

Coating vaginal or rectal epithelium using microbicides is a promising preventive procedure against HIV and other sexually transmitted infections (STIs). A microbicide gel is deployed as a delivery vehicle of anti-HIV and other anti-STI agents and it is also used to act as a barrier between the pathogens and the biological tissue. The efficacy of a microbicide gel depends on the extent of the spreading, the amount of the epithelial surfaces coated, and the retention on the vaginal surfaces [47].

The ultimate goal of our research group is to develop reliable and effective microbicide gel formulations as drug delivery vehicles. In order to achieve this goal, it is of

great importance to identify and investigate critical factors that would affect the spreading of a gel. It is expected that the flow of a gel in the vaginal tract would be influenced by mechanical properties of the vaginal tissue, the geometry of the vaginal canal, and the surface properties of the vaginal epithelium.

Microbicidal gels possess shear-thinning rheological properties. The shear-thinning behaviour of a gel can be described using models such as the power-law and the Ellis constitutive equations. To study the flow of microbicidal gels, mathematical and experimental models have been used. Kieweg *et al.* developed an *in vitro* experimental model to examine the impact of the gravity and the surface type on the flow of different gel formulations [47]. They determined that the gel's rheological properties and the surface wettability have a substantial influence on the distribution of different gels [47]. Hu and Kieweg introduced a 2D numerical model of a gravity-driven free surface flow that incorporated surface tension with the power-law model as the non-Newtonian fluid [48]. They found that the surface tension influenced the speed of the flow of the gel compared to the flow without surface tension [48]. They also observed the appearance of a capillary ridge, which is due to the surface tension and associated with fingering instabilities [48]. Fingering instabilities are expected to alter the spreading of a microbicidal gel and therefore affect the degree of protection of the epithelium [48].

Kheifets and Kieweg expanded the 2D model by Hu [48] to a 3D flow model to account for the lateral spreading [49]. They determined that the 2D model (axial spreading only) greatly overestimates the flow extent compared to the experimental results, whereas the 3D model results were reasonably close to the experimental results. Additionally, the gel shear-thinning index and consistency have an impact on the spreading extent of the gel.

Kieweg and Katz introduced a numerical model, as well as an experimental model, to investigate the flow of vaginal microbicides under the influence of squeezing forces applied

by rigid plates [26]. Using the power-law and Hershel-Bulkley constitutive models for non-Newtonian fluids, they determined that the squeezing forces and the fluid's properties have an important impact on the flow of vaginal microbicides [26].

Recent studies investigated the flow of microbicidal gels under the influence of gravity and squeezing effects due to the elasticity of the vaginal walls [15, 19]. Szeri *et al.* [15] and Karri [19] both examined the impact of combined effects of gravity and squeezing forces and found that larger squeezing forces due to high tissue elasticity leads to more gel spreading. The spreading extent depends on the rheological properties of the fluid and the application time [15, 19].

The vaginal tissue, like many other human soft tissues, is anticipated to exhibit viscoelastic characteristics [20]. Thus, it is important to investigate the potential effects of the viscoelastic properties of the tissue, rather than only its elasticity, on the spreading of a microbicidal gel. This study is a first attempt at incorporating the viscoelastic characteristics of the vaginal tissue in a microbicidal gel delivery system.

It is well known that most biological tissues exhibit viscoelastic characteristics. These characteristics are generally non-linear, anisotropic, and time-dependent [28]. There are numerous studies and investigations that describe the biomechanical properties of soft tissues in general, but only a few studies focus on characterizing the viscoelasticity of the human vaginal tissue. Research in the field of vaginal biomechanics remains limited [11].

Many biological tissues are better represented with complex non-linear mechanical models or with strain-energy function based models, because they describe and capture the viscoelastic characteristics of these tissues more accurately. Nonetheless, simple mechanical models, such as Voigt, Kelvin, and Zener models are widely used to study and investigate soft tissue viscoelastic response under specific loading conditions and over certain parameter ranges (e.g. [25, 31-35]).

Published data for biological soft tissue vary with the different methods and approaches used for characterization [30]. Due to the limited data related to the biomechanics of the human vaginal tissue, we considered studies that focused on the viscoelasticity of soft tissue in general, including animal tissue. We also considered studies and data for tissue-mimicking materials.

The aim of this study is to incorporate the viscoelastic characteristics of the vaginal tissue and investigate the impact of these properties on the flow of microbicidal gels compared to the impact of tissue elasticity only. A better understanding of the interaction between the tissue mechanical properties and the fluid rheological properties is gained by expanding the research of microbicidal gel flow under the combined influence of gravitational and squeezing forces.

3.2 Methods

3.2.1 Problem formulation

In this section we derive a partial differential equation that describes the shape of a spreading finite-volume bolus of fluid placed between two viscoelastic boundaries. The nonlinear PDE (governing equation) describes the evolution of the fluid-solid interface as a function of time and space $h(x, t)$. Figure 1 shows the schematic of the initial and boundary conditions of the 2D model, where the fluid is spreading due to gravity and squeezing forces from the viscoelastic tissue.

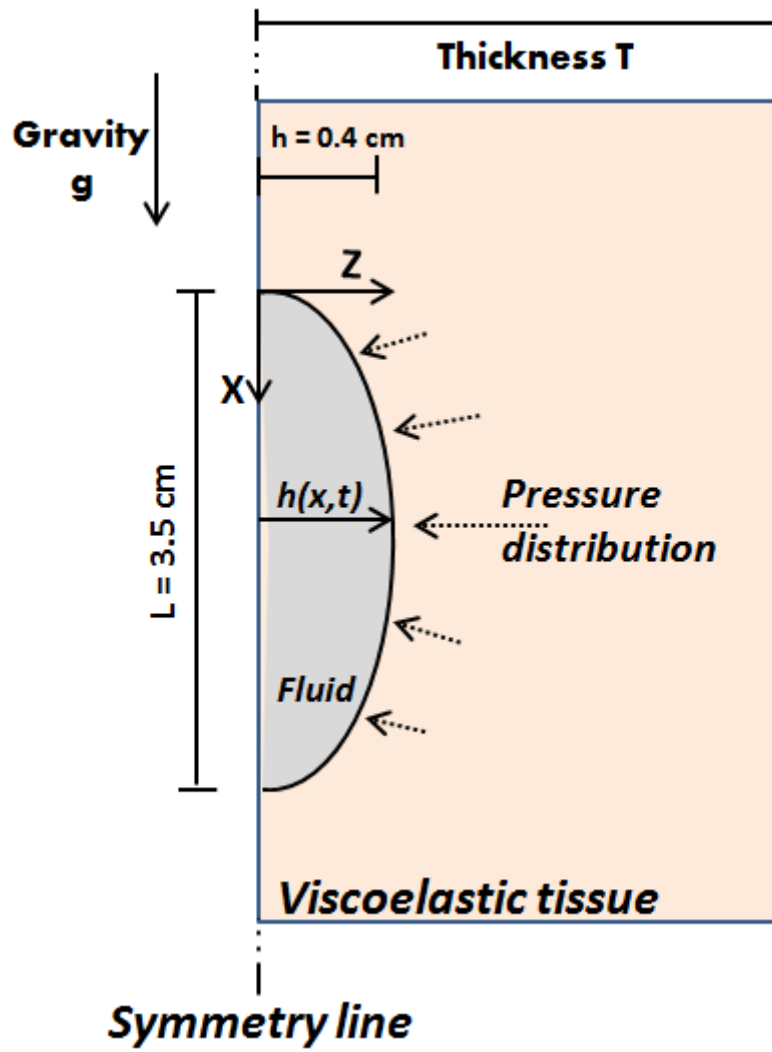


Figure 3.1: Initial geometry of the bolus and tissue. The bolus is symmetrical about the vertical line at all times. The pressure from the boundary and gravity are the driving forces of the flow.

To derive the evolution equation (i.e. governing equation), we first start with the conservation of linear momentum (Equation (3.1)), where \mathbf{u} is the velocity vector, \mathbf{g} is the gravitational acceleration, p is the pressure, $\boldsymbol{\tau}$ is the shear stress tensor, and ρ is the fluid's density.

$$\frac{d\mathbf{u}}{dt} + (\mathbf{u} \cdot \nabla)\mathbf{u} = -\frac{1}{\rho}\nabla \cdot \mathbf{p} + \frac{\nabla \cdot \boldsymbol{\tau}}{\rho} + \mathbf{g} \quad (3.1)$$

Using the thin-film lubrication approximation [50], the momentum equation (Equation (3.1)) is simplified for the 2D flow and written as the following governing equations:

$$x\text{-Direction: } 0 = -\frac{\partial p}{\partial x} + \frac{\partial \tau_{zx}}{\partial z} + \rho g_x \quad (3.2)$$

$$z\text{-Direction: } 0 = -\frac{\partial p}{\partial z} \quad (3.3)$$

Equations (3.2) and (3.3) represent the components of the momentum in the x and z directions.

The bolus is assumed to be symmetrical along its vertical axis at all times and that there is no mass transfer across the symmetry line during the flow (Figure 3.1). Integrating the x -momentum (Equation (3.2)) with respect to z and using the symmetry boundary condition $\tau_{zx}|_{(z=0)} = 0$ yields:

$$\tau_{zx} = \left(\frac{\partial p}{\partial x} - \rho g_x \right) z \quad (3.4)$$

The pressure p exerted on the fluid in this configuration (Figure 3.1) is the normal stress applied by the soft tissue due to the deformation caused by the bolus. Figure 3.2 shows the schematic of the Voigt model. The Voigt model was utilized to represent the response of the tissue viscoelastic properties. The constitutive equation of the Voigt model allowed us to write the stress-strain relationship as a pressure term in the governing equation and therefore incorporate the viscoelastic parameters (i.e. the tissue modulus of elasticity E and viscous-coefficient η).

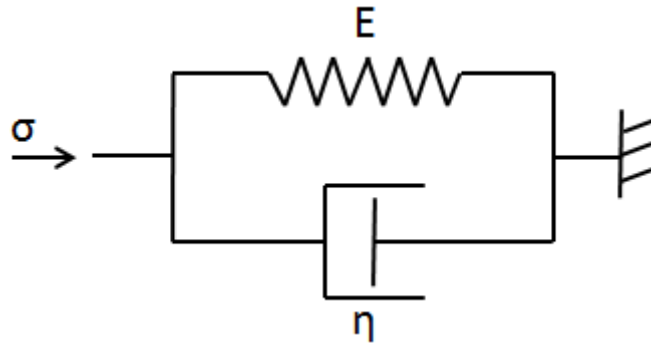


Figure 3.2: The Voigt model for viscoelastic materials

With the Voigt model, the stress-strain relationship is given by:

$$\sigma = E \varepsilon + \eta \dot{\varepsilon}(t) \quad (3.6)$$

where, E is the tissue elastic modulus, and η is the tissue viscous component. We define the strain $= \frac{h(x,t)}{T}$, where $h(x,t)$ is the fluid height and T is the initial thickness of the tissue and write the pressure term as:

$$p = \frac{Eh}{T} + \frac{\eta}{T} \frac{\partial h}{\partial t} \quad \text{at } z = h(x,t) \quad (3.7)$$

For 1D spreading, the power-law constitutive equation (Equation (3.8)) relates the shear τ_{zx} to the axial velocity u , where m and n are the fluid's consistency and shear-thinning index, respectively [48].

$$\tau_{zx} = m \frac{\partial u}{\partial z} \left| \frac{\partial u}{\partial z} \right|^{n-1} \quad (3.8)$$

Substituting Equations (3.7) and (3.8) into Equation (3.4), integrating the latter with respect to z , and using the no-slip boundary condition $u|_{(z=h)} = 0$ yields an expression for flow velocity:

$$u(x, z, t) = \frac{1}{\left(1 + \frac{1}{n}\right)m} \left(\frac{E}{T} \frac{\partial h}{\partial x} + \frac{\eta}{T} \frac{\partial^2 h}{\partial x \partial t} - \rho g_x \right) \left| \frac{1}{m} \left(\frac{E}{T} \frac{\partial h}{\partial x} + \frac{\eta}{T} \frac{\partial^2 h}{\partial x \partial t} - \rho g_x \right) \right|^{\frac{1}{n}-1} \left(|z|^{1+\frac{1}{n}} - |h|^{1+\frac{1}{n}} \right) \quad (3.9)$$

We use the velocity expression to determine the flow rate per unit width (flux), which is defined as:

$$q(x, t) = \int_0^{h(x,t)} u(x, z, t) dz \quad (3.10)$$

The resulting expression for the flux is:

$$q(x, t) = \frac{-n}{m^{1/n}(2n+1)} \left(\left(\frac{E}{T} \frac{\partial h}{\partial x} + \frac{\eta}{T} \frac{\partial^2 h}{\partial x \partial t} - \rho g_x \right) \left| \frac{E}{T} \frac{\partial h}{\partial x} + \frac{\eta}{T} \frac{\partial^2 h}{\partial x \partial t} - \rho g_x \right|^{\frac{1}{n}-1} h^{2+\frac{1}{n}} \right) \quad (3.11)$$

The evolution equation is obtained by inserting the flux expression into the conservation of mass equation (Equation (3.12)).

$$\frac{\partial h(x, t)}{\partial t} + \frac{\partial q(x, t)}{\partial x} = 0 \quad (3.12)$$

We note that by setting the boundary viscous component $\eta = 0$ we obtain the governing equation of the flow between pure elastic boundaries. We write the evolution equation in a non-dimensional form using the following dimensionless scaling ratios: $\bar{h} = h/H$, $\bar{x} = x/H$, $\bar{t} = t \left(\frac{EH}{Tm} \right)^{\frac{1}{n}}$, where H is the initial maximum of the gel bolus. The resulting non-dimensional evolution equation is given by:

$$\frac{\partial \bar{h}(x, t)}{\partial \bar{t}} - \frac{n}{(2n+1)} \frac{\partial}{\partial \bar{x}} \left[\left(\frac{\partial \bar{h}}{\partial \bar{x}} + Z \frac{\partial^2 \bar{h}}{\partial \bar{x} \partial \bar{t}} - W \right) \left| \frac{\partial \bar{h}}{\partial \bar{x}} + Z \frac{\partial^2 \bar{h}}{\partial \bar{x} \partial \bar{t}} - W \right|^{\frac{1}{n}-1} \bar{h}^{2+\frac{1}{n}} \right] = 0 \quad (3.13)$$

where $Z = \frac{\eta}{E} \left(\frac{EH}{Tm} \right)^{\frac{1}{n}}$, $W = \frac{T\rho g x}{E}$ are non-dimensional variables.

3.2.2 Numerical method and model validation

The governing equation is a nonlinear PDE (Equation 3.12) was solved numerically. The governing equation was discretized in time using the θ -method (Equation (3.14)).

$$\frac{h_i^{p+1} - h_i^p}{\Delta t} + \theta f_i^{p+1} + (1 - \theta) f_i^p = 0 \quad (3.14)$$

Where $0 \leq \theta \leq 1$, the indices p and $p+1$ refer to the current time and next time respectively, and Δt is the time step size [51]. With $\theta = 1$ the method yields the implicit backward Euler scheme, which has a first order accuracy. The central finite difference scheme was employed for space discretization. The central finite difference method provides a second order accuracy. The evolution equation (Equation(11)) discretized around the spatial i^{th} node is given by:

$$\frac{h_i^{p+1} - h_i^p}{\Delta t} + \frac{q_{i+\frac{1}{2}}^{p+1} - q_{i-\frac{1}{2}}^{p+1}}{\Delta x} = 0 \quad (3.14)$$

The resulting nonlinear algebraic equations were solved using Newton's method. Newton's method was set to converge after a maximum of 10 iterations. A maximum error of 10^{-13} was set as the convergence criteria with an error tolerance of 10^{-8} . If the error tolerance

was larger than 10^{-8} , an adaptive time stepping method was applied to reduce the time step size Δt (initially set to 10^{-3} sec) by a factor of 0.8 (20% reduction). The numerical approach was implemented using a C-code.

In order to save computational time, we exploited the symmetry in the computational domain (Figure 3.1). The computational flow domain was chosen to be 20 cm long. The simulations were run for a total of 100 seconds as long as the spreading length didn't exceed 15 cm, which was chosen to be the spreading length limit since the length of the human vagina is in the range of 7-10 cm [22]. Even though the real application time is expected to be longer than the total simulation time of 100 seconds, the simulation time was long enough to provide insights on the flow behaviour of the fluid. Additionally, longer simulation times would have extended the overall computational time of the simulations substantially.

We performed a mesh convergence study by refining the computational spatial mesh until the change in the numerical results was less than 1%. Additionally, we monitored the area of the bolus over the computational time to ensure conservation of mass.

3.2.3 Parametric study method

In order to evaluate the impact of different parameters of the mathematical model on the flow behaviour, a series of coupling parametric studies were conducted. The parametric studies investigated the impact of the tissue's viscoelastic parameters on the spreading of the fluid with different rheological properties. The parametric studies were performed to evaluate the extent of influence of the tissue viscous component η relative to the tissue elasticity on the flow behaviour of the fluid with different properties (i.e. shear-thinning index n , and fluid's consistency m). In this study, the coupling parametric studies are based on varying two parameters for a given set of values of the other two parameters. For instance, in a set of simulation cases we varied the tissue elastic and viscous components for a fixed set of the

fluid shear-thinning index and consistency. There were a total of three series of coupling parametric studies with the following sets of parameters as the variable parameters:

- 1) η and E
- 2) η and m
- 3) η and n

For the dimensional analysis, four parameters were considered for the parametric studies (n , m , E , and η), while the other parameters listed in Table 3.1 were kept constant. The fluid density ρ was set to be 1 g/cm³ since this value is commonly used for the density of a microbicidal gel [18, 19]. The tissue thickness was set to be 1.5 cm, which is within the range of the vaginal wall thickness [22].

Constant Parameter	Value
Acceleration, g	980 cm/s ²
Tissue Thickness, T	1.5 cm
Inclination angle, α	$\pi/2$
Fluid density	1 g/cm ³

Table 3.1: The constant parameters of the numerical model

We considered relatively large ranges for the vaginal tissue viscoelastic properties. Due to the lack of data for the biomechanical properties of the vaginal tissue, we considered data determined for other soft tissues. For the tissue elasticity E , we chose values between $E = 1$ and 50 kPa, and for the viscous-coefficient, we chose values between $\eta = 0$ and 10 kPa·s. These values were based on relevant data found in literature, which included studies involving human as well as animal tissues in addition to soft tissue mimicking materials [30, 33, 35-39, 43, 52]. For the gel rheological properties, the consistency ranged from $m = 100$ to 600 Psⁿ⁻¹ and the shear-thinning index ranged from $n = 0.5$ to 1.0, which are typical for microbicidal gels [26, 48].

For the non-dimensional analysis of the dimensionless model, the parameters n , W , and Z were determined to be the model's variables. The dimensionless parameters Z and W varied from 4 to 3.5×10^5 and 0.00294 to 0.147, respectively. These ranges were determined based on the values of dimensional parameters: n , m , E , η . The non-dimensional analysis was an approach to study the interactions between the dimensionless parameters $W = \frac{T\rho g_x}{E}$ and $Z = \frac{\eta}{E} \left(\frac{EH}{Tm} \right)^{\frac{1}{n}}$ with respect to the dimensionless spreading length. A total of 386 simulations were run to carry out the dimensional parametric studies and the non-dimensional analysis.

3.3 Results and discussion

The parametric studies explored the relative influence of the tissue elastic E and the tissue viscous-coefficient η on the flow of the fluid. The studies also examined the degree of influence of the viscous-coefficient η on the flow of the fluids with different rheological properties (i.e. shear-thinning index n and consistency m). The results of this study are presented mainly in the dimensional form because in a non-dimensional analysis any dimensionless group that includes the parameter m (units: $P \cdot s^{n-1}$) has to include the parameter n (no units). Additionally, from a development stand point the dimensional results of parametric studies are more relevant for the design and optimization of the gel rheological properties [49].

3.3.1 The impact of elastic and viscoelastic boundary

The first step in investigating the impact of the viscoelastic characteristic of the tissue on the flow behaviour of the fluid was to compare the spreading profiles with viscoelastic boundaries to the profiles generated with elastic boundaries. The comparison between the squeezing effects of the viscoelastic and the elastic boundaries on the flow assessed the impact and the importance of the tissue viscous-coefficient η on the flow behaviour of a microbicidal gel.

To illustrate the effect of the tissue viscous component η on the flow of the gel-bolus, an example of the flow profiles of the bolus that best show the difference between the viscoelastic model and the elastic model ($\eta = 0 \text{ kPa}\cdot\text{s}$) of the tissue are presented in Figure 2. The profiles presented in Figure 3.3 left (elastic) and right (viscoelastic) show the evolution profiles of the bolus over time starting from the initial time $t = 0$ seconds at intervals of 10 seconds to $t = 50$ seconds and then at $t = 100$ seconds.

Previously, Karri [19] found in his study, in which he considered the flow between pure elastic boundaries, that in some cases the direction of the flow was entirely downward and in other cases the flow occurred in both directions downward as well as upward. He determined that the direction of the flow is directly related to the relative effects of the tissue elasticity and the gravitational force. He observed that with relatively low tissue elasticity, the effect of gravity dominated the flow hence the downward spreading. With high tissue elasticity, the squeezing effect dominated the flow thus the spreading in the downward as well as in the upward directions [19]. Similar trends were observed in this study and thus not described in detail further.

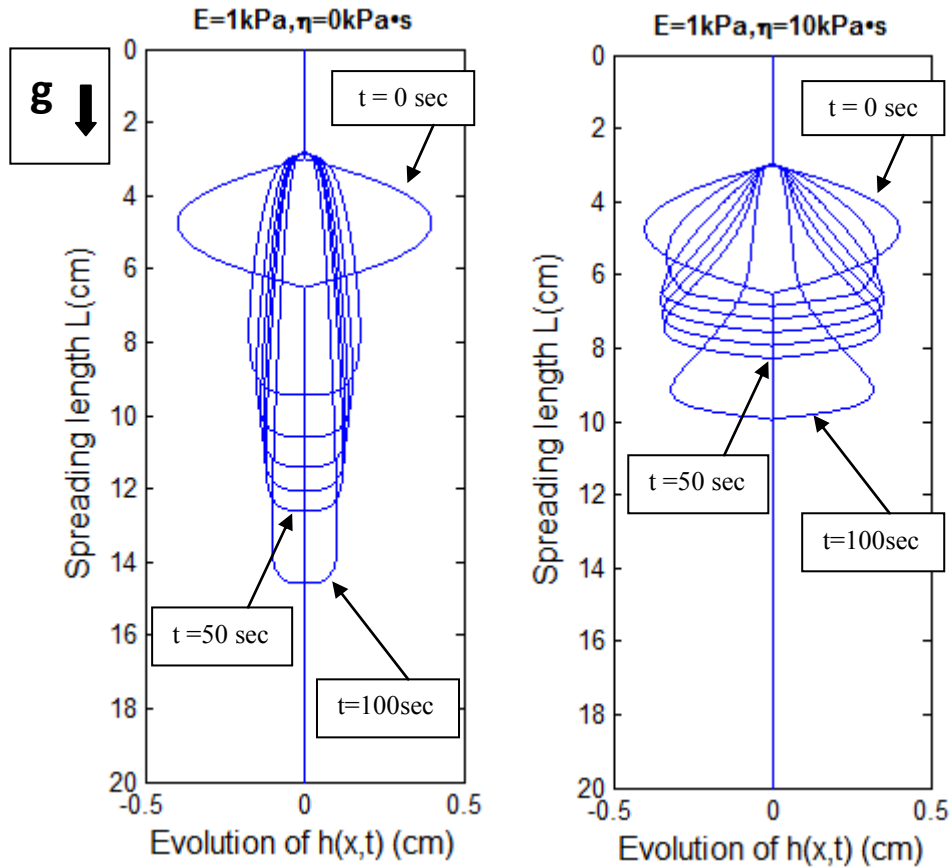


Figure 3.3: Example of flow profiles of a power-law fluid ($n = 0.6$, $m = 100 \text{ P}\cdot\text{s}^{-n-1}$) with two different sets of tissue elastic E and viscous η components illustrating the difference in the impact of the elastic model and the viscoelastic model of the tissue.

It is apparent from the spreading profiles (Figure 3.3) that the viscous-coefficient η has an impact on the flow patterns of the fluid. Figure 3.4 shows the amount of change in the spreading length L_{max} , which represents the length of the bolus after 100 seconds for various magnitudes of the tissue elastic (E) and viscous (η) components. Similar trend was observed for with various sets of fluid consistency and shear-thinning index values. The change in the spreading length was more pronounced for lower tissue elasticity. Thus the impact of the tissue viscous-coefficient η is more important at low tissue elasticities.

The impact of the tissue viscous-coefficient η diminished with larger tissue elasticity regardless of the magnitude of the viscous-coefficient or of the fluid's rheological properties (Figure 3.4). At high tissue elasticity the impact of the tissue viscous-coefficient is negligible.

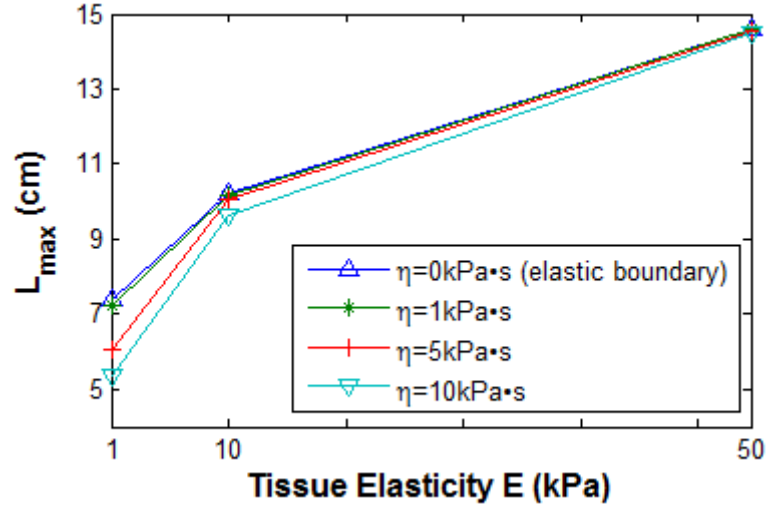


Figure 3.4: Example of change in the spreading length of a power law fluid ($n = 0.6$, $m = 300 \text{ P}\cdot\text{s}^{n-1}$) with various values of tissue elasticity E and viscous-coefficient η .

The difference between the viscoelastic model and the elastic model was primarily related to the relative difference between the magnitudes of the tissue elasticity and viscous-coefficient. In order to quantify the difference in impact on the flow between the viscoelastic model and the elastic model, the percentage change in the maximum spreading length (% change in L_{max}) was determined for all parameter sets. The % change in L_{max} was defined as:

$$\% \text{ change in } L_{max} = \frac{L_{max,viscoelastic} - L_{max,elastic}}{L_{max,elastic}} \times 100 \quad (3.41)$$

where $L_{max,viscoelastic}$ and $L_{max,elastic}$ are the maximum lengths with the viscoelastic model and the corresponding elastic model, respectively. The % change in L_{max} compared the viscoelastic boundary with the larger η value ($\eta = 10 \text{ kPa}\cdot\text{s}$) for different magnitudes of elasticity E and the corresponding elastic cases ($\eta = 0 \text{ kPa}\cdot\text{s}$). Table 3.2 shows the largest and the smallest percentage change in the maximum spreading lengths of the fluid.

tissue parameters ($E \text{ (kPa)}, \eta \text{ (kPa}\cdot\text{s)}$)	% change in L_{max}	
	Relative to the corresponding elastic case ($\eta = 0 \text{ P}\cdot\text{s}^{n-1}$)	
	Min. change	Max. change
(1, 10)	-18.53	-46.78
(10, 10)	-3.04	-8.75

(50, 10)	-0.75	-1.15
----------	-------	-------

Table 3.2: Maximum percentage change in the maximum length L_{max} with tissue viscous-coefficient $\eta = 10 \text{ P}\cdot\text{s}^{n-1}$ for different tissue elasticity E and all combinations of fluid's shear-thinning index n and consistency m .

The largest minimum change of -18.53% was determined with shear-thinning $n = 0.6$ and consistency $m = 600 \text{ P}\cdot\text{s}^{n-1}$, whereas the largest maximum change of -46.78% was determined with shear-thinning index $n = 1$ and consistency $m = 100 \text{ P}\cdot\text{s}^{n-1}$.

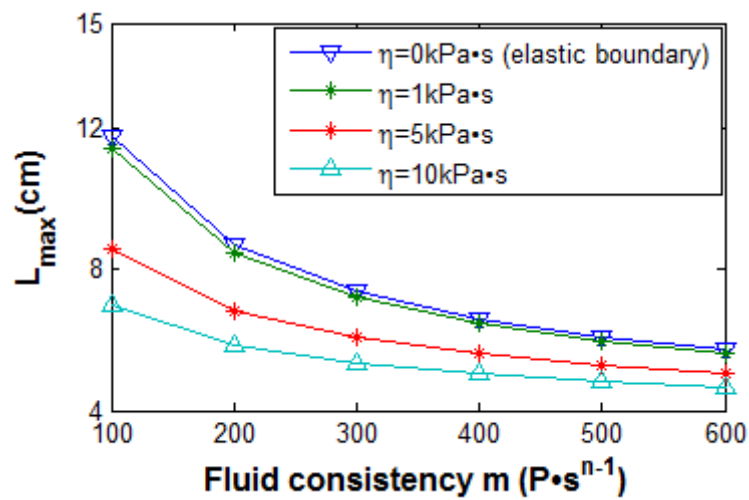
The change in the bolus spreading extent with increasing viscous-coefficient η was associated with a corresponding change in the bolus height (i.e. bolus thickness). This can clearly be seen in figure 3.1. The change in bolus height was especially pronounced in the cases of low elasticity and high or relatively high viscous-coefficient. Larger viscous-coefficient signifies larger deformation potential of the tissue, thus higher dissipation of the energy generated by the straining of the tissue, hence the extra deformation of the viscoelastic boundary (Figure 3.1). The change in height occurred primarily at the downstream portion of the bolus. Similar trends were observed with various combinations of fluid consistency and shear-thinning index values.

3.3.2 The influence of the tissue viscous-coefficient η on the flow of the fluid with varying rheological properties

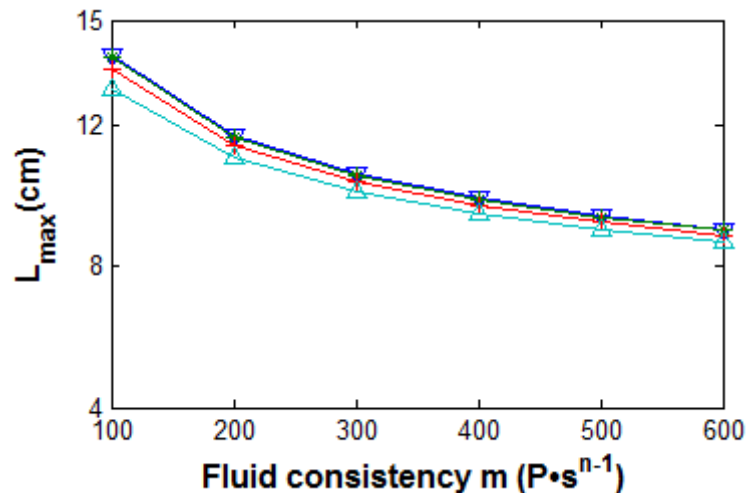
In this section, major results regarding the influence of the tissue viscous-coefficient η on the flow of the gel with different rheological properties (i.e. consistency m , and shear-thinning index n) are presented. Previously Karri [19] found that the spreading of the bolus between pure elastic boundaries increased with decreasing fluid consistency and increasing shear-thinning index [19].

A. Impact of tissue viscous-coefficient η on the spreading of fluids with different consistency m

Figure 3.5 shows that for a fluid with lower consistency, the tissue viscous component has more impact on the bolus spreading extent. This influence on the spreading length was more pronounced at low tissue elasticity. Similar patterns were observed with other parameter sets. The difference between the elastic and the viscoelastic boundaries was more pronounced for lower elasticity and higher viscous-coefficient and at low fluid consistency.



(a) $n = 0.6, E = 1 \text{ kPa}$



(b) $n = 0.8, E = 10 \text{ kPa}$

Figure 3.5: (a) – (b) The change in the maximum spreading length L_{max} of the bolus for various values of consistency m , tissue viscous-coefficient η and with different combinations of tissue elasticity E and fluid's shear-thinning index n .

As shown in Figure 3.3 the decrease in the spreading was accompanied by an increase in the bolus height. The change in the height was due to the viscous effect of the tissue, causing the tissue to deform and have the tendency to retain the bolus. Figure 3.6 shows the change in the maximum height h_{max} (height after 100 seconds) with increasing m values for different sets of shear-thinning index and tissue viscoelastic parameters. Initially, the maximum bolus height was set to 0.4 cm.

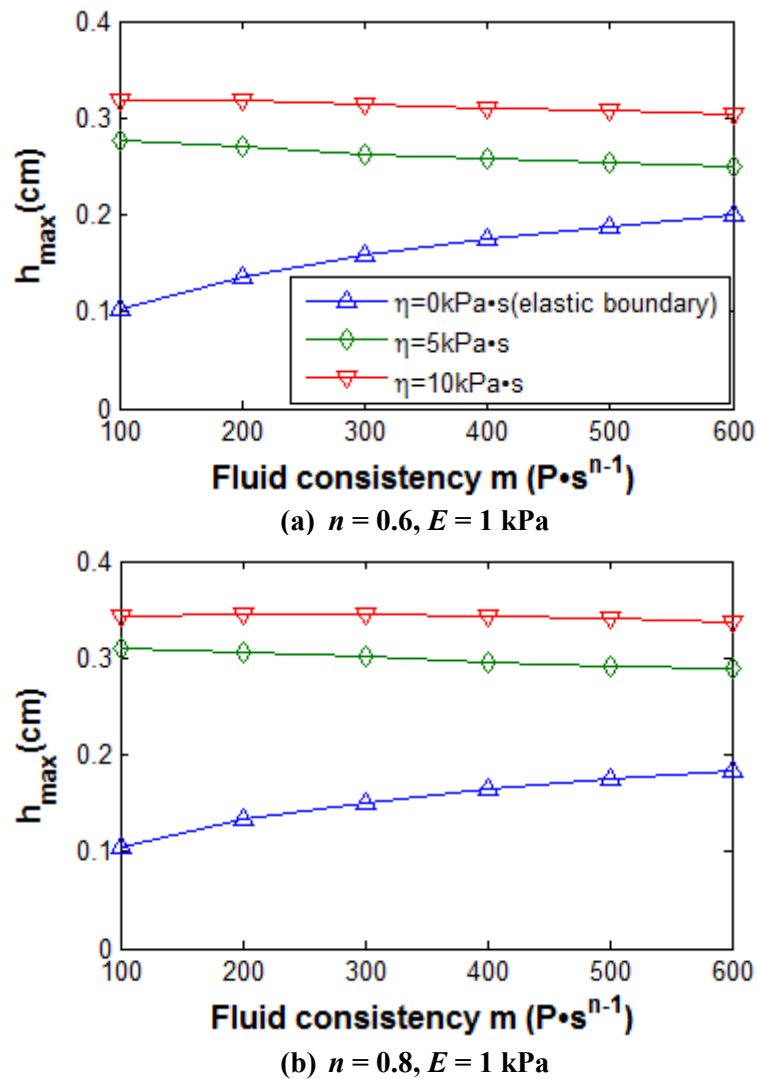


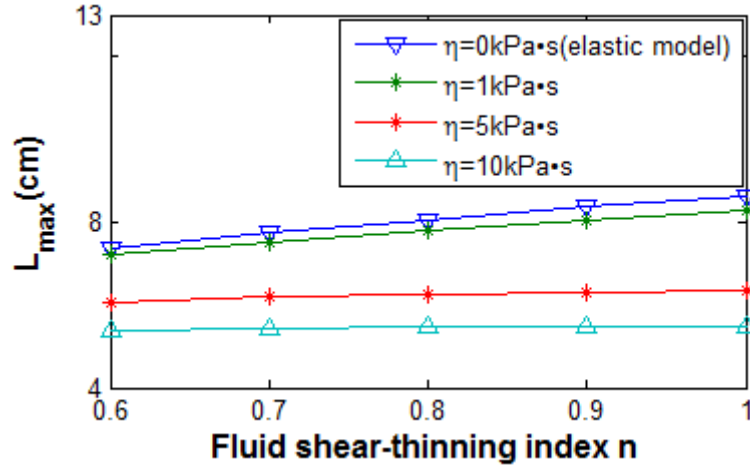
Figure 3.6: (a) – (b) the change in the maximum bolus height h_{max} as a function of the consistency m for different shear-thinning indices and tissue properties (viscous-coefficient η and elasticity E).

Larger η has more impact on the bolus height h_{max} for any fluid consistency m , whereas in the case of $\eta = 0 \text{ P}\cdot\text{s}^{n-1}$ (elastic tissue) the fluid's consistency m has more impact on the bolus height.

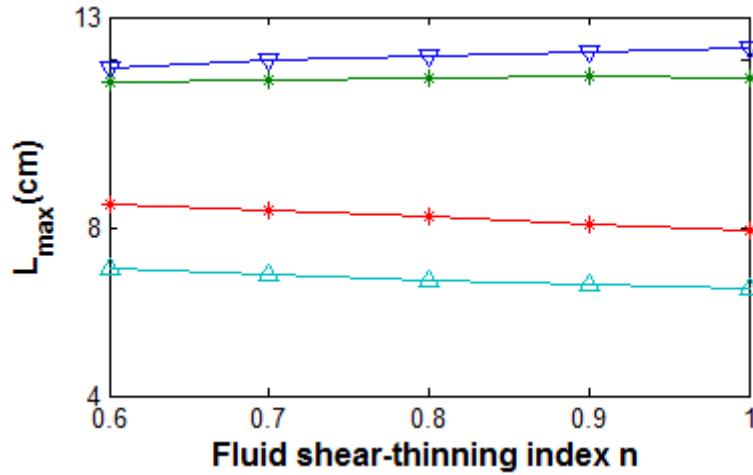
In Figure 3.6, we first note the increasing trend in the maximum height of the bolus with the pure elastic boundary ($\eta = 0 \text{ P}\cdot\text{s}^{n-1}$) as the consistency increased. Figure 3.6 also shows the considerable increase in the maximum height with the viscoelastic boundary compared to the elastic boundary. Unlike the change in the maximum length of the bolus, the maximum height for the viscoelastic tissue did not vary much with different fluid consistency values. The relatively small change in the bolus maximum height suggests that the deformation of the tissue (when represented as viscoelastic) is not greatly affected by the fluid consistency. The bolus has a constant volume and as it flows down, it deforms the tissue by the relatively the same extent.

B. Impact of η on the spreading of fluid with varying shear-thinning index n

In addition to the fluid's consistency m , the shear-thinning index n is the second parameter that describes the rheology of a power-law fluid. In this section, the main results of the impact of the tissue viscous component on the flow of the fluid with different shear-thinning indices are presented and discussed. Figure 3.7 shows an example of the change in the maximum length with increasing shear-thinning index n for different sets of the tissue viscous-coefficient and fluid consistency. For most fluid consistencies and tissue properties the fluid spread more with increasing shear-thinning index. However, the instances where the fluid consistency was low ($m = 100 \text{ P}\cdot\text{s}^{n-1}$) and the tissue viscous-coefficient was relatively large ($\eta = 5$ and $10 \text{ kPa}\cdot\text{s}$), a new trend was observed, namely the spreading length decreased as the shear-thinning index increased (Figure 3.7 (b)). The tissue viscous-coefficient η has a larger impact on the spreading length at larger values of shear-thinning index n . Figure 3.7 illustrates the trends observed for the cases with tissue elasticity $E = 1 \text{ kPa}$. Similar patterns were observed for other cases with different parameter sets.



(a) $m = 300 \text{ P}\cdot\text{s}^{n-1}$, $E = 1 \text{ kPa}$



(b) $m = 100 \text{ P}\cdot\text{s}^{n-1}$, $E = 1 \text{ kPa}$

Figure 3.7: (a) – (b) The change in the maximum spreading length L_{max} of the bolus with various fluid shear-thinning index n , tissue viscous-coefficient η for different combinations of tissue elasticity E and fluid consistency m .

The influence of the tissue viscous-coefficient η was more noticeable as n increased and the low fluid consistency $m = 100 \text{ P}\cdot\text{s}^{n-1}$

To examine the impact on n further, we calculated the spreading rate of the bolus (i.e. the spreading length over time) the low viscous-coefficient values 0 and 1 kPa·s, showed how the spreading rates changed during the flow for the different shear-thinning indices. At early times, the spreading was occurring faster with lower shear-thinning indices, but towards the end of the simulation time, this trend changed and the spreading was faster for larger shear-

thinning indices. This explains the increase in the maximum length with increasing shear-thinning n as shown in Figure 6 (a) for the elastic case ($\eta = 0$ kPa·s) and for the viscoelastic case with $\eta = 1$ kPa·s. For the other cases with higher viscous-coefficient ($\eta = 5$ and 10 kPa·s), we observed a decrease in the spreading lengths and this trend was due to the unchanged spreading rates of the fluid, where the fluid with lower shear-thinning index was spreading faster during the entire simulation time.

The change in the spreading rates due to low fluid consistency and different tissue viscous-coefficient is particularly important considering the dilution factor after the application of the gel. Once the gel is applied to the vaginal canal, it is expected to be mixed with vaginal fluids causing a change in the gel's rheological properties. Changes to the rheological properties would have a direct impact on the spreading behaviour of the gel and therefore on the coating of the targeted surfaces.

As indicated in the section A, the maximum bolus height (i.e. bolus thickness) increased with decreasing bolus length and the change in the maximum height was more pronounced and limited to the cases where parameter η was the larger than the parameter E . we observed a considerable increase in the bolus maximum height with viscoelastic boundary compared to elastic boundary. This trend was similar to the trend shown in figure 3.6, hence the results are not shown here for brevity.

3.3.3 Dimensionless analysis

With the evolution equation in the non-dimensional form (Equation (13)), the flow behaviour of the fluid can be studied in terms of the dimensionless variables $Z = \frac{\eta}{E} \left(\frac{EH}{Tm} \right)^{\frac{1}{n}}$, $W = \frac{T\rho g x}{E}$, n and $\bar{t} = t \left(\frac{EH}{Tm} \right)^{1/n}$. Szeri *et al.* were the first to introduce a non-dimensional model of a non-Newtonian fluid between elastic boundaries. In that model, the non-Newtonian fluid was represented with the Carreau-model [15]. The similarity between the

non-dimensional model introduced by Szeri *et al.* and the one presented in this study is that both models contain a form of a dimensionless variable, which is inversely proportional to the elasticity of the boundary (in this study the dimensionless variable is $W = \frac{T\rho g x}{E}$).

By setting our dimensionless parameter $Z = 0$ (i.e. setting the tissue viscous-coefficient $\eta = 0$ kPa·s) this study reduces to an elastic case that is similar to the case presented by Szeri *et al.* [15]. Therefore, we were able to compare the overall trend of the impact of the parameter W on the dimensionless spreading of the fluid at various dimensionless times \bar{t} . It is important however to note that this study and the Szeri *et al.* study differ from each other in the way the non-dimensional parameters were defined, in the range of the parameters considered for the dimensionless variables, in the constitutive models of the non-Newtonian fluid, and in the numerical solution techniques.

Figure 3.8 illustrates the dimensionless spreading length L_{max}/H as a function of the variable W , where L_{max} is the maximum length at the end of the dimensionless computational time \bar{t} and H is the maximum height of the bolus at the initial condition. Figure 3.8 confirms the trend shown in Szeri *et al.* study [15] (Figure 4), in the sense that as the dimensionless parameter W and the flow time were increased the dimensionless spreading increased. The agreement in trend between these trends validates our numerical model. We also note that even though Szeri *et al.* introduced the dimensionless evolution equation with a non-Newtonian fluid, their dimensionless results were shown for a Newtonian case only, which correspond to shear-thinning index $n = 1$. In this study, the results for both a Newtonian and a non-Newtonian case are presented (Figure 3.8 (a) and (b)). Figure 3.8 (a) and (b) show the difference in the spreading extent between a Newtonian and a shear-thinning fluid.

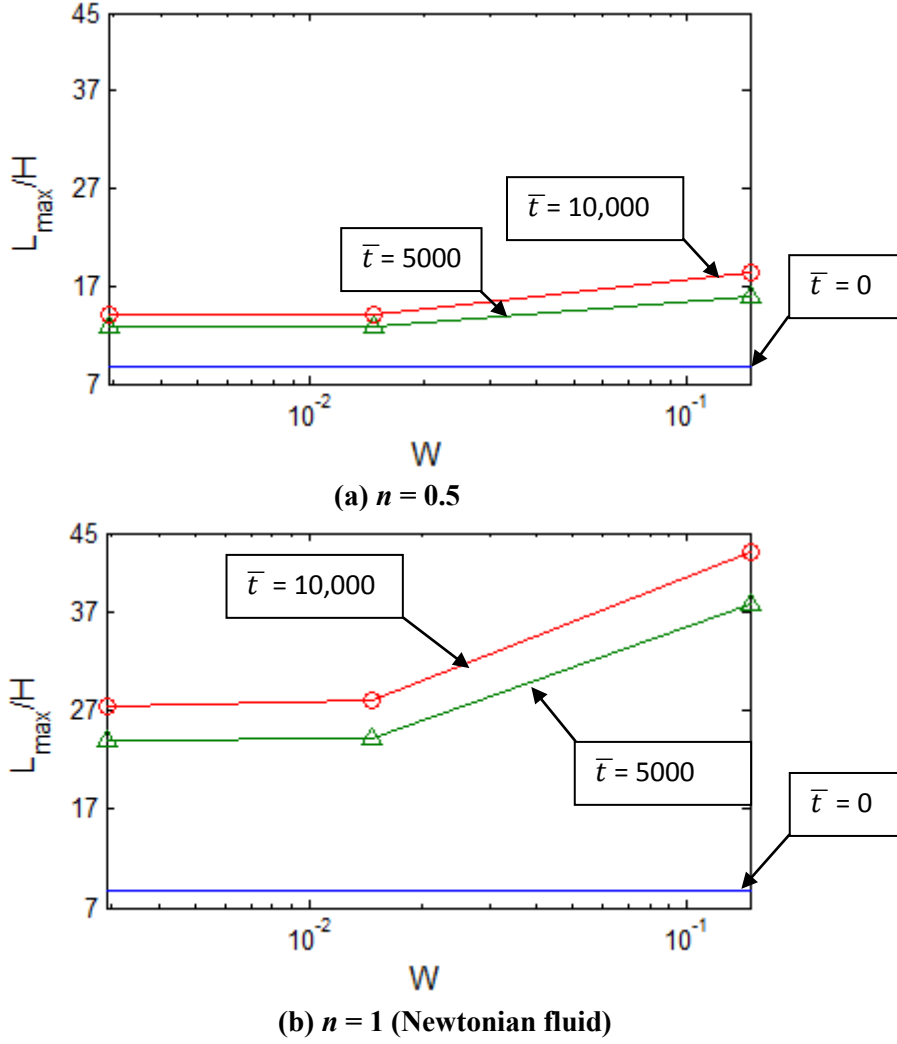


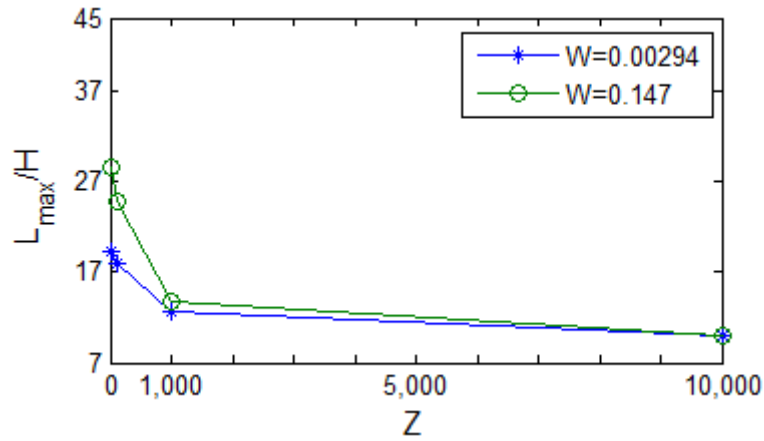
Figure 3.8: (a) - (b) The dimensionless spreading length due to the boundary elasticity only ($Z = 0$) as a function of $W = \frac{T\rho g_x}{E}$ (starting with the lowest value $W = 0.00294$) at different dimensionless time \bar{t} relative to the dimensionless length at the initial condition ($\bar{t} = 0$), for different fluid shear-thinning index n . L_{max} is the maximum dimensional length and H is the bolus initial maximum height.

The dimensionless spreading extent L_{max}/H increased with increasing W and flow duration for both a Newtonian ($n = 1$) and a shear-thinning fluid ($n = 0.5$).

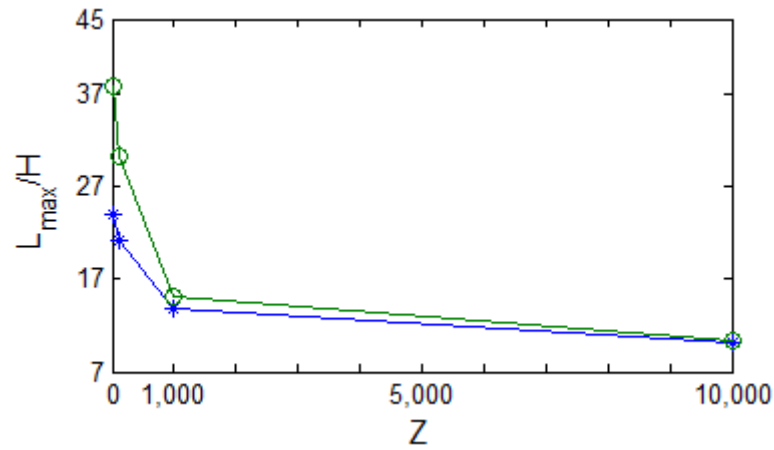
The benefits of performing non-dimensional analysis are generally two fold. First, the non-dimensional form of the model reduces the amount of the simulation required for analysis by reducing the number of variables. Secondly, it allows the assessment of the relative impact of a parameter with respect to another parameter. For instance, the dimensionless variable $Z \left(\frac{\eta}{E} \left(\frac{EH}{Tm} \right)^{\frac{1}{n}} \right)$ can be considered to evaluate the impact of the tissue

viscous component on the spreading extent with respect to the fluid shear-thinning index for a given W .

The interaction between the dimensionless parameters W and Z was examined in terms of their impact on the dimensionless spreading length. W represents the relative effect of the tissue elasticity with respect to tissue thickness and Z represents the relative effect of the tissue viscous-coefficient with respect to tissue elasticity and thickness for a given fluid consistency m , and shear-thinning index n . Figures 3.9 (a) and (b) show that at the same dimensionless time ($\bar{t} = 5000$) the non-dimensional spreading length decreased as the variable Z increased with different magnitudes of W . This trend is consistent with the one observed in the dimensional study, namely as the boundary viscous-coefficient increased the spreading length decreased for different tissue elasticity.



(a) $n = 0.8$



(b) $n = 1$ (Newtonian fluid)

Figure 3.9: (a) – (b) The dimensionless spreading length (L_{max}/H) at dimensionless time $\bar{t} = 5000$ as function of the variable Z for two different values of W and different cases of fluid

shear-thinning index. $Z = \frac{\eta}{E} \left(\frac{EH}{Tm} \right)^{\frac{1}{n}}$, $W = \frac{T\rho g_x}{E}$

The dimensionless length (L_{max}/H) decreased as the variable Z increased for different values of W and shear-thinning index n .

3.4 Conclusions

The goal of this study was to compare the impact of viscoelastic boundaries and pure elastic boundaries in terms of their effect on the spreading behaviour of different formulations of microbicidal gels. Based on the numerical results, we concluded that there is a difference between linear elastic and linear viscoelastic tissue impact on the flow of a gel. The degree of difference between pure elastic and viscoelastic boundaries depends on the relative magnitudes of the tissue modulus of elasticity and of the viscous-coefficient. The difference was more evident with relatively larger values of the tissue viscous component. In

other words, when larger energy is dissipated during the straining of the tissue. During the spreading of the bolus, the tissue undergoes continuous straining and doesn't recover fully due to the energy loss. As the tissue elasticity increased, the impact of the tissue viscous effect diminished.

Additionally, the tissue viscous-coefficient affects the spreading behaviour of the fluid at different levels depending on the fluid rheological properties. The viscous-coefficient has more impact on the spreading extent for a gel with a high shear-thinning index and a low consistency. It is expected that after the gel is applied to the vaginal canal, the gel will mix with the vaginal fluids and be diluted. The dilution of the gel after application would lead to a decrease in its consistency and increase in its shear-thinning index and subsequently the impact of the tissue viscous component on the diluted gel would be greater. This change in the gel properties is particularly important as it would affect the performance and efficacy of the gel. Therefore, during the design and optimization of microbicidal gels, it is important to take into consideration the dilution of the gel and the subsequent impact of the viscoelastic properties of the vaginal tissue on the spreading behaviour of the gel.

The change in the spreading behaviour with the different combinations of tissue and fluid properties indicates the importance of specifying suitable fluid rheological properties for certain tissue properties to obtain maximum spreading and hence optimal coating of the targeted surfaces. Vaginal tissue with a low modulus of elasticity and a high viscous component would have a relatively low potential to spread the gel, therefore choosing a gel with a high shear-thinning index and low consistency would help extend the spreading of the gel. Whereas, in the case of a tissue with higher elasticity and low viscous-coefficient, choosing a gel with a relatively high consistency and a low shear-thinning index would be provide sufficient spreading as high tissue elasticity would result in higher squeezing forces. However, it is also important to keep in mind that the spreading extent would also depend on

the application time and on the level of the dilution. Longer application times and high levels of dilution would lead to more spreading.

This study was an initial attempt at incorporating the viscoelastic properties of the vaginal tissue in a numerical model to simulate the flow of microbicidal gels. The results of this study help increase the understanding of the interaction between the tissue mechanical properties and the fluid rheological properties. Therefore, this study expands the framework for investigating the spreading behaviour of microbicidal gels under the influence of gravitational and squeezing forces due to the biomechanical properties of the vaginal tissue.

One of the major limitations of this study is the theoretical model was a 2D flow model (1D spreading), which means the flow of the fluid was simulated only in the axial direction. However, in a real world application, a microbicidal gel will flow in both the axial, as well as in the lateral direction. Expanding the current model to a 3D model would be advantageous. A 3D model would account for the spreading in both directions and provide insights into the overall spreading behaviour of the gel in the two different directions. However, it is important to recognize the difficulties in developing a 3D model. These difficulties include the specification of the flow geometry as the vaginal canal is asymmetric and doesn't conform to conventional shapes. Due to the asymmetry of the vaginal canal, the spreading behaviour of the gel in the lateral and axial directions would likely be different and potentially affected by changes in the tissue viscoelasticity along the axial and lateral directions. Additionally, numerical simulations with a 3D model would involve a substantial increase in the computational time. For the strain calculation, we considered the deformation of the tissue in the normal direction only. In a real application, the bolus might cause the tissue to stretch in the circumferential, as well as in the radial direction. For future studies, a better representation and estimation of the strain would help in understanding the response of the tissue. Another limitation is that the bolus was considered to be symmetrical about the

vertical axis and to spread in the vertical direction at all times. In a real application, the bolus might be placed at different angles and the symmetry assumption would no longer be valid.

The characterization of the vaginal tissue is limited and the lack of data for the biomechanical properties of the tissue limits the relevance of the ranges considered for the biomechanical properties in this study. The tissue biomechanical properties and tissue thickness are expected to vary with age, parity, and menopause. The results of this study clearly show the importance and the significance of measuring the biomechanical properties of the vaginal tissue *in vivo*. The characterization of the tissue viscoelastic properties would not only help in developing more accurate and more relevant numerical models, but also play a major role in validating the numerical studies. Changes in the vaginal tissue thickness would directly influence the degree at which the tissue would be strained, therefore impacting the tissue response level and subsequently influencing the spreading extent of the gel. It is critical to consider the aforementioned factors in the development of microbicidal gels, as they would greatly influence the spreading extent of the gels and hence their efficacy.

In this study, a simple linear viscoelastic model was used to represent the viscoelastic properties of the vaginal tissue. With the simple model we were able to represent the pressure term of the numerical flow model explicitly as the normal stress in the tissue. Complex and non-linear viscoelastic models would be more representative of the tissue response. However, with these complex and non-linear models, it is not always possible or simple to get an explicit equation for the stress. Future studies with such models would require fluid-structure interaction (FSI) methods to improve the understanding of how the viscoelastic tissue responds to the fluid and how this response influences the flow behaviour.

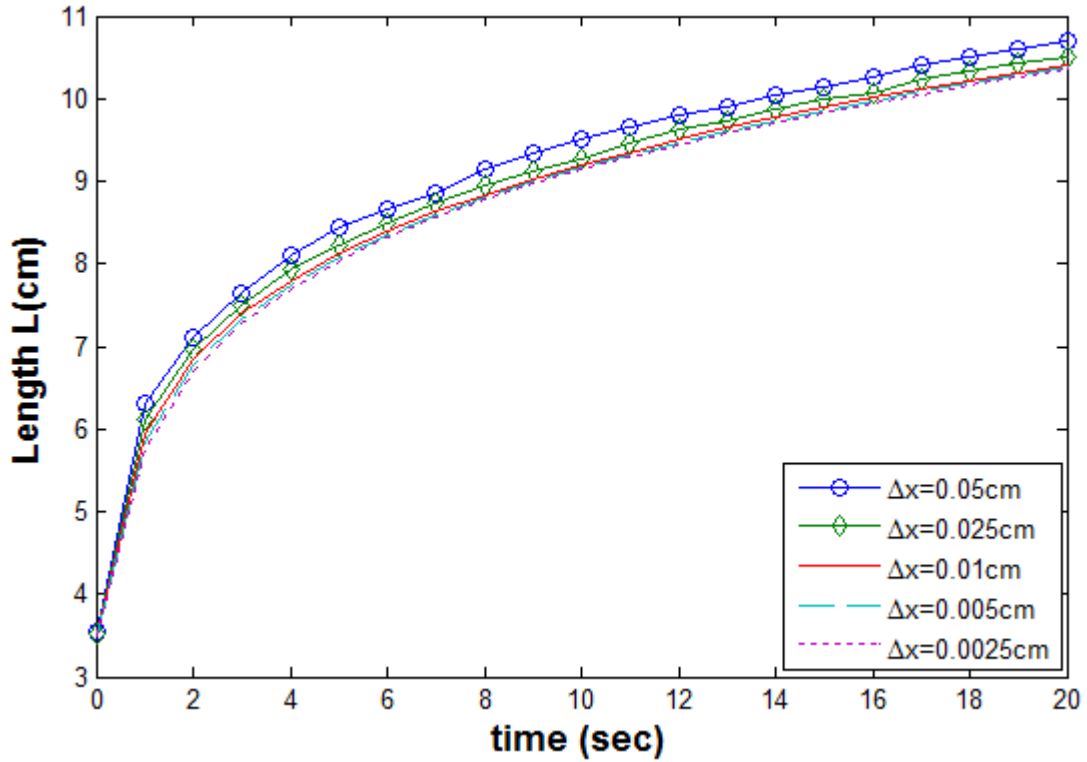
The numerical model was developed with the power-law fluid constitutive equation. Using other constitutive models for the non-Newtonian fluid would help increase the understanding of the interaction between the viscoelastic characteristics of the tissue and the

rheological properties of a microbicidal gel. For instance, the Ellis constitutive model has the ability to capture the behaviour of the fluid at low shear rates. Additionally a constitutive model that would incorporate the viscoelasticity of the fluid would be especially beneficial, as it would allow the comparison between the relative effects of the viscoelasticity of the fluid and of the tissue. Tissue and fluid with high relaxation times might require longer application time to ensure complete spreading and coating of the targeted surfaces. Lower tissue relaxation time would likely result in faster and greater spreading of the gel, especially for a fluid with a low relaxation time. The incorporation of the fluid viscoelasticity in a numerical model such as the one presented in this study is a challenging task. The constitutive equation of a viscoelastic fluid involves many time dependent parameters making the derivations as well as the numerical simulations a challenging undertaking. A fluid-structure interaction model would be especially useful in better understanding the interaction between the viscoelastic fluid and the viscoelastic tissue.

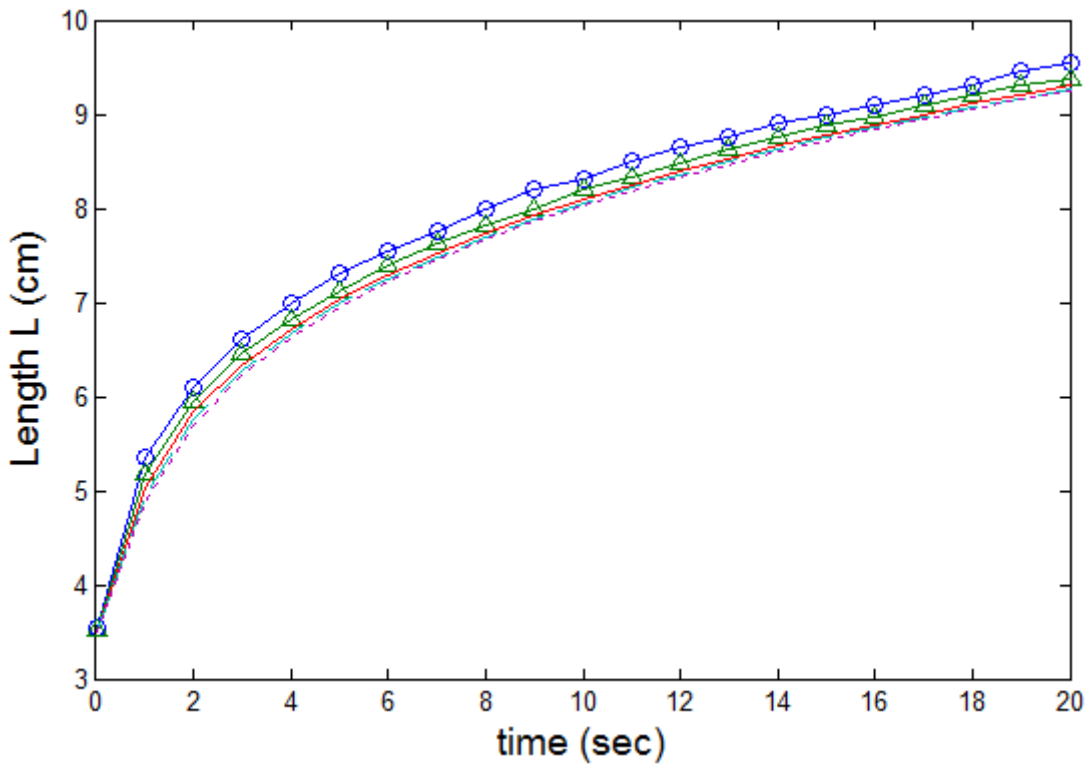
4. Model validation and additional results

4.2 Convergence study

Convergence studies are typical procedures performed to check the accuracy of the numerical simulations. Generally, a convergence study involves the refinement of the mesh resolution. The refinement of the spatial computational mesh is achieved by increasing the number of the nodes used in the computations and subsequently increasing the number of the computational steps. In this study, a series of mesh refinement were conducted. The mesh refinement was achieved by incrementally decreasing the computational spatial step size Δx until the change in the numerical results became negligible. Figure 4.1 (a) and (b) shows the change in the spreading length over time for different mesh resolutions. Both plots in Figure 4.1 show that as the step size Δx became smaller the change in the spreading length became smaller.



(a) $E = 50\text{kPa}$, $\eta = 1\text{kPa}\cdot\text{s}$, $n = 0.8$ and $m = 400 \text{ P}\cdot\text{s}^{n-1}$



(b) $E = 50\text{kPa}$, $\eta = 1\text{kPa}\cdot\text{s}$, $n = 1$ (Newtonian fluid), and $m = 600 \text{ P}\cdot\text{s}^{n-1}$.

Figure 4.1: (a) – (b) The convergence results with different combinations of tissue viscoelastic parameters (E and η) and fluid's properties (shear-thinning index n and consistency m) elasticity.

The plots (a) and (b) illustrate the change in spreading length over time for different mesh resolutions. With the step sizes $\Delta x = 0.01, 0.005, \text{ and } 0.0025$ cm, the change in the spreading length was very small.

Tables 4.1 and 4.2 illustrate the percentage change in the maximum length L_{max} , computed with different mesh resolutions. The percentage change in L_{max} was defined as:

$$\% \text{ change in } L_{max} = \frac{L_{max} - L_{max,\Delta x=0.0025}}{L_{max}} \times 100 \quad (4.1)$$

where L_{max} is the maximum length computed for a given Δx and $L_{max,\Delta x=0.0025}$ is the maximum length computed with the resolution $\Delta x = 0.0025$ cm.

For the convergence study, we considered a case with a Newtonian fluid ($n = 1, m = 600 \text{ P}\cdot\text{s}^{n-1}$) and a case with a power-law fluid ($n = 0.8, m = 400 \text{ P}\cdot\text{s}^{n-1}$), where the viscoelasticity parameters E and η were chosen as 50 kPa and 1 kPa·s respectively, as these magnitudes of the viscoelastic parameters are expected to make the fluid spread faster.

Δx (cm)	Length L_{max} (cm)	% change in L_{max}
0.05	10.7	3.382
0.025	10.5	1.450
0.01	10.4	0.483
0.005	10.37	0.193
0.0025	10.35	0

Table 4.1: Spatial mesh refinement for a power-law fluid with shear-thinning $n = 0.8$ and consistency $m = 400 \text{ P}\cdot\text{s}^{n-1}$

Δx (cm)	Length L_{max} (cm)	% change in L_{max} , relative to $\Delta x = 0.0025$ cm
0.05	9.55	3.271
0.025	9.375	1.379
0.01	9.31	0.676
0.005	9.27	0.244
0.0025	9.2475	0

Table 4.2: Spatial mesh refinement for a case of Newtonian fluid ($n = 1$) with a consistency $m = 600 \text{ P}\cdot\text{s}^{n-1}$

For both the Newtonian and non-Newtonian cases, the convergence study revealed that the mesh resolution with the spatial step size $\Delta x = 0.01$ cm was sufficiently fine to ensure accurate numerical results. In both cases the percent change in the spreading length L_{max} was less than 1% relative to the finest mesh resolution $\Delta x = 0.0025$ cm, which required much longer computational time for the power-law fluid case as well as for the Newtonian fluid case. Table 4.3 shows the computational time required (hours : minutes) to simulate the flow for 20 seconds.

Case	$\Delta x = 0.01$ cm	$\Delta x = 0.0025$ cm
Power-Law fluid	2 : 24	10 : 50
Newtonian fluid	1 : 38	7 : 01

Table4.3: Computational time required with different mesh resolutions

Mesh resolution with step size $\Delta x = 0.01$ cm was chosen for all computational simulations, as this resolution was computationally less expensive and changes in the computational results were very small. It is worth mentioning that Karri also used a spatial step size of $\Delta x = 0.01$ cm, after performing a convergence study with a Newtonian case and power-law fluid case with the linear elastic boundaries [19].

4.2 Conservation of mass check

As a second verification method, we performed mass-conservation check of the fluid-bolus for numerous simulation cases with combination sets of the variables E , η , m , and n . The mass of the bolus (i.e. the area of the bolus, since a 2D model was considered) was computed for each computational time step. Figure 4.2 shows the mass of the fluid-bolus was constant over the computational time, indicating the conservation of mass during the entire simulation time.

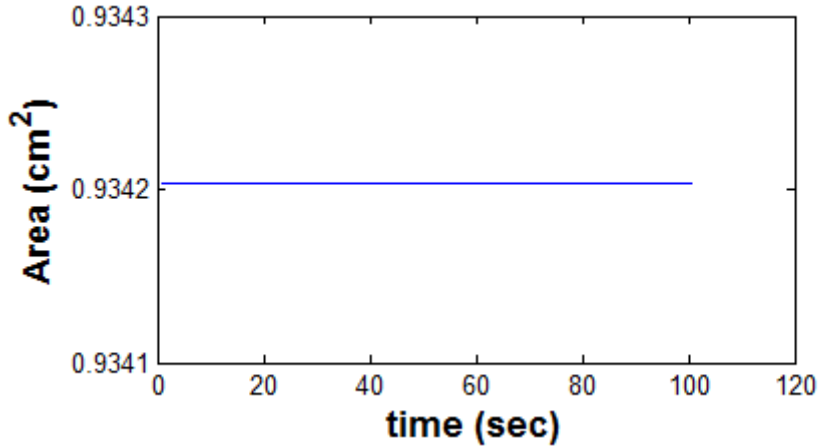


Figure 4.2: The conservation of mass of the fluid-bolus over the computational time

Additionally, we compared several results from the study of flow between elastic boundaries [19] by setting the tissue's viscous-coefficient $\eta = 0 \text{ P}\cdot\text{s}^{\text{n-1}}$ in the code. The results from both flow models were identical. By performing the convergence study and checking the conservation of mass of the bolus, we were able to verify the accuracy of the numerical results and validate our numerical model.

4.3 Numerical Methods

The non-linear partial differential equation both in the dimensional form as well as in the non-dimensional form was solved numerically. Initially, two numerical methods were considered in this study, namely the backward Euler method and the Crank-Nicolson method. After comparing the two numerical methods, it was determined that the backward Euler method was computationally more efficient and therefore was chosen for all simulations. A finite difference scheme based C-code, previously used by Kieweg [53] to simulate free surface gravity-driven flow model and by Karri [19] to simulate the flow between elastic boundaries were adapted and manipulated to simulate the flow between viscoelastic boundaries. Additionally, the new code was further manipulated to solve the non-dimensional evolution equation. The computations were executed on the computing cluster of the Information and Telecommunication Technology Center (ITTC) at the University of Kansas.

4.3.1 Discretization: *the theta-method (the θ -method)*

Using the θ -method, the evolution equation's discretization is expressed as:

$$\frac{h_i^{p+1} - h_i^p}{\Delta t} + \theta f_i^{p+1} + (1 - \theta)f_i^p = 0 \quad (4.2)$$

Where $0 \leq \theta \leq 1$, the indices p and $p+1$ refer to the current time and next time respectively, and Δt is the time step size [51].

When $\theta = 0$ the method gives the explicit forward Euler scheme, which was not considered in this study due the potential of numerical instability. When $\theta = 1$ the method yields the implicit backward Euler scheme and when $\theta = 1/2$ the method gives the Crank–Nicolson scheme, both schemes are unconditionally stable [51].

4.3.1.1 Backward Euler method (fully implicit scheme)

Using the backward Euler scheme ($\theta = 1$), which has an error of order $O(\Delta t)$, the evolution equation is of the form:

$$\frac{h_i^{p+1} - h_i^p}{\Delta t} + f_i^{p+1} = 0, \text{ where } f = \frac{\partial q}{\partial x} \quad (4.3)$$

For the term $\frac{\partial q}{\partial x}$, the central difference spatial discretization, which has an error of order $O(\Delta x)^2$, was used with the computational stencil shown in figure 4.3.

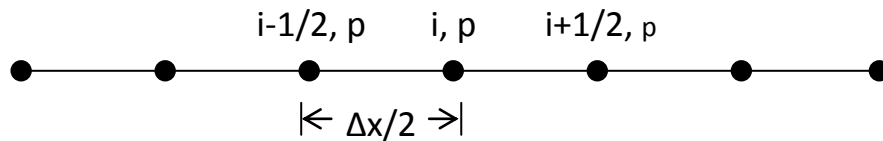


Figure 4.3: central difference around the i th node

The equation evolution equation becomes:

$$\frac{h_i^{p+1} - h_i^p}{\Delta t} + \frac{q_{i+\frac{1}{2}}^{p+1} - q_{i-\frac{1}{2}}^{p+1}}{\Delta x} = 0 \quad (4.4)$$

In a similar way, we discretize the two terms: $q_{i+\frac{1}{2}}^{p+1}$ and $q_{i-\frac{1}{2}}^{p+1}$ using the central difference discretization around the nodes $i + \frac{1}{2}$ and $i - \frac{1}{2}$ respectively. First, we show the discretization of the mixed derivatives term $\frac{\partial^2 h}{\partial x \partial t}$:

$$\begin{aligned} \frac{\partial^2 h}{\partial x \partial t} &= \frac{\partial}{\partial t} \left(\frac{\partial h}{\partial x} \right) = \frac{\left(\frac{h_{i+1} - h_i}{\Delta x} \right)^{p+1} - \left(\frac{h_{i+1} - h_i}{\Delta x} \right)^p}{\Delta t} \\ &= \frac{h_{i+1}^{p+1} - h_{i+1}^p - h_i^{p+1} + h_i^p}{\Delta x \Delta t} \end{aligned} \quad (4.5)$$

Figure 4.4 shows the footprint of the computational stencil used for the special and time discretizations:

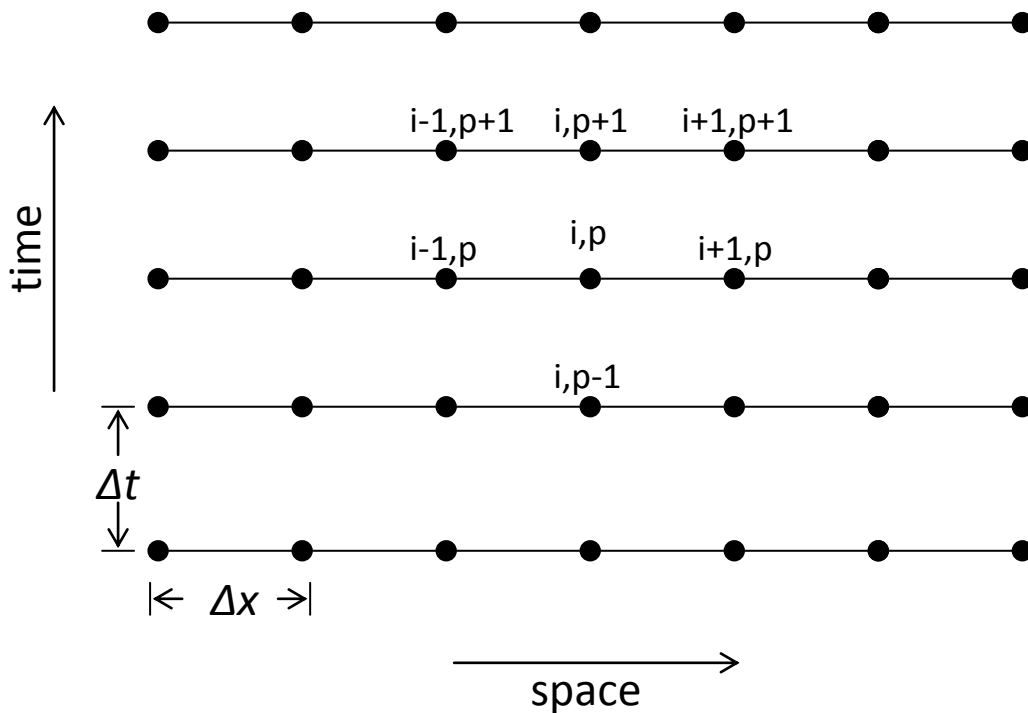


Figure 4.4: Implicit finite difference discretization

For the q -terms, we get:

$$\begin{aligned}
q_{i+\frac{1}{2}}^{p+1} = & \frac{-n}{m^{1/n}(2n+1)} \left(\frac{E h_{i+1}^{p+1} - h_i^{p+1}}{\Delta x} + \frac{\eta h_{i+1}^{p+1} - h_{i+1}^p - h_i^{p+1} + h_i^p}{\Delta x \Delta t} \right. \\
& \left. - \rho g \right) \left(\frac{E h_{i+1}^{p+1} - h_i^{p+1}}{\Delta x} + \frac{\eta h_{i+1}^{p+1} - h_{i+1}^p - h_i^{p+1} + h_i^p}{\Delta x \Delta t} \right. \\
& \left. - \rho g \right)^{\frac{1}{n}-1} \left(\frac{h_{i+1}^{p+1} + h_i^{p+1}}{2} \right)^{2+\frac{1}{n}} \tag{4.6}
\end{aligned}$$

$$\begin{aligned}
q_{i-\frac{1}{2}}^{p+1} = & \frac{-n}{m^{1/n}(2n+1)} \left(\frac{E h_i^{p+1} - h_{i-1}^{p+1}}{\Delta x} + \frac{\eta h_i^{p+1} - h_i^p - h_{i-1}^{p+1} + h_{i-1}^p}{\Delta x \Delta t} \right. \\
& \left. - \rho g \right) \left(\frac{E h_i^{p+1} - h_{i-1}^{p+1}}{\Delta x} + \frac{\eta h_i^{p+1} - h_i^p - h_{i-1}^{p+1} + h_{i-1}^p}{\Delta x \Delta t} \right. \\
& \left. - \rho g \right)^{\frac{1}{n}-1} \left(\frac{h_i^{p+1} + h_{i-1}^{p+1}}{2} \right)^{2+\frac{1}{n}} \tag{4.7}
\end{aligned}$$

4.3.1.2 Modified Crank-Nicolson method:

Using the Crank-Nicolson method, the evolution equation is of the form:

$$\frac{h_i^{p+1} - h_i^p}{\Delta t} + \frac{1}{2} f_i^{p+1} + \frac{1}{2} f_i^p = 0, \text{ where } f = \frac{\partial q}{\partial x} \tag{4.8}$$

The equation becomes:

$$\frac{h_i^{p+1} - h_i^p}{\Delta t} - \frac{1}{2} \left[\frac{q_{i+\frac{1}{2}}^{p+1} - q_{i-\frac{1}{2}}^{p+1} + q_{i+\frac{1}{2}}^p - q_{i-\frac{1}{2}}^p}{\Delta x} \right] = 0 \tag{4.9}$$

The Crank-Nicolson method has error of orders $O(\Delta t)$ and $O(\Delta x)^2$. Following the same discretization steps as before, the terms are given by:

$$\begin{aligned}
q_{i+\frac{1}{2}}^{p+1} = & \frac{-n}{m^{1/n}(2n+1)} \left(\frac{E h_{i+1}^{p+1} - h_i^{p+1}}{\Delta x} + \frac{\eta h_{i+1}^{p+1} - h_{i+1}^p - h_i^{p+1} + h_i^p}{\Delta x \Delta t} \right. \\
& \left. - \rho g \right) \left(\frac{E h_{i+1}^{p+1} - h_i^{p+1}}{\Delta x} + \frac{\eta h_{i+1}^{p+1} - h_{i+1}^p - h_i^{p+1} + h_i^p}{\Delta x \Delta t} \right. \\
& \left. - \rho g \right)^{\frac{1}{n}-1} \left(\frac{h_{i+1}^{p+1} + h_i^{p+1}}{2} \right)^{2+\frac{1}{n}} \tag{4.10}
\end{aligned}$$

$$\begin{aligned}
q_{i-\frac{1}{2}}^{p+1} &= \frac{-n}{m^{1/n}(2n+1)} \left(\frac{E h_i^{p+1} - h_{i-1}^{p+1}}{T \Delta x} + \frac{\eta h_i^{p+1} - h_i^p - h_{i-1}^{p+1} + h_{i-1}^p}{T \Delta x \Delta t} \right. \\
&\quad \left. - \rho g \right) \left| \left(\frac{E h_i^{p+1} - h_{i-1}^{p+1}}{T \Delta x} + \frac{\eta h_i^{p+1} - h_i^p - h_{i-1}^{p+1} + h_{i-1}^p}{T \Delta x \Delta t} \right. \right. \\
&\quad \left. \left. - \rho g \right) \right|^{\frac{1}{n}-1} \left(\frac{h_i^{p+1} + h_{i-1}^{p+1}}{2} \right)^{2+\frac{1}{n}}
\end{aligned} \tag{4.11}$$

$$\begin{aligned}
q_{i+\frac{1}{2}}^p &= \frac{-n}{m^{1/n}(2n+1)} \left(\frac{E h_{i+1}^p - h_i^p}{T \Delta x} + \frac{\eta h_{i+1}^{p+1} - h_{i+1}^p - h_i^{p+1} + h_i^p}{T \Delta x \Delta t} \right. \\
&\quad \left. - \rho g \right) \left| \left(\frac{E h_{i+1}^p - h_i^p}{T \Delta x} + \frac{\eta h_{i+1}^{p+1} - h_{i+1}^p - h_i^{p+1} + h_i^p}{T \Delta x \Delta t} \right. \right. \\
&\quad \left. \left. - \rho g \right) \right|^{\frac{1}{n}-1} \left(\frac{h_{i+1}^p - h_i^p}{2} \right)^{2+\frac{1}{n}}
\end{aligned} \tag{4.12}$$

$$\begin{aligned}
q_{i-\frac{1}{2}}^p &= \frac{-n}{m^{\frac{1}{n}}(2n+1)} \left(\frac{E h_i^p - h_{i-1}^p}{T \Delta x} + \frac{\eta h_i^{p+1} - h_i^p - h_{i-1}^{p+1} + h_{i-1}^p}{T \Delta x \Delta t} \right. \\
&\quad \left. - \rho g \right) \left| \left(\frac{E h_i^p - h_{i-1}^p}{T \Delta x} + \frac{\eta h_i^{p+1} - h_i^p - h_{i-1}^{p+1} + h_{i-1}^p}{T \Delta x \Delta t} \right. \right. \\
&\quad \left. \left. - \rho g \right) \right|^{\frac{1}{n}-1} \left(\frac{h_i^p - h_{i-1}^p}{2} \right)^{2+\frac{1}{n}}
\end{aligned} \tag{4.13}$$

The modification in the Crank-Nicolson method was how the mixed derivatives term $\frac{\partial^2 h}{\partial x \partial t}$

was discretised. The term $\frac{\partial^2 h}{\partial x \partial t}$ was discretized using the full implicit backward Euler

method. Therefore, the introduced modified Crank-Nicolson method is basically a mixture of the backward Euler method and the conventional Crank-Nicolson method. The

Newton's method was used to solve the system of non-linear equations. The Newton's method was set to converge after a maximum of 10 iterations. A maximum error of

10^{-13} was set as the convergence criteria with an error tolerance of 10^{-8} . If the error tolerance was larger than 10^{-8} , an adaptive time stepping method was applied to reduce the time step Δt (initially set as $\Delta t = 10^{-3}$ sec) by a factor of 0.8 (20% reduction).

In order to save computational time, we exploited the symmetry in the flow domain (see Figure 3.2). Since we assumed no mass transfer along the vertical axis of the bolus (i.e. the symmetry line of the flow), the spreading behavior and pattern would be symmetrical about the vertical axis of the flow domain.

4.3.2 Backward Euler method vs. Crank-Nicolson method

In order to evaluate the efficiency and the accuracy of each of the two numerical methods, simulation cases were run with the same parameter sets. Table 4.4 presents the cases considered for the comparison of the two numerical methods, in addition to percent difference in the results and the time required to simulate the flow for 100 seconds. The cases chosen for this comparison are examples, which involve combinations of low and high values of the parameters n , m , E , η .

Parameter set [n , m ($P \cdot s^{n-1}$), E (kPa), η (kPa \cdot s)]	Numerical Method	Computational time [hours : minutes]	% change in results	
			Length(cm)	Height(cm)
[1, 100, 1, 10]	Backward-Euler	18:52	0	0.0476
	Crank-Nicolson	28:55		
[0.8, 300, 10, 5]	Backward-Euler	9:03	0	0.0102
	Crank-Nicolson	13:28		
[0.5, 600, 50, 1]	Backward-Euler	15:06	0	0.0013
	Crank-Nicolson	26:50		

Table4.4: Comparison between Backward-Euler method and the Crank-Nicolson method

It is clear that the Backward-Euler required much less time for the simulation compared to the modified Crank-Nicolson with negligible change in the numerical results. Therefore, the Backward Euler method was chosen for all simulations.

4.4 Additional results

In this section we provide additional plots and analysis that reiterate and reinforce the results presented and discussed in section 3.3. First, we briefly reiterate the concepts and the steps involved in deriving the numerical model. The derivation steps were based on the following concepts:

- Conservation of momentum
- Lubrication approximation
- Boundary conditions
- Constitutive equation of power-law fluid
- Conservation of mass

All five concepts were presented in details in section 3.3, except the lubrication approximation, also known as thin-film approximation. The lubrication approximation is valid when the characteristic length L of the thin film is considerably larger than its characteristic height H , as shown in figure 4.5, i.e. when the following inequalities hold:

$$H \ll L \quad (4.14)$$

$$\left(\frac{\rho u L}{\mu}\right) \left(\frac{H}{L}\right)^2 \ll 1 \quad (4.15)$$

Where, μ and ρ are the fluid's viscosity and density, respectively.

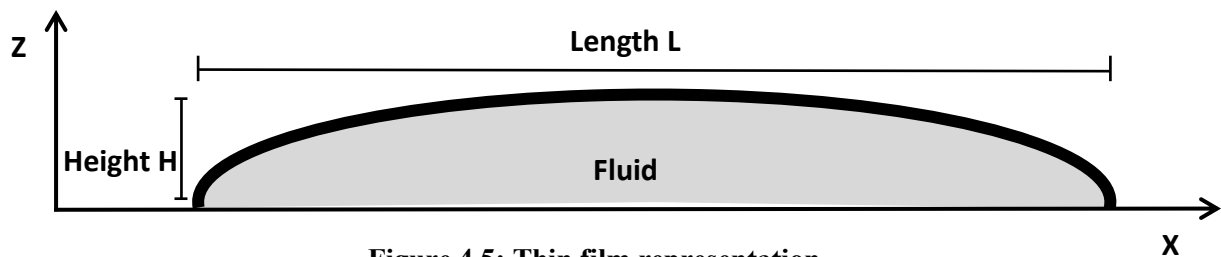


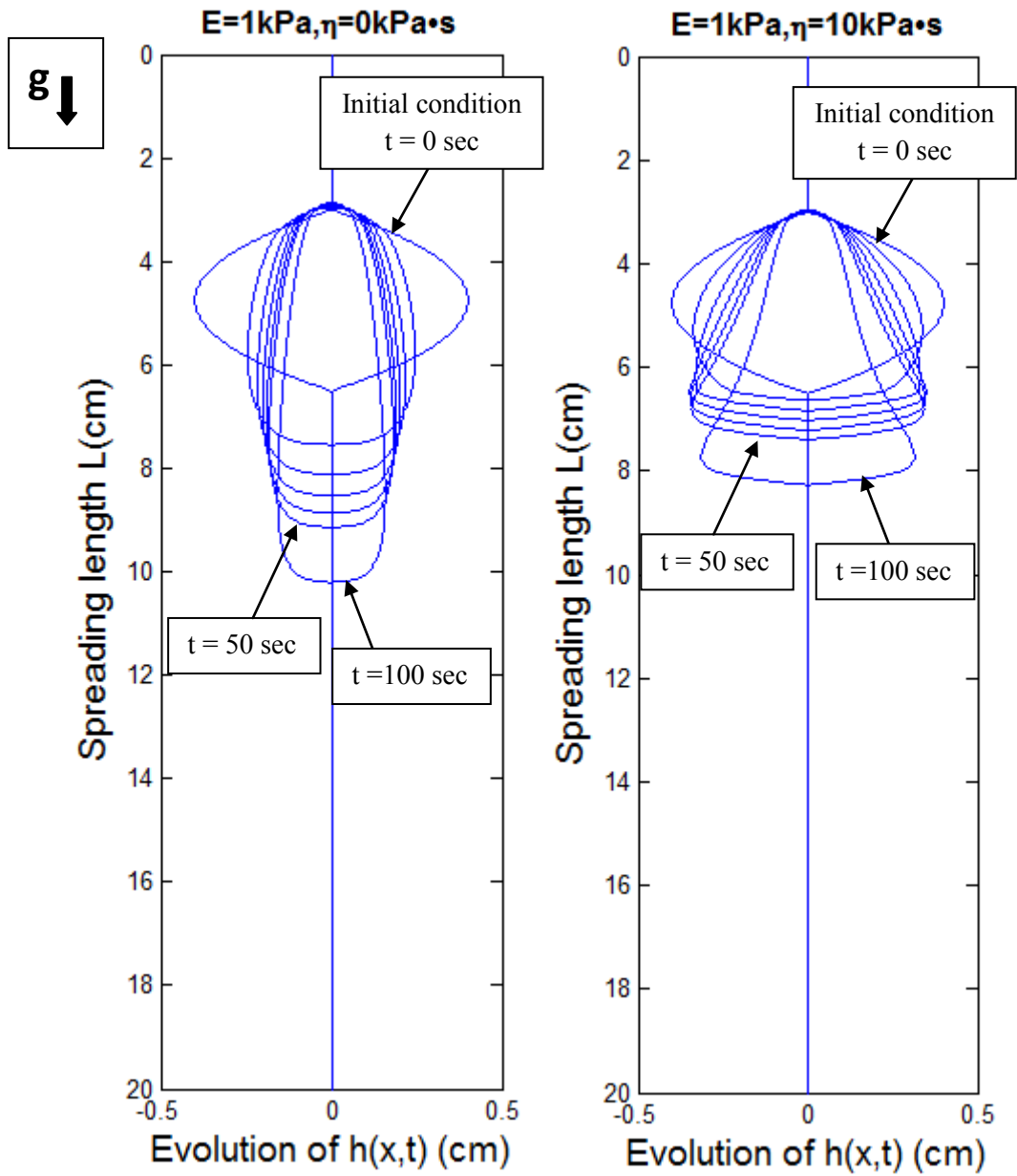
Figure 4.5: Thin film representation

Using this approximation, the inertial terms in the conservation of linear momentum can be neglected as the inertial terms are assumed to be dominated by the viscous term [50]. The lubrication approximation was used to simplify the conservation of linear momentum equation by neglecting the inertial terms in the equation.

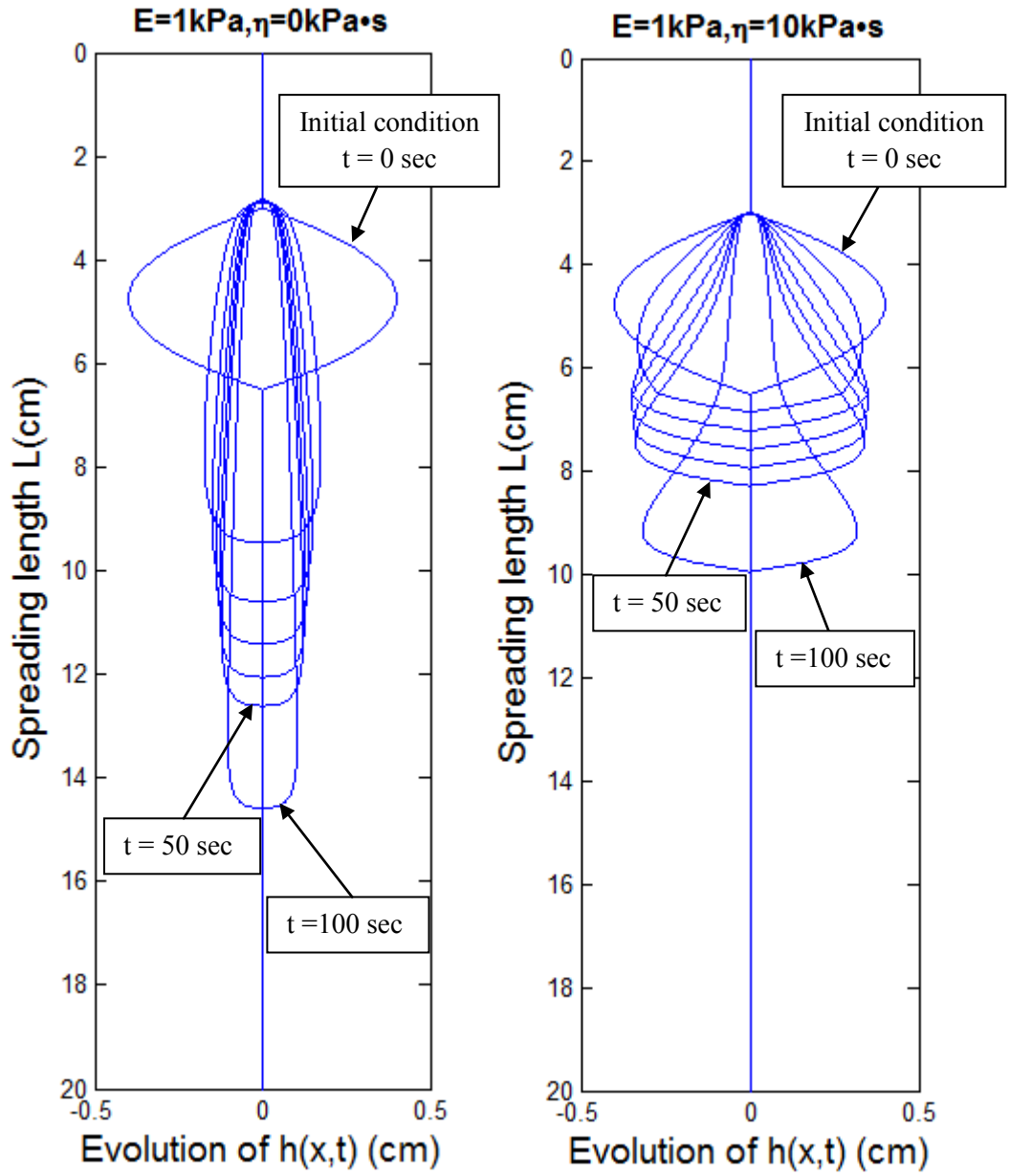
4.4.1 The difference between the viscoelastic and the elastic properties of the tissue on the flow behaviour of the fluid

The comparison of the flow patterns of the bolus under the influence of the tissue viscoelasticity and of the tissue elasticity only was the first step in assessing the impact of the viscoelastic characteristics of the tissue. In section 3.3 we showed an example that depicts the difference in the spreading profiles of the bolus over time for a fixed set of fluid consistency m and shear-thinning index n . Figure 4.6 shows additional flow profiles for different combinations of m and n values.

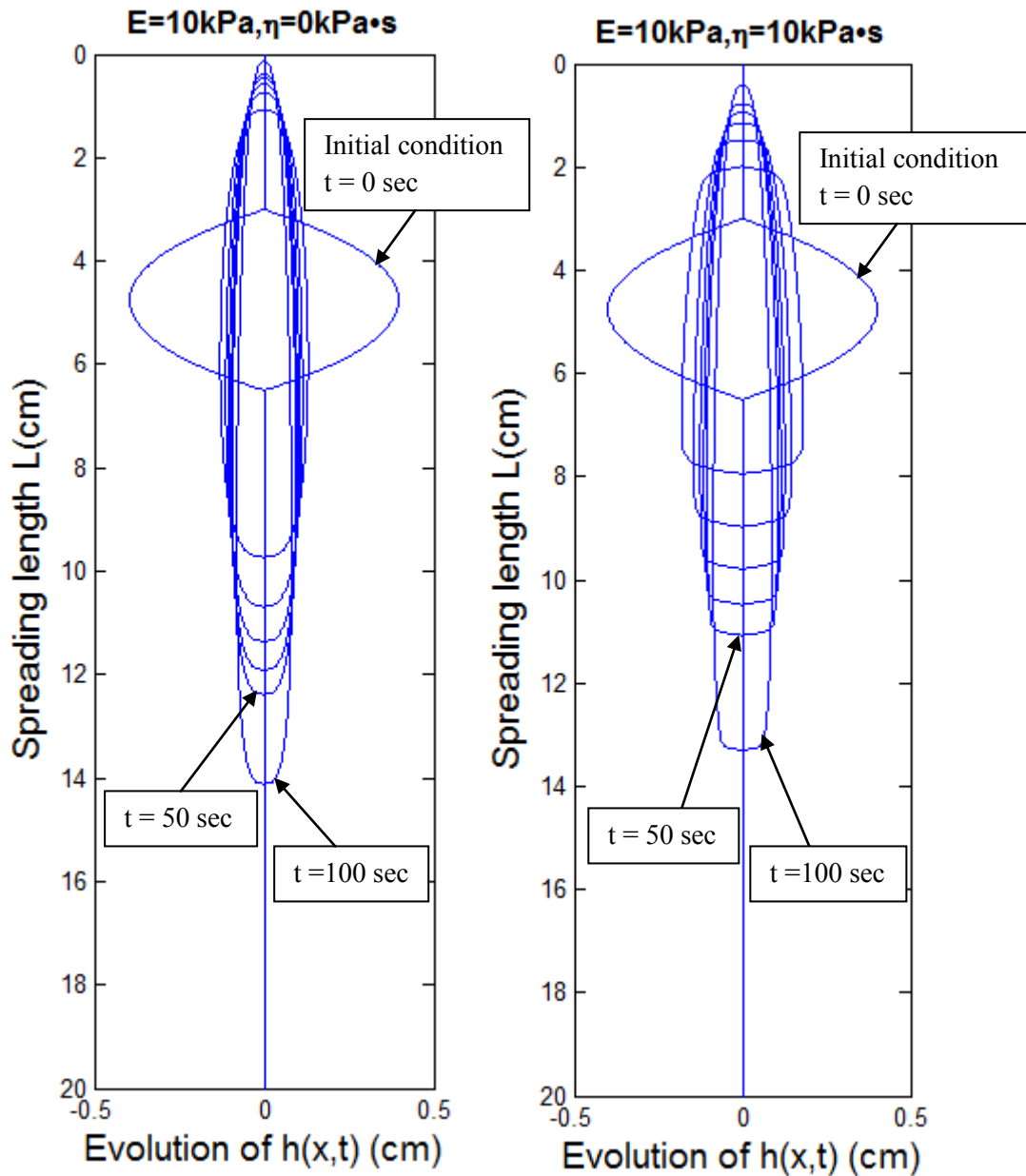
The spreading profiles presented in Figure 4.6 (a) - (d) show the evolution profiles of the bolus over time starting from the initial time $t = 0$ seconds at intervals of 10 seconds to $t = 50$ seconds and then at $t = 100$ seconds. From these profiles, one can notice that in some cases the direction of the flow was entirely downward and in other cases the flow occurred in both directions downward as well as upward. This trend is consistent with Karri's findings [19]. Karri determined that the direction of the flow is directly related to the relative effects of the tissue elasticity and the gravitational force. He found that with relatively low tissue elasticity, the gravitational effect dominates the flow hence the downward spreading and with high tissue elasticity, the squeezing effect dominates the flow hence the spreading in the downward as well as in the upward directions [19].



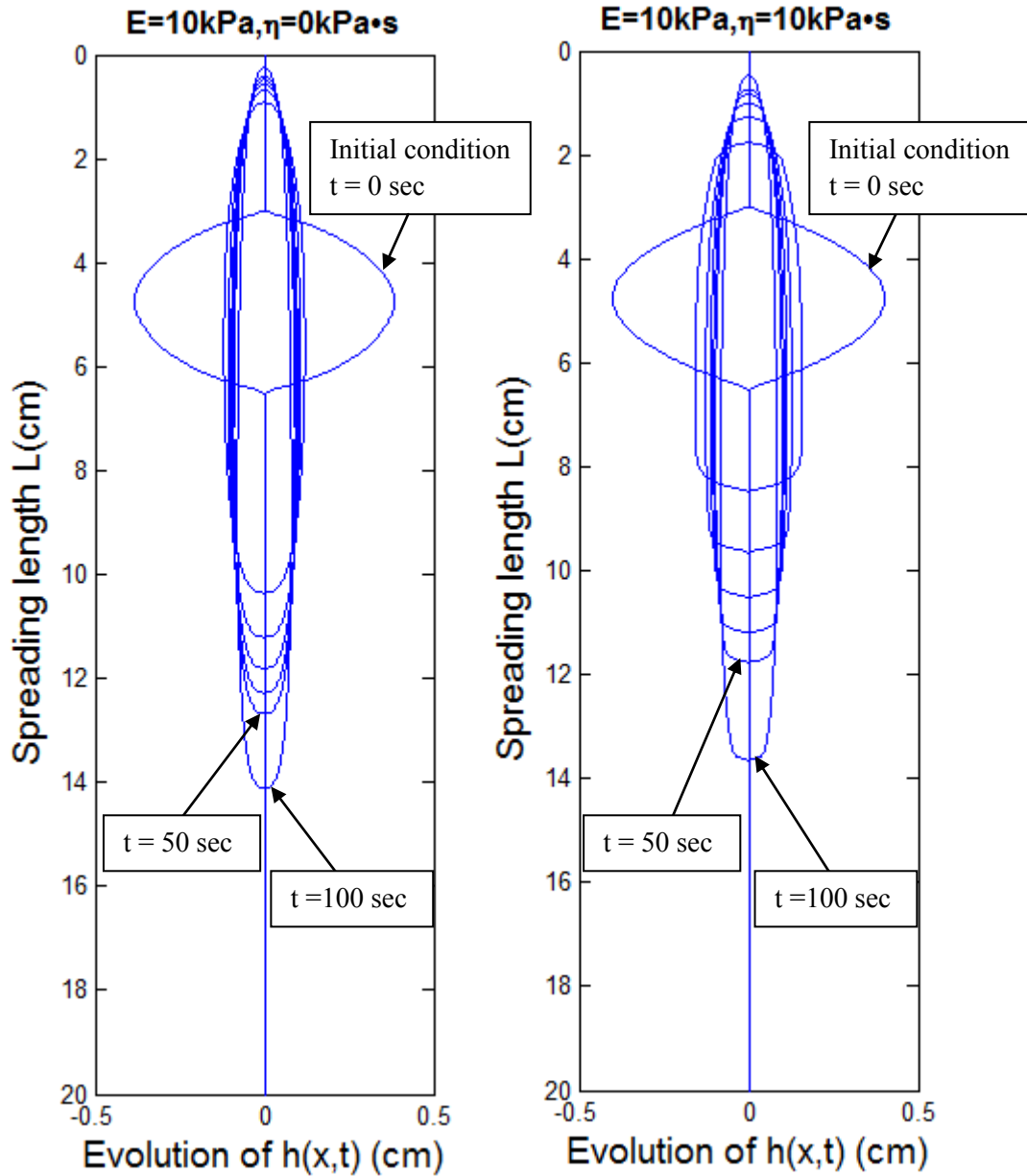
(a): $n = 0.6, m = 300 \text{ P}\cdot\text{s}^{n-1}$



(b): $n = 0.6, m = 100 \text{ P}\cdot\text{s}^{n-1}$



(c): $n = 0.9, m = 100 \text{ P}\cdot\text{s}^{n-1}$



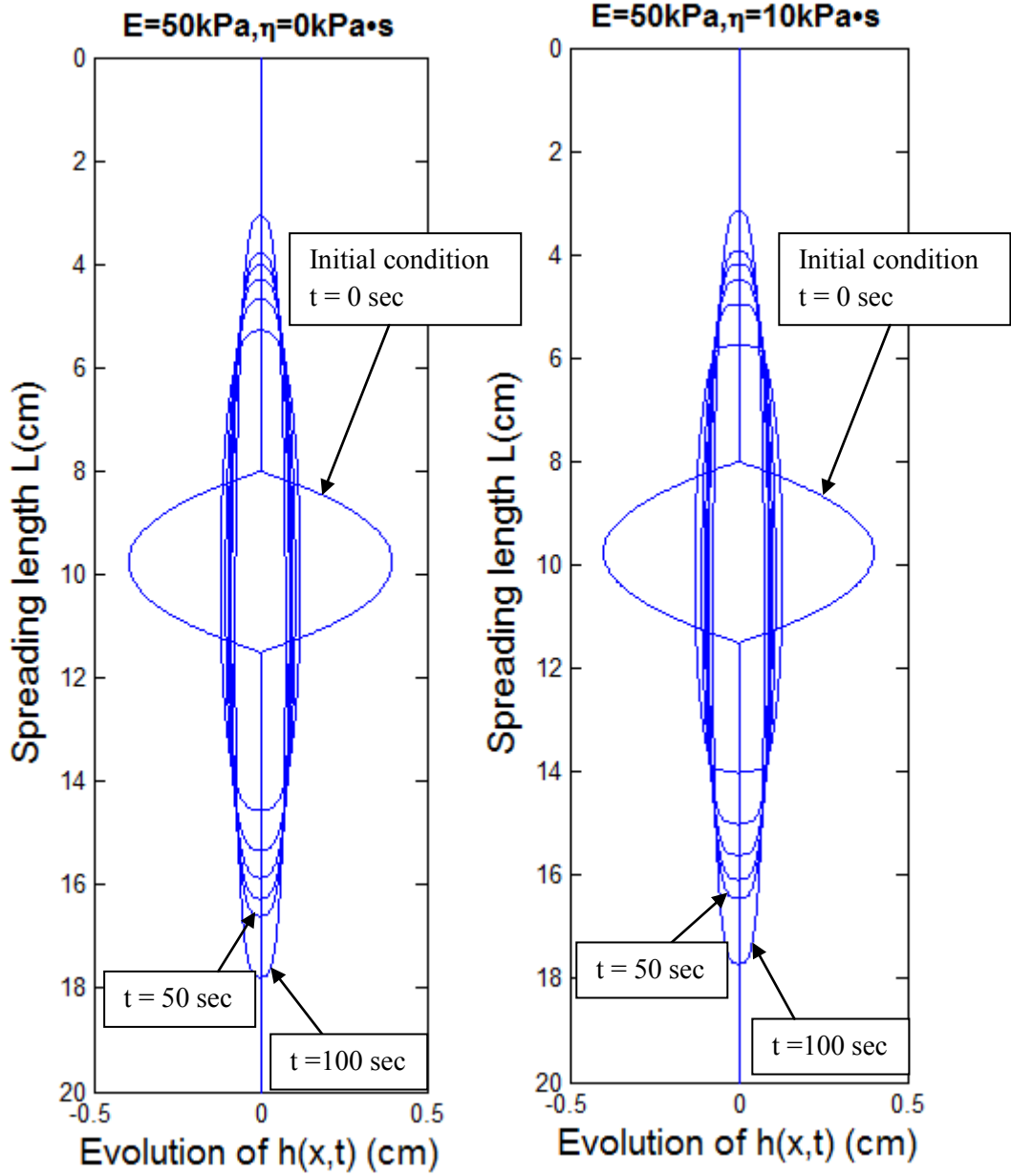
(d): $n = 0.6, m = 100 \text{ P}\cdot\text{s}^{-1}$

Figure 4.6: (a) – (d) Examples of flow profiles of power-law fluids with different combination of boundary elastic and viscous components, illustrating the effect of the elastic model and the viscoelastic model of the tissue.

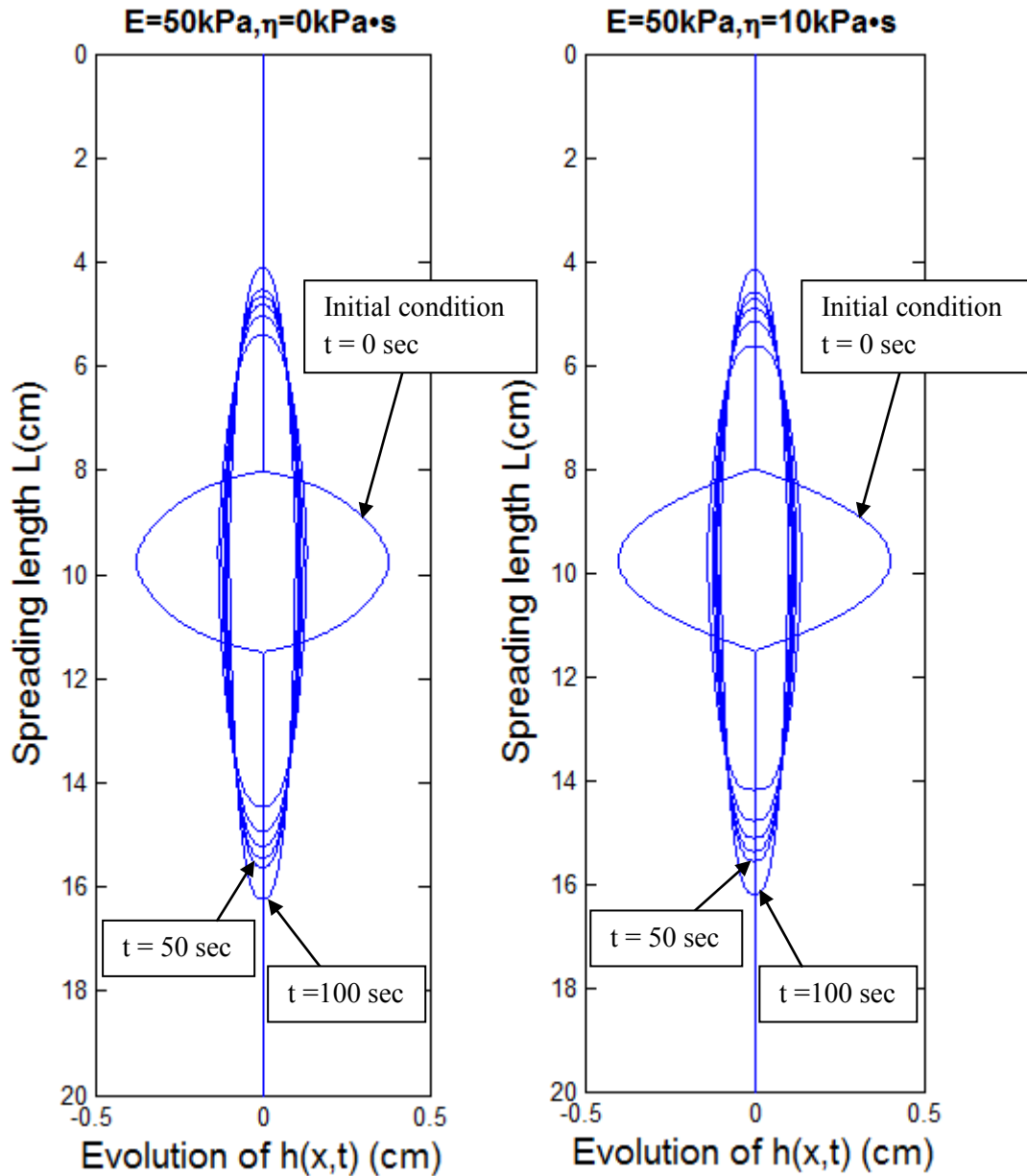
The impact of the boundary properties depends on the fluid's consistency m ((a) and (b)) and on the fluid's shear-thinning index n ((c) and (d)). The profiles are shown over time starting with the initial time $t = 0$ seconds at intervals of 10 seconds to $t = 50$ seconds and then at $t = 100$ seconds. Major difference between the elastic and the viscoelastic boundary was observed for large tissue viscous coefficient and low tissue elasticity (see Appendix A for more examples).

It is evident from the flow profiles, which compare the effect of pure elastic boundaries to the effect of viscoelastic boundaries, that the viscous-coefficient η has an impact on the flow patterns of the fluid. The impact of the parameter η was more noticeable with the two modulus of elasticity values $E = 1$ kPa and $E = 10$ kPa and with different fluid properties (see Figure A.1 in Appendix A for more examples of the spreading profiles).

The impact of the tissue viscous-coefficient seemed to diminish with the larger boundary elasticity $E = 50$ kPa regardless of the magnitude of the parameter η and the values of the fluid properties. Example profiles shown in Figure 4.7 (a) and (b) demonstrate how the elasticity E dominated the effect of the viscoelastic boundary on the flow of the bolus even with the larger value of $\eta = 10$ kPa·s.



(a): $n = 1, m = 300 \text{ P}\cdot\text{s}^{-1}$



(b): $n = 0.5, m = 600 \text{ P}\cdot\text{s}^{n-1}$

Figure 4.7: (a) – (b) Examples of the spreading profiles of the bolus with different rheological properties with large boundary elasticity $E = 50 \text{ kPa}$, showing the dominance of the elasticity of the boundary.

The spreading profiles are shown over time starting with the initial time $t = 0$ seconds at intervals of 10 seconds to $t = 50$ seconds and then at $t = 100$ seconds.

Overall, it is evident that the viscoelastic model and the elastic model of the tissue have different effects on the flow of the fluid. However, the difference between the two models seemed to diminish with larger tissue elasticity ($E = 50 \text{ kPa}$). In other words, the

impact of the tissue viscous parameter on the flow behaviour of the fluid depends primarily on the magnitude of the tissue elasticity E since the viscoelastic and the elastic models of the tissue resulted in very similar flow profiles independently of the fluid's properties. Therefore, the difference between the linear elastic and the linear viscoelastic models of the tissue is fundamentally associated with the relative magnitudes of the tissue's modulus of elasticity E and viscous-coefficient η .

With larger elasticity magnitudes, the viscoelastic boundaries behave more like elastic boundaries. For lower elasticity values ($E = 1$ and 10 kPa), the impact of the tissue viscous-coefficient was evident and the degree of impact appeared to depend on the fluid's consistency m (see profiles in Figure 4.6 (a) and (b)) and on the fluid's shear-thinning index n (see profiles in Figure 4.6 (c) and (d)).

As mentioned before, the difference between the spreading due pure elastic tissue and to viscoelastic tissue diminished with increasing modulus of elasticity E . Figure 4.8 shows that as the tissue elasticity E increased, the change in the spreading length became smaller and less apparent regardless of the tissue viscous-coefficient. Similar patterns were observed for different values of the shear-thinning index n and consistency m of the fluid (see Figure B.1 in Appendix B for more examples).

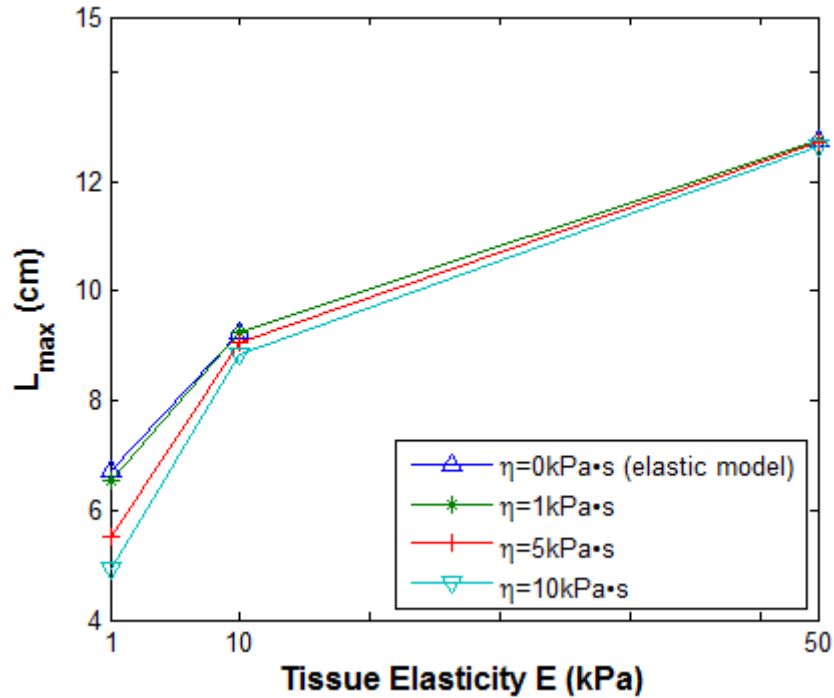


Figure 4.7: The spreading lengths of power law fluids with $n = 0.9$, $m = 600 \text{ P}\cdot\text{s}^{-1}$ for different tissue viscous-coefficient η and elasticity E .

The impact of the viscous-coefficient η depended on the elasticity E . As the elasticity increased the impact of the parameter η diminished. Similar trends were observed for various combinations of fluid shear-thinning index n and consistency m .

The relative magnitudes of the tissue viscous and elastic components can be compared using the relaxation time τ , which is the ratio of the viscous-coefficient η to the modulus of elasticity E . Figure 4.9 shows an example of the tissue relaxation time impact on the maximum spreading length for a power-law fluid case. The effect of the tissue relaxation time was strongest at lower tissue elasticity. The tissue relaxation time has little impact for larger elasticity.

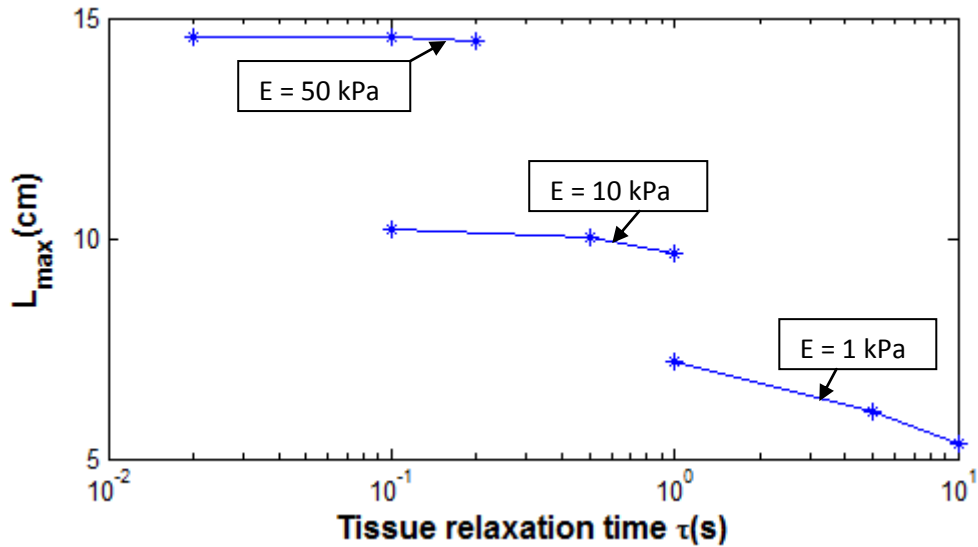


Figure 4.9: The effect of the tissue relaxation time on the maximum spreading length L_{max} of a power-law fluid with shear-thinning index $n = 0.6$, and consistency $m = 300 \text{ P}\cdot\text{s}^{n-1}$ at various tissue relaxation times $\tau = \eta / E$, where η and E are the tissue viscous and elastic component, respectively.

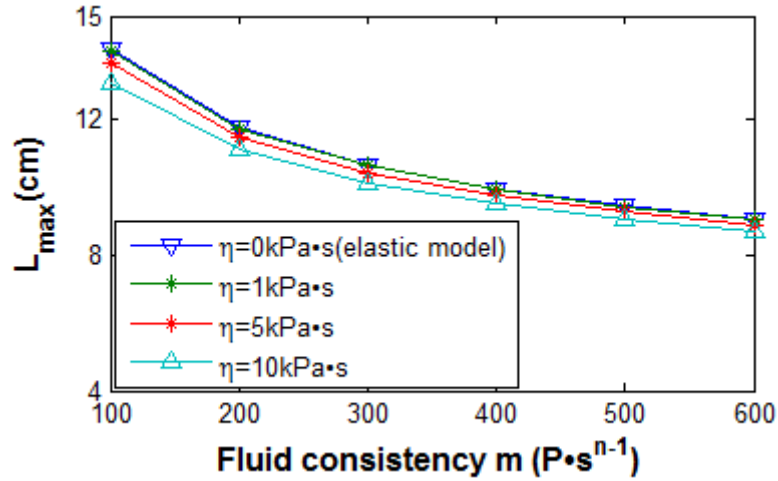
The tissue relaxation time τ has more impact at lower tissue elasticity and this impact diminished at higher elasticity.

4.4.2 The influence of the tissue viscous component on the flow of the fluid with different consistencies

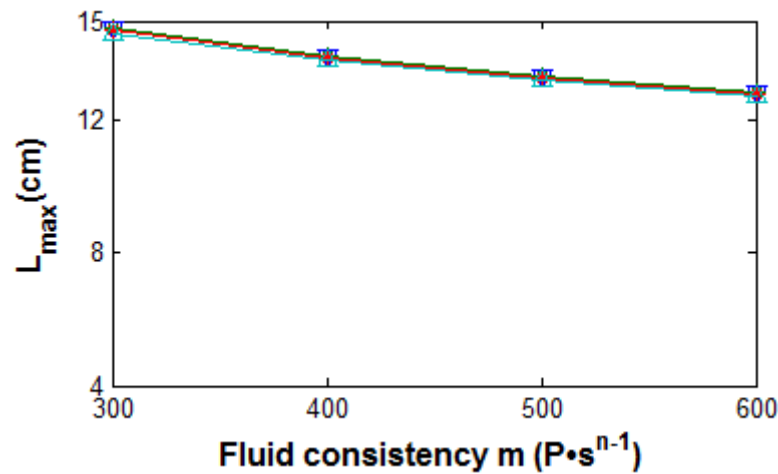
In this section, major results of the tissue viscous-coefficient impact on the flow of the bolus with different consistencies are presented and discussed. Figure 3.9 shows the spreading length vs. the fluid's consistency m for different values of the tissue viscous-coefficient η . As the consistency m increased the impact of the parameter η on the spreading length was less pronounced. This trend is consistent with previous results determined by Karri [19] section 3.1.3. The trend occurred with all sets of tissue elastic E and viscous η components, few examples of the trend are shown in Figure 4.10 (see Figure C.1 in Appendix C for additional examples). As noted in the previous section, the effect of the tissue viscous-coefficient η diminishes with increasing tissue elasticity E .

Overall, a similar trend was observed with all elasticities and shear-thinning indices, where the spreading length decreased as both the fluid's consistency and the tissue viscous component increased. Figure 3.9 is an example that illustrates the overall trend (see Figure C.1

in Appendix C for more examples). The results for the cases with the larger tissue elasticity ($E = 50\text{kPa}$) and low fluid consistency ($m = 100\text{ P}\cdot\text{s}^{n-1}$ and $200\text{ P}\cdot\text{s}^{n-1}$) are not shown because the spreading lengths reached the allowable maximum length of 15 cm much earlier than the selected simulation time of 100 seconds.



(a) $n = 0.8, E = 10\text{ kPa}$



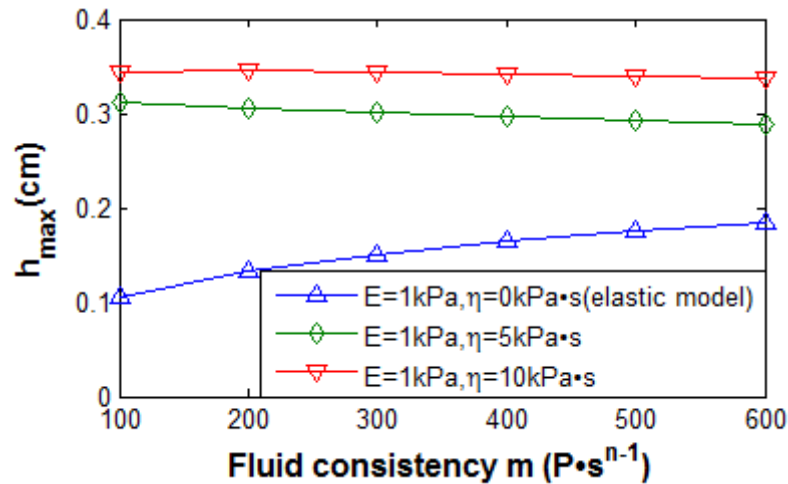
(a) $n = 1, E = 50\text{ kPa}$

Figure 4.10: (a) – (b) The maximum spreading length L_{max} of the bolus for various values of consistency m for different combinations of tissue elasticity E and fluid's shear-thinning index n .

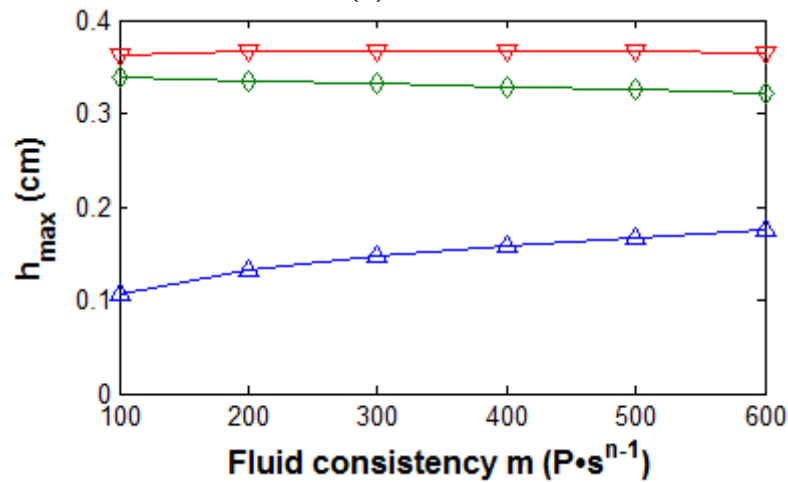
The impact of the tissue viscous-coefficient η on the spreading length L_{max} depends on the fluid's consistency m for all combinations of tissue elasticity E and fluid's shear-thinning index n . As m increased, the effect of η was less pronounced.

The decrease in the spreading length of the bolus when comparing different η values and different m values was accompanied by an increase in the bolus height. As mentioned in section 3.3, the change in the height was due to the viscous effects of the tissue. Initially, the

maximum bolus height was set to be 0.4 cm. Figure 4.11 shows the change in the maximum height h_{max} (height after 100 seconds) with increasing m values for different combinations of shear-thinning index and tissue viscoelastic parameters.



(a) $n = 0.8$



(b) $n = 1$

Figure 4.11: (a) – (b) the maximum bolus height h_{max} at $t = 100$ sec as a function of the fluid consistency m with different sets of shear-thinning index and tissue viscoelastic properties (viscous-coefficient η and elasticity E).

For larger η has more impact on the bolus height h_{max} for any fluid consistency m , whereas in the case of $\eta = 0 P \cdot s^{n-1}$ (elastic tissue) the fluid's consistency m has more impact on the bolus height.

In Figure 4.11, we first note the increasing trend in the maximum height of the bolus with the pure elastic boundary ($\eta = 0 P \cdot s^{n-1}$) as the consistency increased. Figure 4.11 also shows the considerable increase in the maximum height with the viscoelastic boundary

compared to the elastic boundary. The maximum height for a viscoelastic boundary did not vary much with the fluid consistency. This indicates that the fluid consistency has less influence on the maximum height of the bolus when the viscoelasticity of the tissue is strong, as was observed for the maximum length. Alternatively it indicates that the tissue viscous-coefficient has more impact on fluids with low consistency.

Figure 4.12 shows the result for larger tissue elasticity. The height increase with increasing m was considerably small (maximum change in Δh_{max} of 1.25 %), and the impact of η was not distinguishable at any value of the fluid consistency m .

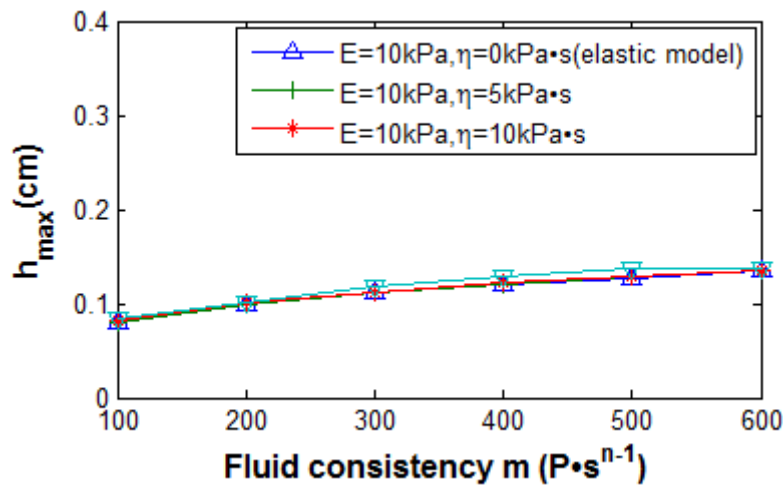


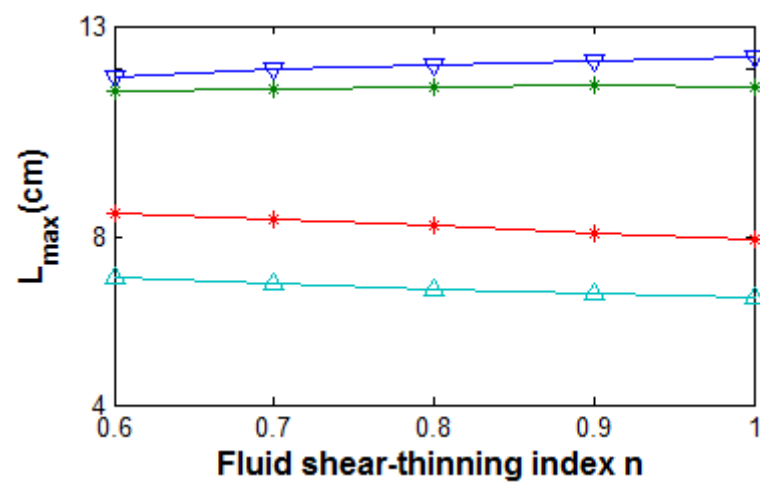
Figure 4.12: The maximum bolus height h_{max} with varying fluid consistency m for different values of tissue viscous-coefficient η and for a fixed set of the fluid shear-thinning index $n = 0.6$ tissue elasticity E .

With larger tissue elasticity E the impact of the component η on the bolus height is negligible at any value of the fluid's consistency m .

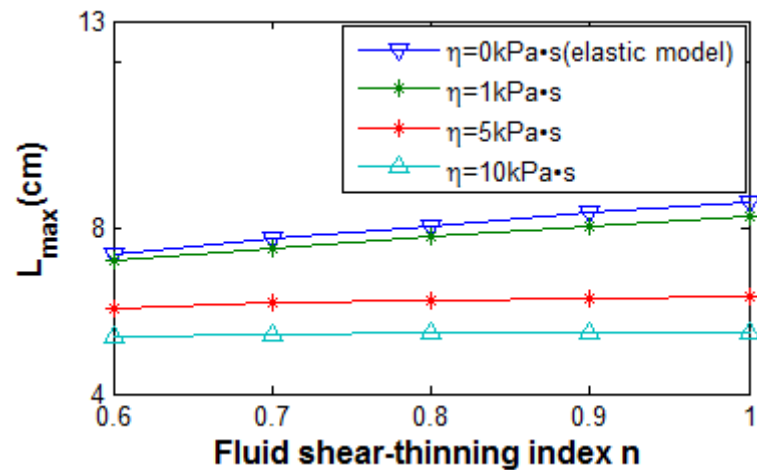
4.4.3 The influence of the tissue viscous component on the flow of the fluid with different shear-thinning indices

In addition to the fluid consistency m , the shear-thinning index n is the second parameter that describes the rheology of a power law fluid. In this section, the main results of the impact of the tissue viscous component on the flow of the fluid with different shear-thinning indices are presented and discussed. Figure 4.13 shows the change in the maximum length with increasing shear-thinning index n for different sets of the tissue viscous

component and fluid consistency. For most fluid consistencies and tissue properties the fluid spread more with increased shear-thinning index. However, the instances where the fluid consistency was low ($m = 100 \text{ P}\cdot\text{s}^{-n-1}$) and the tissue viscous component was relatively large a new trend was noticed, namely the spreading length decreased as the shear-thinning index increased. Figure 4.13 illustrates the trends observed for the cases with the tissue elasticity $E = 1 \text{ kPa}$. Similar patterns were observed for the cases with tissue elasticity $E = 10 \text{ kPa}$. (See Figure D.1 in Appendix D).



(a) $m = 100 \text{ P}\cdot\text{s}^{-n-1}$, $E = 1 \text{ kPa}$



(b) $m = 300 \text{ P}\cdot\text{s}^{-n-1}$, $E = 1 \text{ kPa}$

Figure 4.13: (a) – (b) The maximum spreading length L_{max} of the bolus with varying fluid's shear-thinning index n for different combinations of tissue elasticity E and fluid's consistency m .

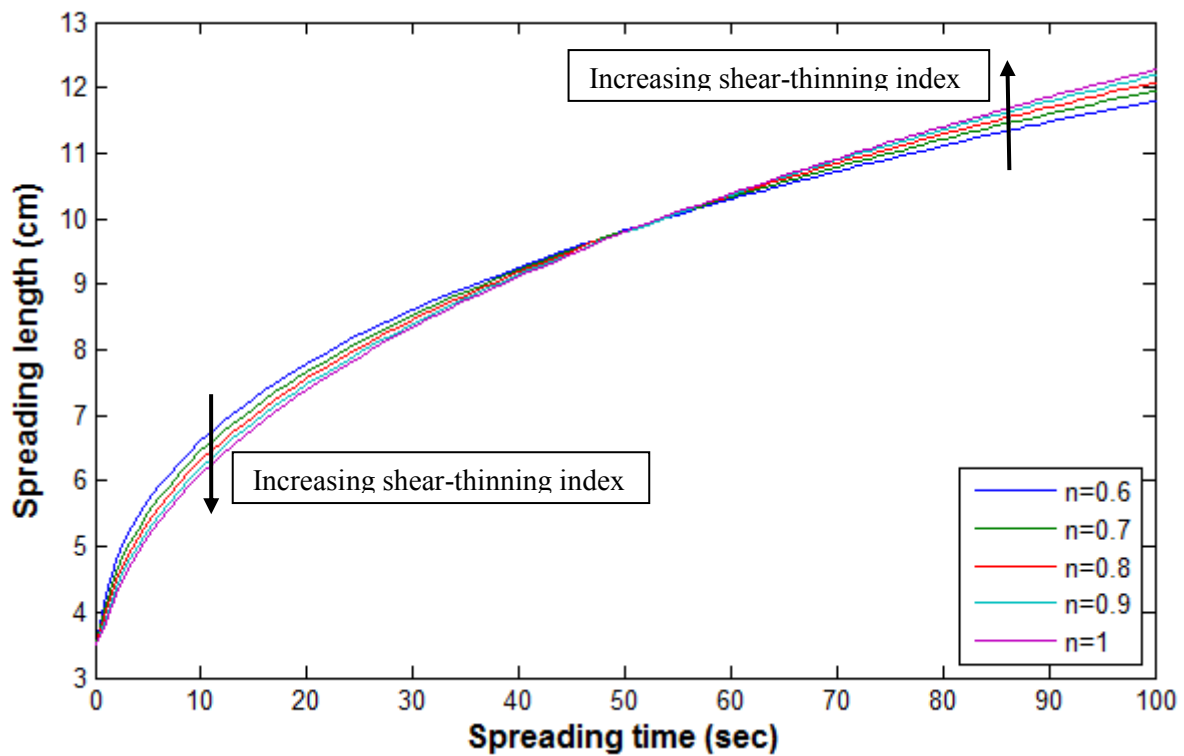
As the shear-thinning index increased, the impact of the tissue viscous-coefficient η was more noticeable. At the low consistency $m = 100 \text{ P}\cdot\text{s}^{-n-1}$, larger η values (5 and 10 $\text{kPa}\cdot\text{s}$) had a different impact on the spreading length L_{max} .

The results for the cases with the larger tissue elasticity ($E = 50\text{kPa}$) and low fluid consistency ($m = 100 \text{ P}\cdot\text{s}^{n-1}$) were not considered in this comparison since the spreading extent reached the allowable maximum length of 15 cm much earlier than the selected simulation time of 100 seconds. However, with other consistency values the maximum spreading length L_{max} (length after 100 seconds) increased as the fluid's shear thinning index increased, which was consistent with the overall trend observed with the other elasticities (see Figure D.2 in Appendix D).

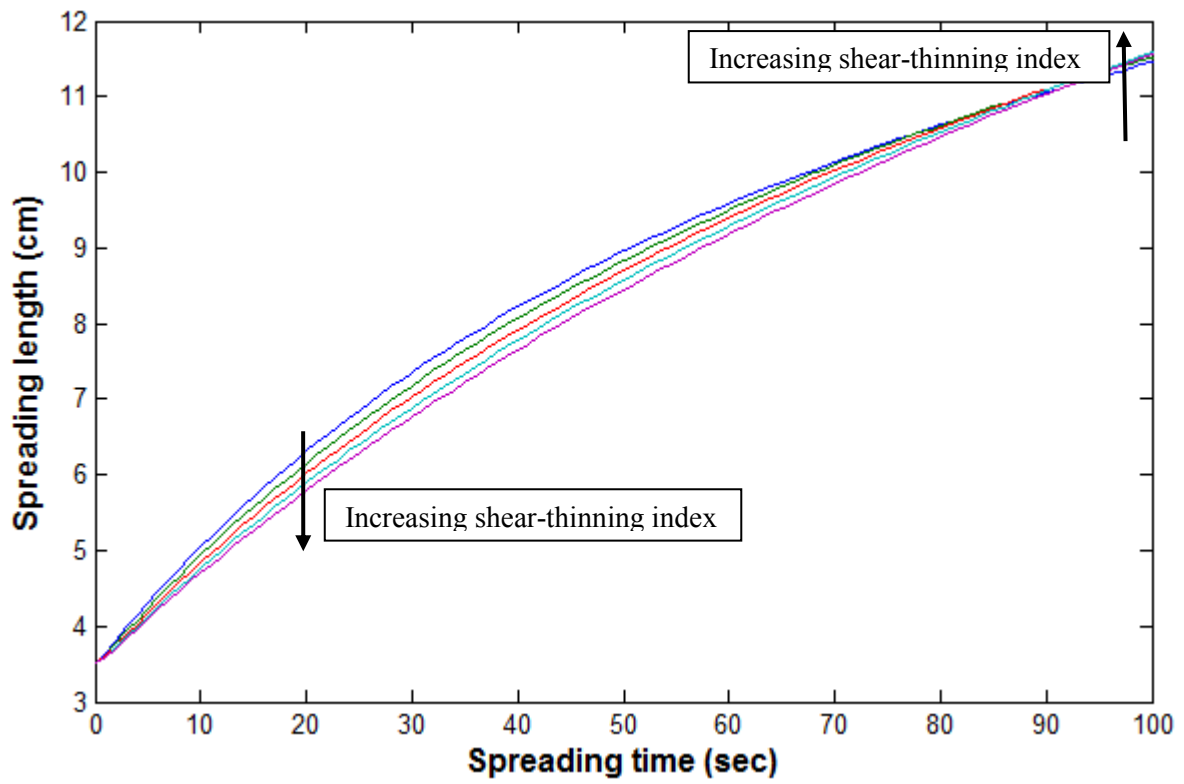
Even though there was a continuous increase in the spreading length with increasing shear-thinning index n for different tissue viscoelastic parameters and different fluid consistency m (except for the instances where $m = 100 \text{ P}\cdot\text{s}^{n-1}$ and $\eta = 5$ and $10 \text{ kPa}\cdot\text{s}$), the degree of increase was restricted by the tissue viscous component η . Figures 4.13 (b) - (c) show a continuous increase in the spreading length with increasing shear-thinning index n . The tissue viscous component η has a larger impact on the spreading length at larger values of shear-thinning index n .

Figure 4.14 (a) - (d) show the spreading of the bolus over time for different magnitudes of tissue viscous component. Figure 4.14 (a) and (b) show how the spreading rates changed during the flow for the different shear-thinning indices. At the beginning the spreading was occurring faster with lower shear-thinning indices, but towards the end of the application time, this trend changed and the spreading was faster for larger thinning indices, which explains the increase in the maximum length with increasing shear-thinning n as shown in Figure 4.13 (a) for the elastic case ($\eta = 0 \text{ P}\cdot\text{s}^{n-1}$) and for the viscoelastic case with $\eta = 1 \text{ kPa}\cdot\text{s}$. In Figure 4.13 (b), we observed a decrease in the spreading lengths with the viscoelastic boundary ($\eta = 5$ and $10 \text{ kPa}\cdot\text{s}$). This trend was due to the unchanged spreading rates of the fluid as shown in Figure 4.14 (c) and (d).

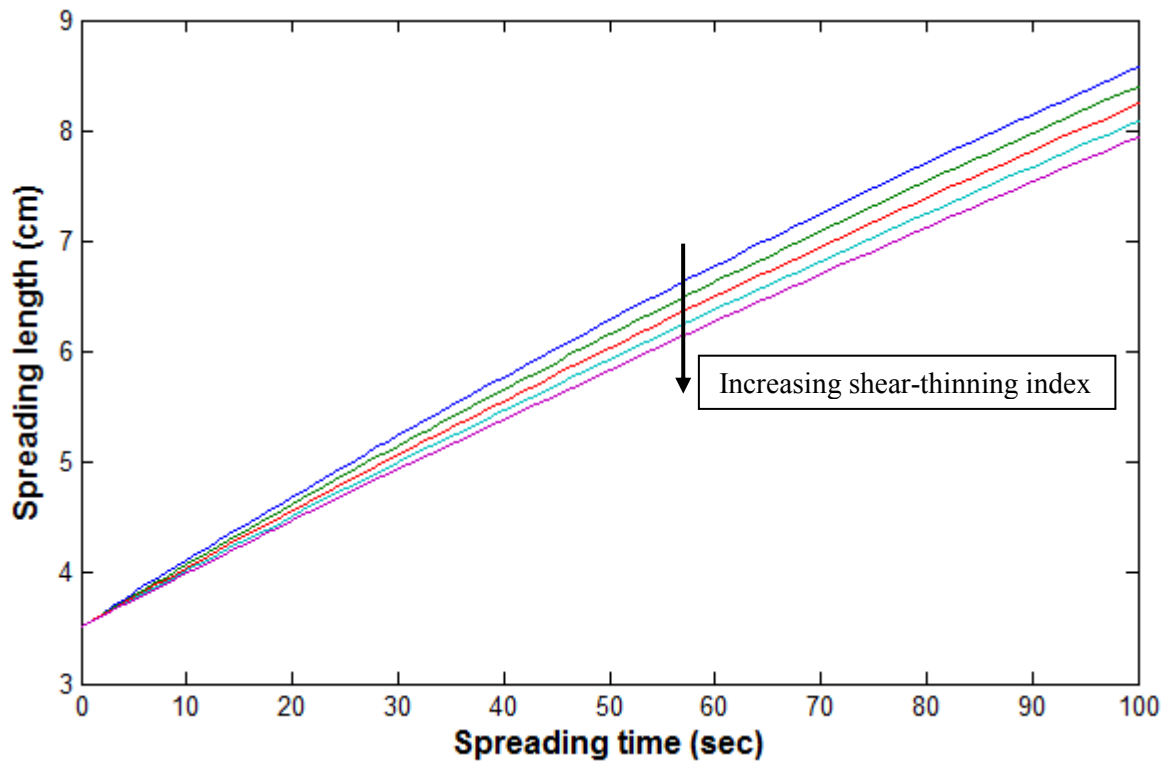
This change in the spreading rates due to different boundary properties and low fluid consistency is particularly important considering the dilution factor after the application of the gel. Once the gel is applied to the vaginal canal, it is expected to be mixed with vaginal fluids causing a change in the gel's rheological properties. Changes to the rheological properties would have a direct impact on the spreading behaviour of the gel and therefore on the coating of the targeted surfaces.



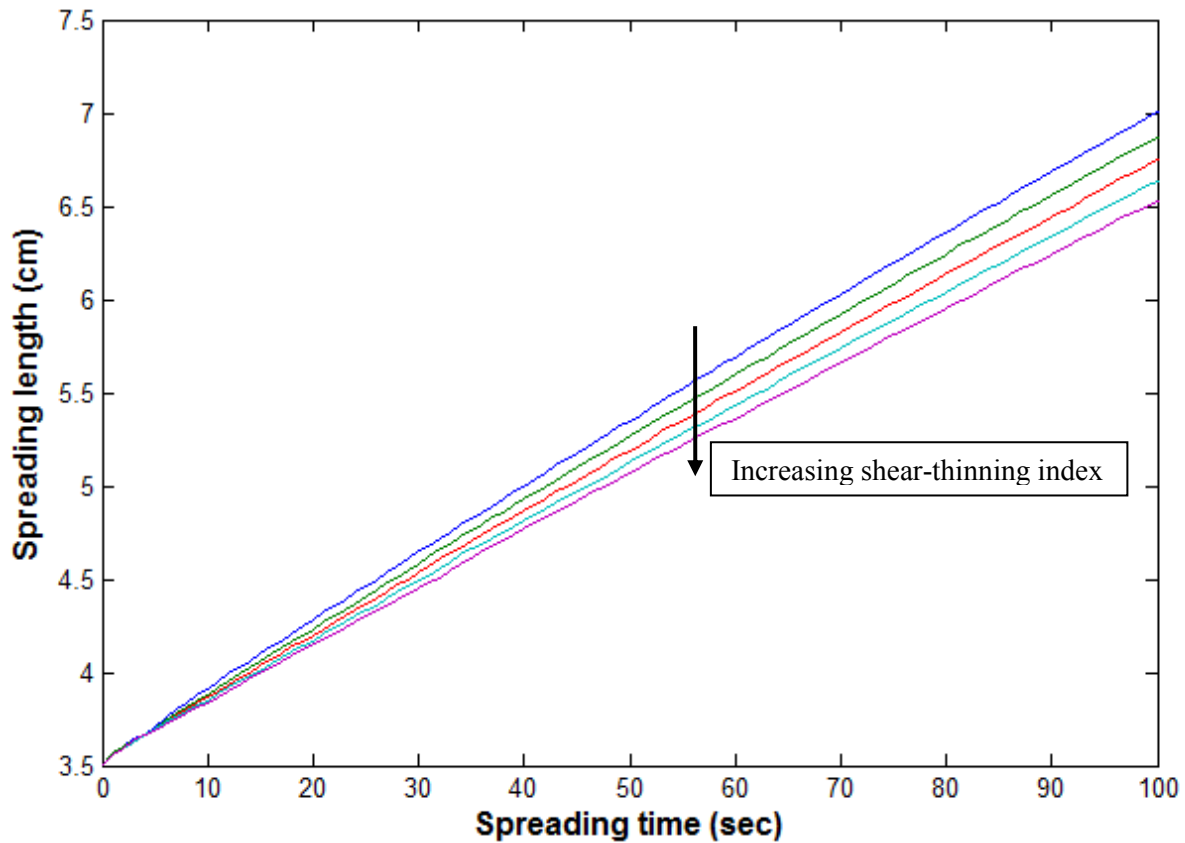
(a) $E = 1 \text{ kPa}$, $\eta = 0 \text{ kPa}\cdot\text{s}$ (elastic boundary)



(b) $E = 1 \text{ kPa}$, $\eta = 1 \text{ kPa}\cdot\text{s}$



(c) $E = 1 \text{ kPa}$, $\eta = 5 \text{ kPa}\cdot\text{s}$



(d) $E = 1 \text{ kPa}$, $\eta = 10 \text{ kPa}\cdot\text{s}$

Figure 4.14: (a) – (d) Spreading length over time of the bolus with different shear-thinning indices n and with consistency $m = 100 \text{ P}\cdot\text{s}^{n-1}$ for different combinations of tissue properties (viscous component η and elasticity E).

The change in the fluid's spreading rate depended on the shear-thinning index n and on the tissue viscous-coefficient η . With $\eta = 0$ and $1 \text{ kPa}\cdot\text{s}$, the spreading rate was higher at the beginning for lower shear-thinning indices n but by the end of the flow this trend changed and the spreading was faster for larger shear-thinning indices. Whereas, for $\eta = 5$ and $10 \text{ kPa}\cdot\text{s}$ the spreading rate was higher for lower shear-thinning indices n throughout the flow duration.

As indicated in previous sections, the maximum bolus height (i.e bolus thickness) was larger when the length was smaller. The change in the maximum height was more pronounced and limited to the cases where the magnitude of the tissue viscous-coefficient was larger than the magnitude the elasticity. Figure 4.15 shows the change in the maximum height of the bolus with increasing shear-thinning index n for different combinations of fluid consistency and tissue viscous component. With the viscoelastic boundary, the maximum

height increased as n increased for different fluid consistencies. Whereas, with the elastic boundary the maximum height decreased as the shear-thinning index n increased (see Figure 4.15 (b) - (c)). The change in the trend for the maximum height caused by the low consistency m with the elastic boundary is consistent with the spreading rate patterns shown in Figure 4.14 (a). Figure 4.14 (a) showed that at the end of the application time larger shear-thinning indices caused a less spreading length and consequently the maximum height of the bolus increased. Overall, the tissue viscous component has more impact on the maximum height of the bolus at larger shear-thinning index.

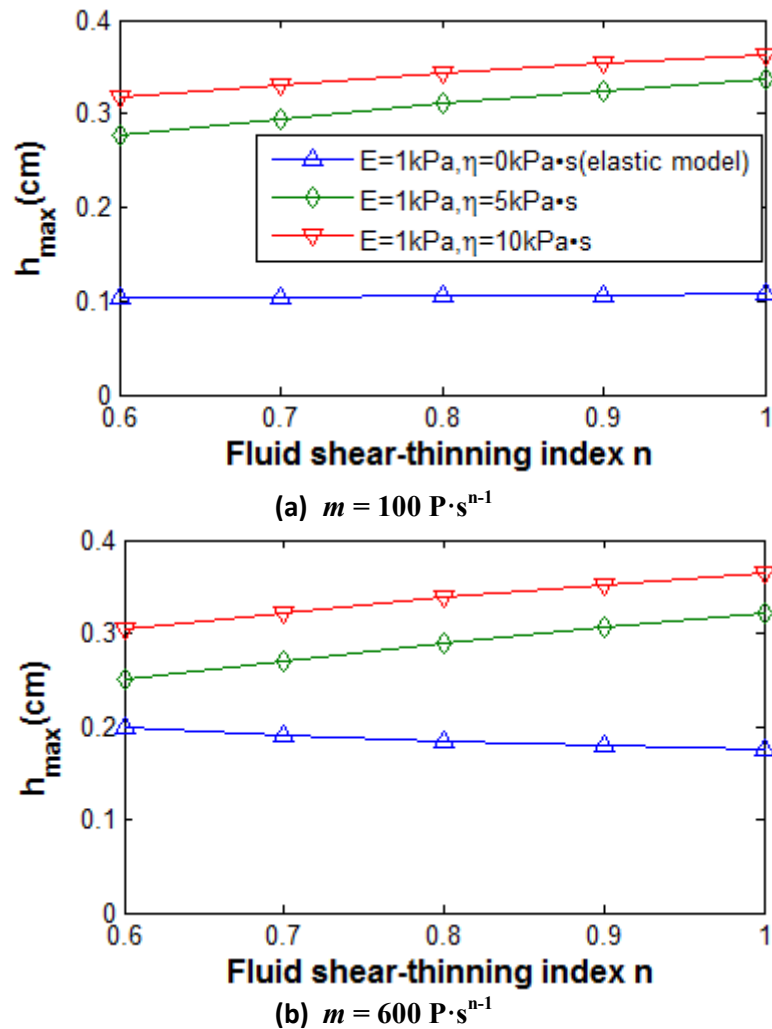


Figure 4.15: (a) – (b) the maximum bolus height h_{max} at $t = 100$ sec as a function of the fluid's shear-thinning index n for different consistency m and tissue viscoelastic properties (viscous-coefficient η and elasticity E).

The parameter η has more impact on the bolus height at larger n . With η larger values increased as the shear-thinning index n increased.

For the cases where the magnitude of the tissue's elasticity was larger than the magnitude of the tissue viscous component, the change in the maximum height of the bolus was negligible (see Figure D.3 in Appendix D).

4.4.4 Non-dimensional analysis

Non-dimensional parametric studies generally help reduce the amount of the numerical simulation required for analysis by reducing the number of variables. Dimensionless studies allow the assessment of the impact of the parameters relative to each other. For instance, the dimensionless variable $Z \left(\frac{\eta}{E} \left(\frac{EH}{Tm} \right)^{\frac{1}{n}} \right)$ can be considered to evaluate the interaction between the tissue viscous-coefficient and elasticity for a given fluid consistency m and shear-thinning index n .

For the design and optimization of microbicidal gels, the interpretation of the non-dimensional results would be convoluted. This is due to the fact that the non-dimensional grouping $Z \left(\frac{\eta}{E} \left(\frac{EH}{Tm} \right)^{\frac{1}{n}} \right)$ and $W \left(\frac{T\rho g x}{E} \right)$, as well as the dimensionless time $\bar{t} \left(t \left(\frac{EH}{Tm} \right)^{1/n} \right)$ have several common variables. The shared parameters would make a dimensionless coupled parametric study like the one considered for the dimensional analysis (see section 3.3.3) complicated to interpret.

The difficulty with the non-dimensional grouping having shared variables remained even after considering a different non-Newtonian fluid constitutive model. We developed a numerical model (in the dimensional and non-dimensional forms) of the flow with the Ellis constitutive model for a non-Newtonian fluid (see appendix E). With the Ellis model the dimensionless parameters $= \frac{\eta H}{T\eta_0}$, $W = \frac{T\rho g x}{E}$, $Y = \frac{EH}{T\tau_{1/2}}$, and the dimensionless time $\bar{t} = t \left(\frac{EH}{T\eta_0} \right)$ also share common variables.

Chapter 5: Conclusions, limitations, and future work

The aim of this study was to evaluate the impact of viscoelastic boundaries and pure elastic boundaries on the spreading behaviour of different formulations of a microbicidal gel. The scope of this study focused on the impact of the vaginal tissue viscous component on the flow of a gel with various rheological properties. Based on the numerical results, we found that there is a difference between linear elastic and linear viscoelastic tissue impact on the flow of a gel. The amount of difference between elastic and viscoelastic tissue varied with the change in the relative magnitudes of the tissue elasticity and of the viscous-coefficient. There was a more pronounced difference between elastic and viscoelastic tissue at low tissue elasticity and high tissue viscous-coefficient. The viscous-coefficient has a greater impact on the spreading extent for a gel with a high shear-thinning index and a low consistency. It is anticipated that after the application of the gel into the vaginal canal, the gel will dilute as it mixes with the vaginal fluids. The dilution of the gel would decrease its consistency and increase its shear-thinning index and subsequently increase the impact of the tissue viscous component on the diluted gel.

This work was an initial attempt at incorporating the viscoelastic characteristics of the vaginal tissue in a numerical model to simulate the flow of a microbicidal gel between viscoelastic boundaries. The findings of this study expand the framework of microbicidal gels development.

One of this study limitations is that it was limited to a 2D numerical model (1D spreading), which means the spreading of the fluid was studied in in the axial direction only. In a real application, a gel will spread in both the axial, as well as in the lateral direction. Expanding the current model to 3D model would be of advantageous, as since the 3D model

accounts for the spreading in both directions and would provide more details on the spreading behaviour of the gel in the two different directions. However, it is difficult to define the 3D flow geometry, as the vaginal canal is asymmetric and doesn't conform to conventional shapes. The spreading behaviour of the gel in the lateral and axial directions would likely be different due to the asymmetry of the vaginal canal. The flow in the two directions might be affected by changes in the tissue viscoelasticity along the axial and lateral directions. Additionally, 3D numerical simulations would substantially increase the computational time. For the strain of the tissue, we considered the deformation in the normal direction only. In a real situation, the tissue might stretch in the circumferential as well as in the radial direction. For future studies, a better representation and estimation of the strain would help in understanding the response of the tissue.

In this study a simple linear viscoelastic model was used to represent the viscoelastic properties of the vaginal tissue. With the simple model we were able to represent the pressure term of the numerical flow model explicitly as the normal stress in the tissue. Complex and non-linear viscoelastic models would be more representative of the tissue response. However, with these complex and non-linear models, it is not always possible or simple to get an explicit equation for the stress. Future studies with such models would require fluid-structure interaction (FSI) methods to improve the understanding of how the viscoelastic tissue responds to the fluid and how this response influences the flow behaviour.

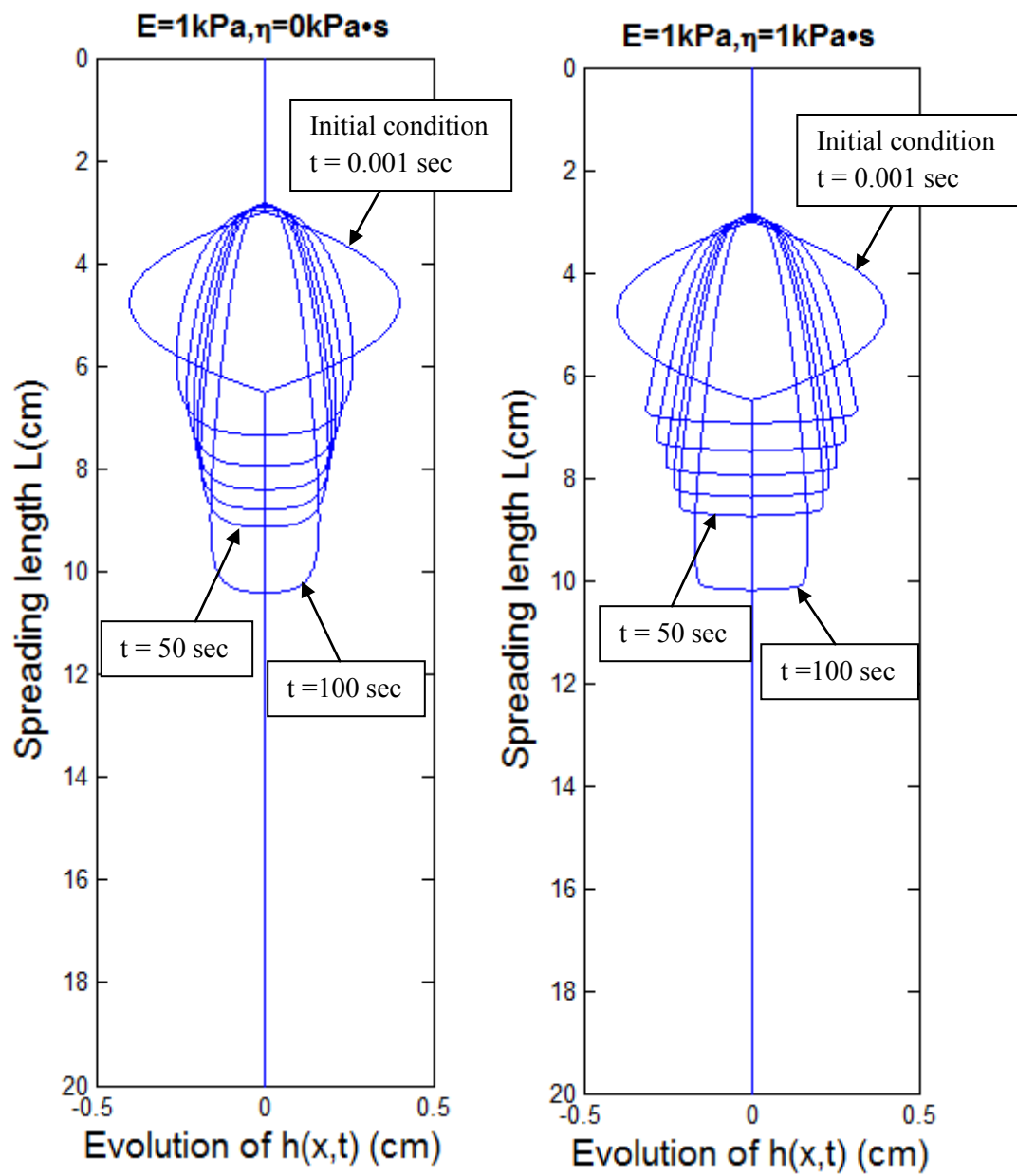
The theoretical model was developed based on the constitutive equation of the power-law model. Developing additional numerical models with other constitutive equations for non-Newtonian fluids would increase the understanding of the tissue viscoelasticity impact on the spreading of the gel with different rheological properties. Considering a constitutive model that incorporates the fluid viscoelasticity would be especially beneficial, as it would compare the relative effects of the viscoelasticity of the fluid and of the tissue. Due to the

complexity of investigating the relative effects of the tissue and the fluid viscoelasticities, a fluid-structure interaction model would increase understanding of the interaction between the fluid and the tissue.

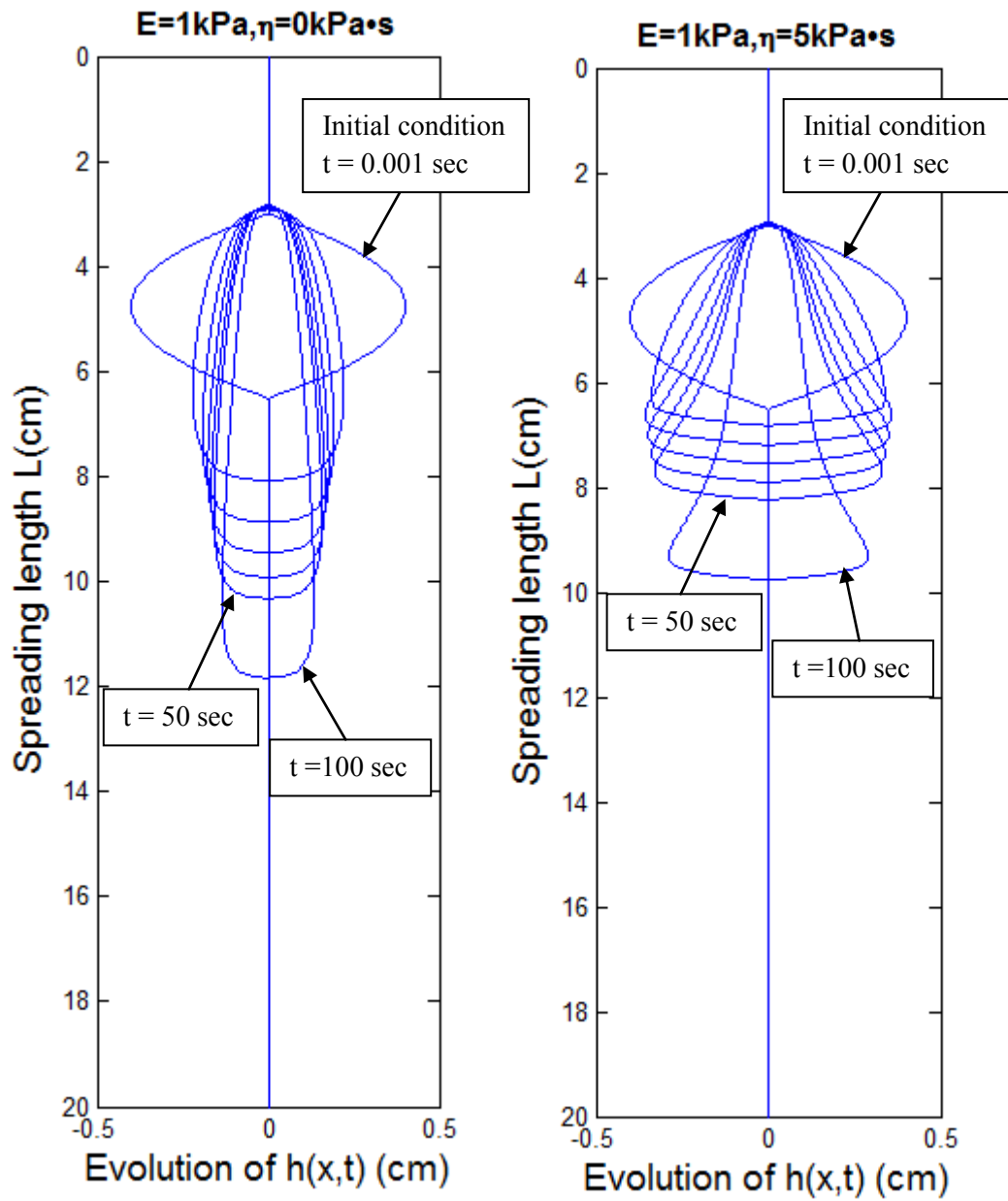
This study clearly shows the importance and significance of measuring the biomechanical properties of the vaginal tissue *in vivo*. The characterization of the tissue viscoelastic properties would not only help in developing more accurate and more relevant numerical models, but also play a major role in validating the numerical studies.

Appendices

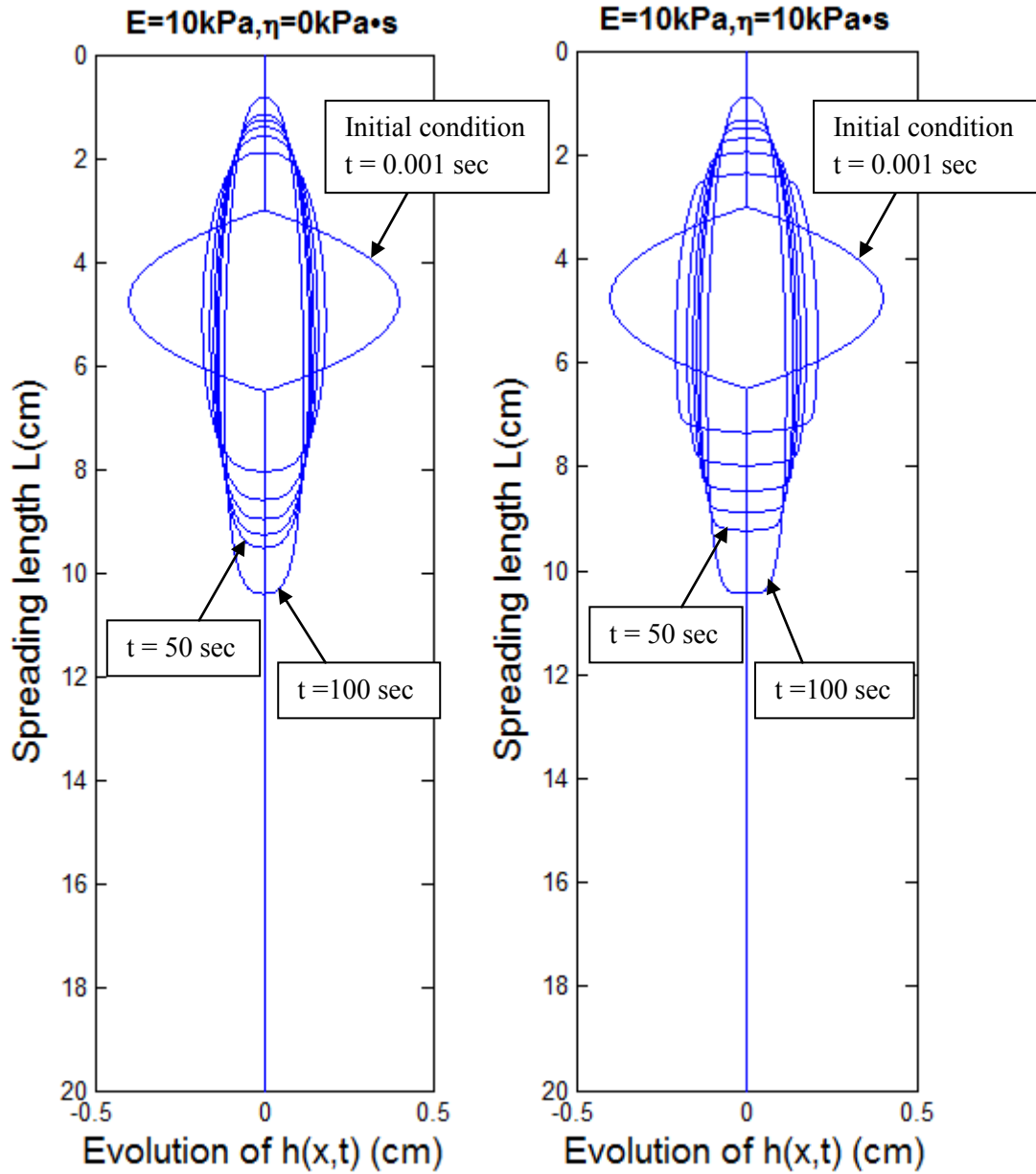
Appendix A. Examples of spreading profiles with different tissue and fluid properties



(a) $n = 0.9, m = 400 \text{ P}\cdot\text{s}^{n-1}$



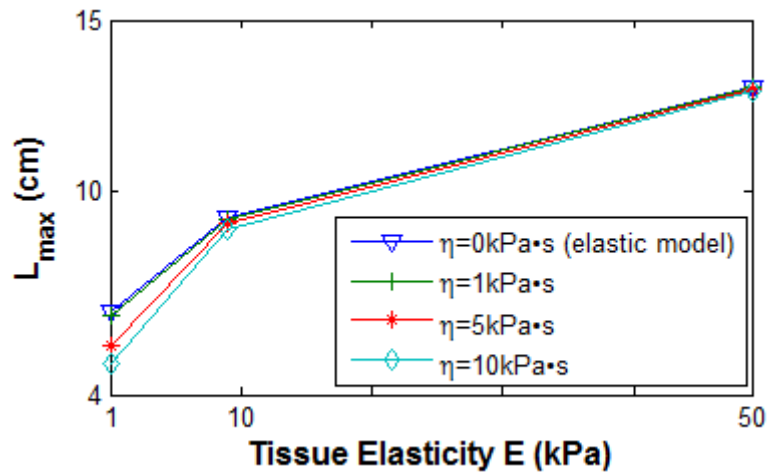
(b) $n = 0.7, m = 200 \text{ P}\cdot\text{s}^{n-1}$



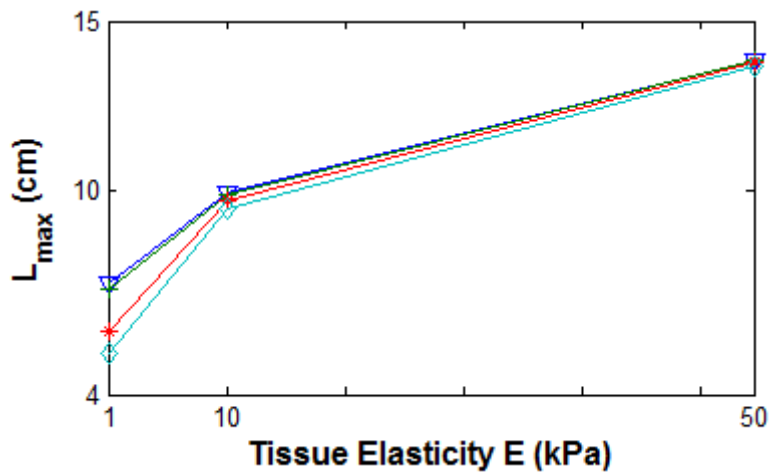
(c) $n = 0.9, m = 500 \text{ P}\cdot\text{s}^{n-1}$

Figure A.1: Flow profiles with different rheological properties of the fluid and different boundary elastic and viscous component illustrating the effect of the elastic model and the viscoelastic model of the tissue.

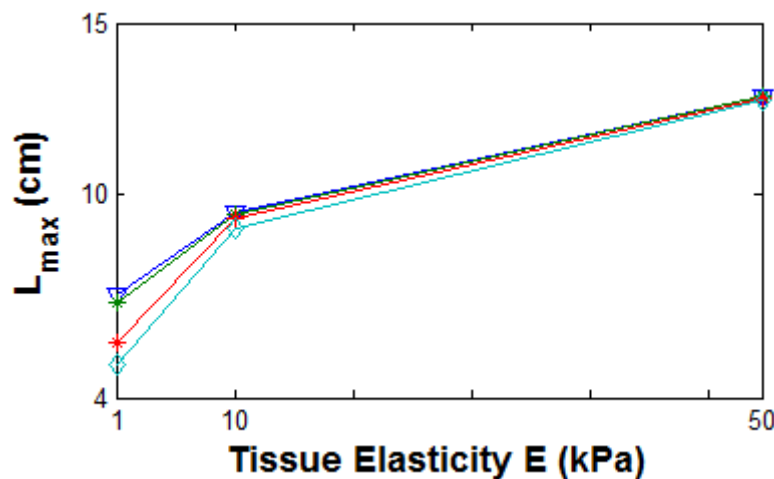
Appendix B. Examples of the change in the maximum length with changing boundary properties for various fluid properties



(a) $n = 0.7, m = 500 \text{ P}\cdot\text{s}^{n-1}$



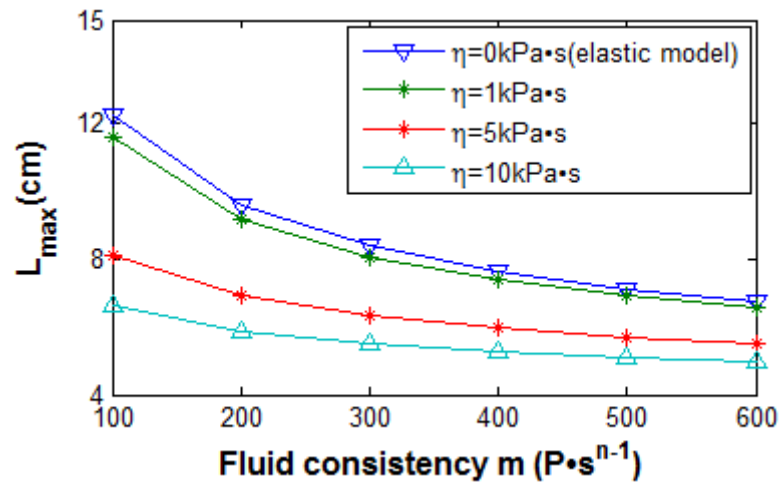
(b) $n = 0.8, m = 400 \text{ P}\cdot\text{s}^{n-1}$



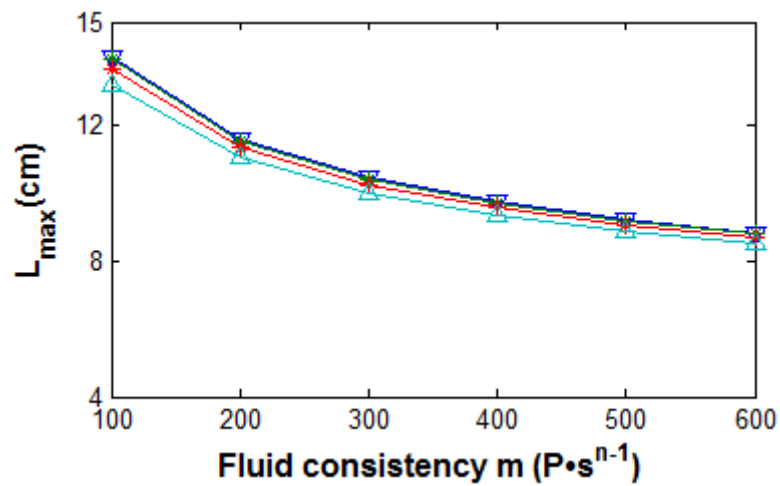
(c) $n = 1, m = 600 \text{ P}\cdot\text{s}^{n-1}$

Figure B.1: Maximum length of the bolus as function of boundary elasticity for various values of tissue viscous-coefficient.

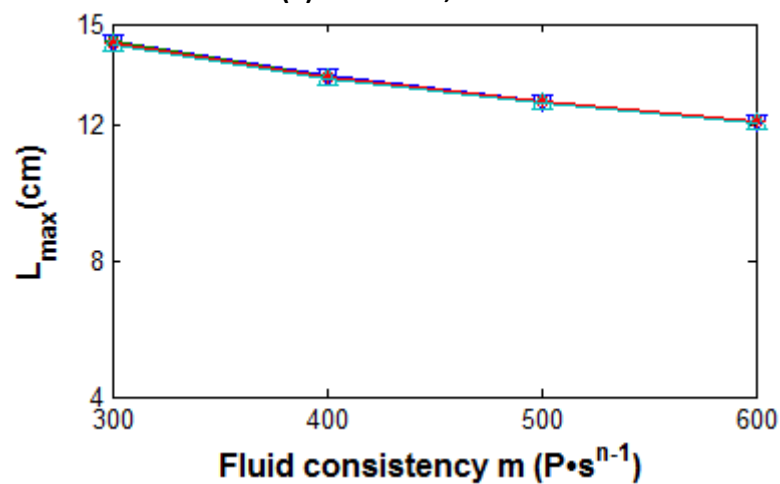
Appendix C. The influence of the tissue viscous component on the fluid with different consistencies



(a) $E = 1 \text{ kPa}, n = 0.9$



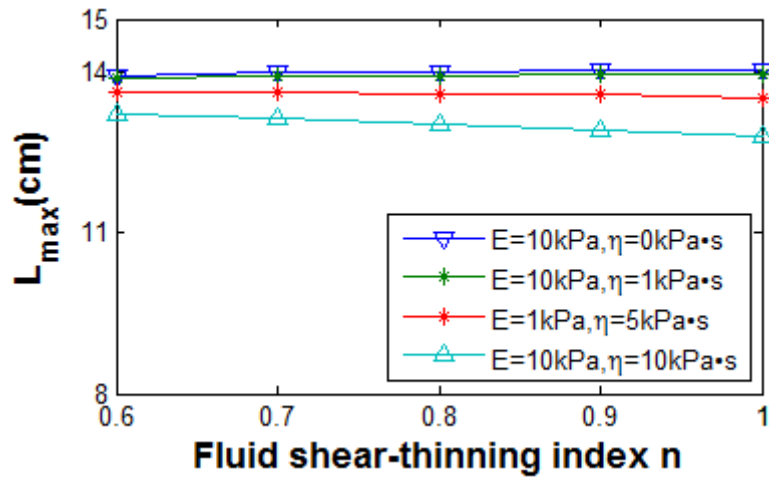
(b) $E = 10 \text{ kPa}, n = 0.7$



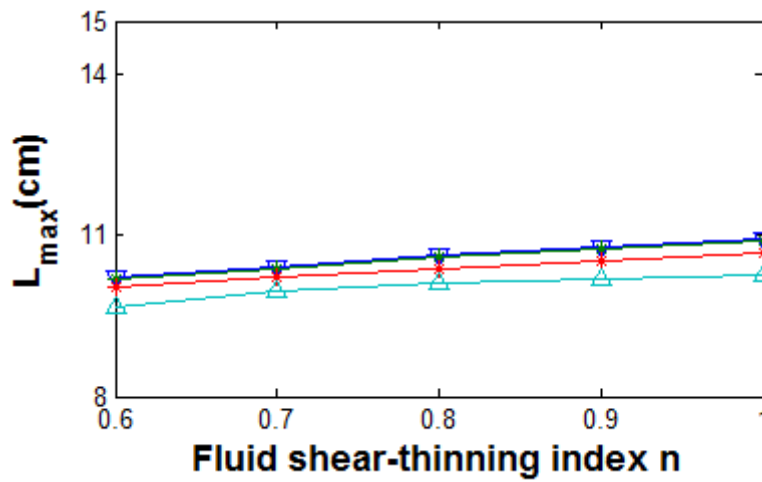
(c) $E = 50 \text{ kPa}, n = 0.5$

Figure C.1: Maximum length of the bolus with various consistencies for different sets of tissue properties and shear-thinning index n .

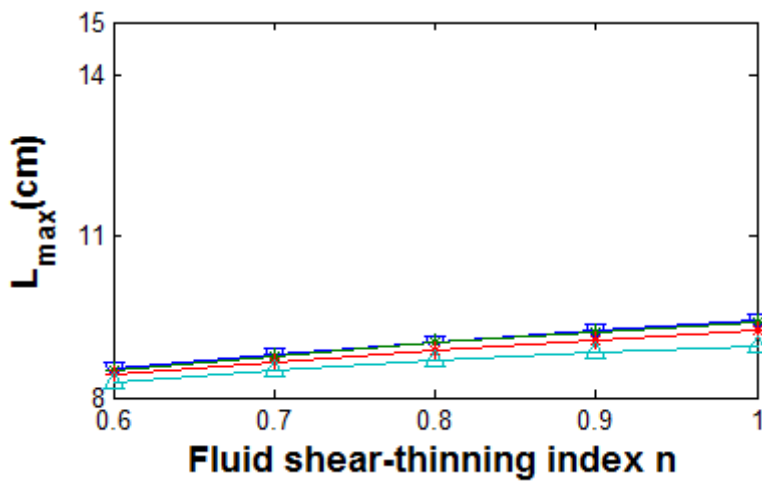
Appendix D. The influence of the tissue viscous component on the fluid with different shear-thinning indices



(a) $m = 100 \text{ P}\cdot\text{s}^{n-1}$

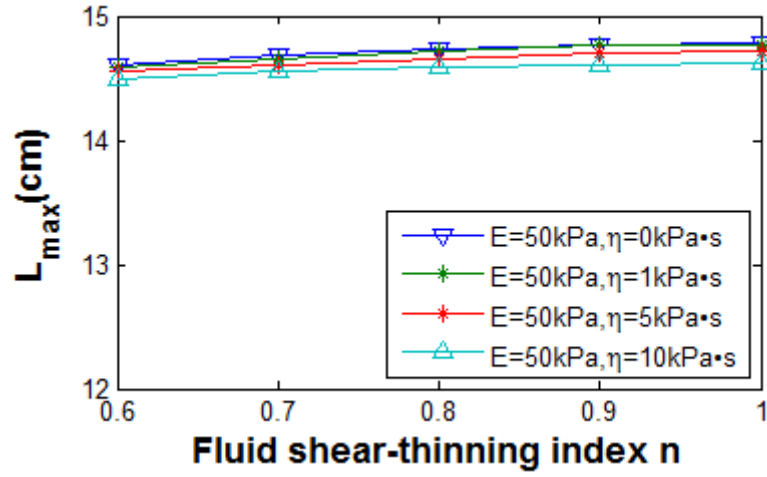


(b) $m = 300 \text{ P}\cdot\text{s}^{n-1}$

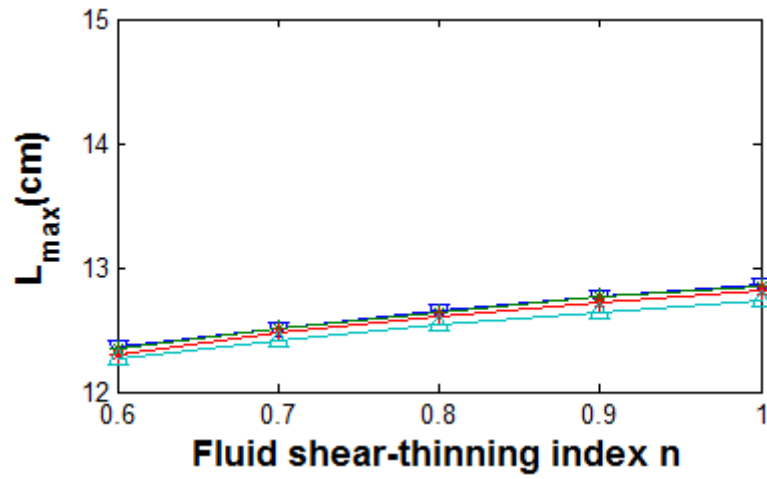


(c) $m = 600 \text{ P}\cdot\text{s}^{n-1}$

Figure D.1: The maximum spreading length as function of shear-thinning index n for various boundary properties and fluid consistency.

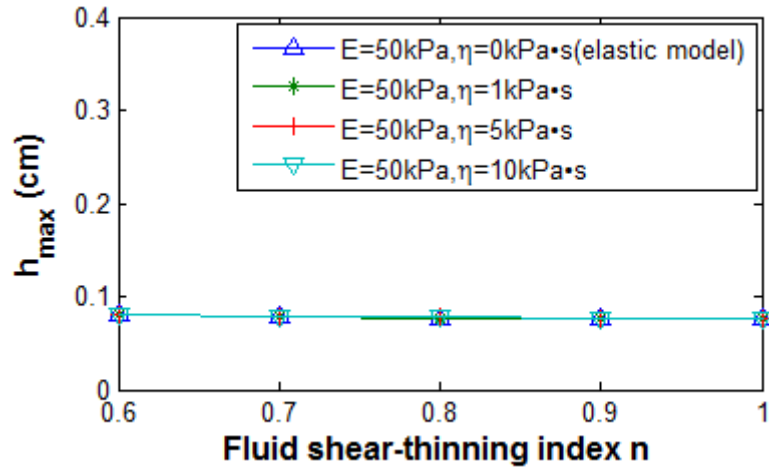


(a) $m = 300 \text{ P}\cdot\text{s}^{-1}$

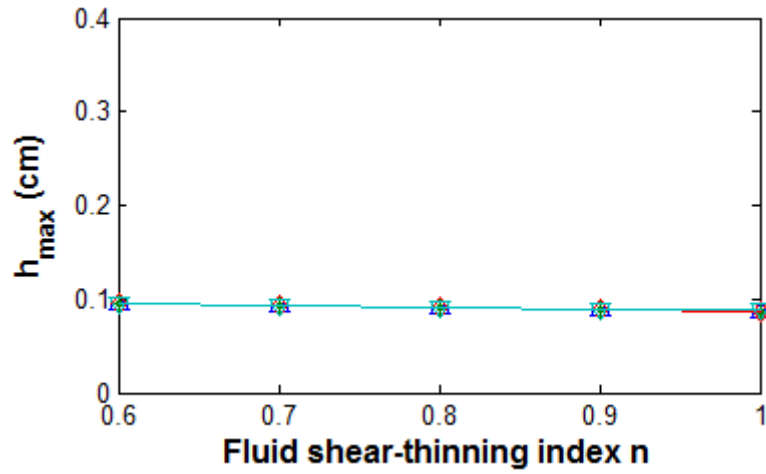


(b) $m = 600 \text{ P}\cdot\text{s}^{-1}$

Figure D.2: The maximum spreading length as function of shear-thinning index n . The small change in spreading lengths illustrates the low impact of the tissue viscous component with large tissue elasticity.



(a) $m = 300 \text{ P}\cdot\text{s}^{n-1}$



(b) $m = 600 \text{ P}\cdot\text{s}^{n-1}$

Figure D.3: The maximum height the bolus with various shear-thinning index n . The negligible change in bolus height illustrates the low impact of the tissue viscous component with large tissue elasticity.

Appendix E. Derivation of the evolution equation (in the dimensional and non-dimensional forms) with the Ellis constitutive model

For 1D spreading the constitutive equation of the Ellis model is given by:

$$\eta_{app} = \frac{\eta_0}{\left(1 + \left|\frac{\tau_{zx}}{\tau_{1/2}}\right|^{\alpha-1}\right)}$$

Where η_{app} is the fluid apparent viscosity, η_0 is the zero shear stress viscosity and $\tau_{1/2}$ is the shear stress when the viscosity has decreased by a factor of one-half. α is the fluid's shear-thinning number. The shear stress with the Ellis model is given by:

$$\tau_{zx} = \eta_{app} \frac{\partial u}{\partial z}$$

An expression for velocity was obtained by substituting the Ellis constitutive model into the expression for shear stress $\tau_{zx}(x, z, t)$ from section 3.2.3 and integrating with respect to z . The no-slip boundary condition was used to determine the constant of integration. The velocity equation of the flow was determined as:

$$u(x, z, t) = \frac{1}{\eta_0} \left(\left(\frac{E}{T} \frac{\partial h}{\partial x} + \frac{\eta}{T} \frac{\partial^2 h}{\partial x \partial t} - \rho g_x \right) \frac{z^2 - h^2}{2} + \frac{z^{\alpha+1} - h^{\alpha+1}}{\alpha + 1} \left(\frac{E}{T} \frac{\partial h}{\partial x} + \frac{\eta}{T} \frac{\partial^2 h}{\partial x \partial t} - \rho g_x \right) \left| \frac{\left(\left(\frac{E}{T} \frac{\partial h}{\partial x} + \frac{\eta}{T} \frac{\partial^2 h}{\partial x \partial t} - \rho g_x \right) \right)^{\alpha-1}}{\tau_{1/2}} \right| \right)$$

As in section 3.2.4, the velocity was used to determine the flow rate per unit width $q(x, t)$:

$$q(x, t) = \frac{-1}{\eta_0} \left(\left(\frac{E}{T} \frac{\partial h}{\partial x} + \frac{\eta}{T} \frac{\partial^2 h}{\partial x \partial t} - \rho g_x \right) \left(\frac{h^3}{3} \right) \right. \\ \left. + \frac{h^{\alpha+2}}{(\alpha+2)} \left(\frac{E}{T} \frac{\partial h}{\partial x} + \frac{\eta}{T} \frac{\partial^2 h}{\partial x \partial t} - \rho g_x \right) \left| \frac{\left(\frac{E}{T} \frac{\partial h}{\partial x} + \frac{\eta}{T} \frac{\partial^2 h}{\partial x \partial t} - \rho g_x \right)}{\tau_{1/2}} \right|^{\alpha-1} \right)$$

Using the law of conservation of mass as in section 3.2.5, the evolution equation for $h(x, t)$ with the Ellis model was obtained:

$$\frac{\partial h(x, t)}{\partial t} - \frac{1}{\eta_0} \frac{\partial}{\partial x} \left(\left(\frac{E}{T} \frac{\partial h}{\partial x} + \frac{\eta}{T} \frac{\partial^2 h}{\partial x \partial t} - \rho g_x \right) \left(\frac{h^3}{3} \right) \right. \\ \left. + \frac{h^{\alpha+2}}{(\alpha+2)} \left(\frac{E}{T} \frac{\partial h}{\partial x} + \frac{\eta}{T} \frac{\partial^2 h}{\partial x \partial t} - \rho g_x \right) \left| \frac{\left(\frac{E}{T} \frac{\partial h}{\partial x} + \frac{\eta}{T} \frac{\partial^2 h}{\partial x \partial t} - \rho g_x \right)}{\tau_{1/2}} \right|^{\alpha-1} \right) = 0$$

The evolution equation above can be written in a non-dimensional form using the following dimensionless scaling ratios:

$$\bar{h} = \frac{h}{H}$$

$$\bar{x} = \frac{x}{H}$$

$$\bar{t} = t \left(\frac{EH}{T\eta_0} \right)$$

where H is a characteristic dimension of the gel bolus, such as its initial maximum height.

The non-dimensional evolution equation is given by:

$$\frac{\partial \bar{h}(x, t)}{\partial \bar{t}} - \frac{\partial}{\partial \bar{x}} \left(\left(\frac{\partial \bar{h}}{\partial \bar{x}} + Z \frac{\partial^2 \bar{h}}{\partial \bar{x} \partial \bar{t}} - W \right) \left(\frac{\bar{h}^3}{3} \right) \right. \\ \left. + \frac{\bar{h}^{\alpha+2}}{(\alpha+2)} \left(\frac{\partial \bar{h}}{\partial \bar{x}} + Z \frac{\partial^2 \bar{h}}{\partial \bar{x} \partial \bar{t}} - W \right) \left| Y \left(\frac{\partial \bar{h}}{\partial \bar{x}} + Z \frac{\partial^2 \bar{h}}{\partial \bar{x} \partial \bar{t}} - W \right) \right|^{\alpha-1} \right) = 0$$

where $Z = \frac{\eta H}{T\eta_0}$, $W = \frac{T\rho g_x}{E}$, and $Y = \frac{EH}{T\tau_{1/2}}$ are non-dimensional variables

References

1. McConville, C. and D. Friend, *Development and characterisation of a self-microemulsifying drug delivery systems (SMEDDSs) for the vaginal administration of the antiretroviral UC-781*. Eur J Pharm Biopharm, 2012.
2. Abdulai M. A., B.F., Adjei G., Afari-Asiedu S., Adjei K., Tawiah C., Newton S., *An assessment of the likely acceptability of vaginal microbicides for HIV prevention among women in rural Ghana*. BMC Womens Health, 2012. **12**: p. 40.
3. UNAIDS, J.U.N.P.o.H.A. *Global Report: UNAIDS report on the global AIDS epidemic 2012*. 2012 [cited 2013; Available from: http://www.unaids.org/en/resources/campaigns/20121120_globalreport2012/globalreport/
4. Obiero, J., et al., *Vaginal microbicides for reducing the risk of sexual acquisition of HIV infection in women: systematic review and meta-analysis*. BMC Infect Dis, 2012. **12**: p. 289.
5. Buckheit, R.W., Jr., et al., *Development of topical microbicides to prevent the sexual transmission of HIV*. Antiviral Res, 2010. **85**(1): p. 142-58.
6. Abdool Karim, Q., H. Humphries, and Z. Stein, *Empowering women in human immunodeficiency virus prevention*. Best Pract Res Clin Obstet Gynaecol, 2012. **26**(4): p. 487-93.
7. Vallely, A., et al., *Intravaginal practices and microbicide acceptability in Papua New Guinea: implications for HIV prevention in a moderate-prevalence setting*. BMC Res Notes, 2012. **5**(1): p. 613.
8. Gupta, N.a., Gupta S.K., *Microbicides: a new hope for HIV prevention*. Indian J Med Res, 2011. **134**: p. 939-949.
9. Choudhury A., D.S., Kar M., *A Review on Novelty and Potentiality of Vaginal Drug Delivery*. International Journal of PharmTech Research, 2011. **3**(2): p. 1033-1044.
10. Fetherston, S.M., et al., *A silicone elastomer vaginal ring for HIV prevention containing two microbicides with different mechanisms of action*. Eur J Pharm Sci, 2012. **48**(3): p. 406-415.
11. Abramowitch, S.D., et al., *Tissue mechanics, animal models, and pelvic organ prolapse: a review*. Eur J Obstet Gynecol Reprod Biol, 2009. **144 Suppl 1**: p. S146-58.
12. Malcolm, K., et al., *Influence of silicone elastomer solubility and diffusivity on the in vitro release of drugs from intravaginal rings*. Journal of Controlled Release, 2003. **90**(2): p. 217-225.
13. Pliszczak, D., et al., *Mucoadhesion evaluation of polysaccharide gels for vaginal application by using rheological and indentation measurements*. Colloids Surf B Biointerfaces, 2012. **92**: p. 168-74.
14. Valenta, C., *The use of mucoadhesive polymers in vaginal delivery*. Adv Drug Deliv Rev, 2005. **57**(11): p. 1692-712.
15. Szeri, A.J., et al., *A model of transluminal flow of an anti-HIV microbicide vehicle: Combined elastic squeezing and gravitational sliding*. Phys Fluids (1994), 2008. **20**(8): p. 83101.
16. Tasoglu, S., et al., *The consequences of yield stress on deployment of a non-Newtonian anti-HIV microbicide gel*. J Nonnewton Fluid Mech, 2011. **166**(19-20): p. 1116-1122.
17. Tasoglu, S., et al., *The effects of inhomogeneous boundary dilution on the coating flow of an anti-HIV microbicide vehicle*. Phys Fluids (1994), 2011. **23**(9): p. 93101-931019.
18. Tasoglu, S., D.F. Katz, and A.J. Szeri, *Transient spreading and swelling behavior of a gel deploying an anti-HIV topical microbicide*. Journal of Non-Newtonian Fluid Mechanics, 2012. **187-188**: p. 36-42.
19. Karri, S., *2D Thin-Film Flow of a Non-Newtonian Fluid Between Elastic Boundaries* Department of Mechanical Engineering. 2011, The University of Kansas.

20. Pena, E., et al., *Experimental study and constitutive modeling of the viscoelastic mechanical properties of the human prolapsed vaginal tissue*. Biomech Model Mechanobiol, 2010. **9**(1): p. 35-44.
21. Barnhart, K.T., et al., *Baseline dimensions of the human vagina*. Hum Reprod, 2006. **21**(6): p. 1618-22.
22. Rohan, L.C. and A.B. Sassi, *Vaginal drug delivery systems for HIV prevention*. AAPS J, 2009. **11**(1): p. 78-87.
23. Panayi, D.C., et al., *Ultrasound measurement of vaginal wall thickness: a novel and reliable technique*. Int Urogynecol J, 2010. **21**(10): p. 1265-70.
24. Hsu, Y., et al., *Vaginal thickness, cross-sectional area, and perimeter in women with and those without prolapse*. Obstet Gynecol, 2005. **105**(5 Pt 1): p. 1012-7.
25. Aritan, S., S.O. Oyadiji, and R.M. Bartlett, *A mechanical model representation of the in vivo creep behaviour of muscular bulk tissue*. J Biomech, 2008. **41**(12): p. 2760-5.
26. Kieweg, S.L. and D.F. Katz, *Squeezing flows of vaginal gel formulations relevant to microbicide drug delivery*. J Biomech Eng, 2006. **128**(4): p. 540-53.
27. Epstein, L.B., C.A. Graham, and M.H. Heit, *Impact of sacral colpopexy on in vivo vaginal biomechanical properties*. Am J Obstet Gynecol, 2008. **199**(6): p. 664 e1-6.
28. YC, F., *Biomechanics: Mechanical Properties of Living Tissues*. 2nd ed. 1993, New York: Springer-Verlag.
29. Masao Tanaka, s.W., Masanori Nakamura, *Computational Biomechanics*. Vol. 3rd. 2012, Tokyo: Springer.
30. Kiss, M.Z., T. Varghese, and T.J. Hall, *Viscoelastic characterization of in vitro canine tissue*. Physics in Medicine and Biology, 2004. **49**(18): p. 4207-4218.
31. Boyer G., Z.H., Le Bot A., Laquieze L., *In vivo characterization of viscoelastic properties of human skin using dynamic micro-indentation*. Proceedings of the 29th Annual International Conference of the IEEE EMBS, 2007.
32. Haslach, H.W., Jr., *Nonlinear viscoelastic, thermodynamically consistent, models for biological soft tissue*. Biomech Model Mechanobiol, 2005. **3**(3): p. 172-89.
33. Leclerc, G.E., et al., *Characterization of a hyper-viscoelastic phantom mimicking biological soft tissue using an abdominal pneumatic driver with magnetic resonance elastography (MRE)*. J Biomech, 2012. **45**(6): p. 952-7.
34. Čanić, S., et al., *Modeling Viscoelastic Behavior of Arterial Walls and Their Interaction with Pulsatile Blood Flow*. SIAM Journal on Applied Mathematics, 2006. **67**(1): p. 164-193.
35. Sack, I., et al., *Non-invasive measurement of brain viscoelasticity using magnetic resonance elastography*. NMR Biomed, 2008. **21**(3): p. 265-71.
36. Anssari-Benam, A., D.L. Bader, and H.R. Screen, *A combined experimental and modelling approach to aortic valve viscoelasticity in tensile deformation*. J Mater Sci Mater Med, 2011. **22**(2): p. 253-62.
37. Klatt, D., et al., *Noninvasive assessment of the rheological behavior of human organs using multifrequency MR elastography: a study of brain and liver viscoelasticity*. Phys Med Biol, 2007. **52**(24): p. 7281-94.
38. Alastruey, J., et al., *Pulse wave propagation in a model human arterial network: Assessment of 1-D visco-elastic simulations against in vitro measurements*. J Biomech, 2011. **44**(12): p. 2250-8.
39. Zhongkui Wang, L.W., Van Anh Ho, Shigehiro Morikawa, Shinichi Hirai, *A 3-D Nonhomogeneous FE Model of Human Fingertip Based onMRI Measurements*. IEEE Transactions on Instrumentation and Measurement, 2012. **61**(12).
40. Girnyk S., B.A., Barannik E., Tovstiak V., Marusenko A., Volokhov V., *The Estimation of elasticity and viscosity of soft tissues in vitro using the data of remote acoustic palpation*. Ultrasound in Med. and Biol., 2005. **32**(2): p. 211-219.

41. Vena, P., D. Gastaldi, and R. Contro, *A constituent-based model for the nonlinear viscoelastic behavior of ligaments*. J Biomech Eng, 2006. **128**(3): p. 449-57.
42. Zhang X. , K.R., Greenleaf J. F. , *Viscoelasticity of lung tissue with surface wave method*. IEEE International Ultrasonics Symposium Proceedings 2008.
43. Catheline, S., et al., *Measurement of viscoelastic properties of homogeneous soft solid using transient elastography: An inverse problem approach*. The Journal of the Acoustical Society of America, 2004. **116**(6): p. 3734.
44. Levental, I., P.C. Georges, and P.A. Janmey, *Soft biological materials and their impact on cell function*. Soft Matter, 2007. **3**(3): p. 299.
45. Egorov, V., H. van Raalte, and V. Lucente, *Quantifying vaginal tissue elasticity under normal and prolapse conditions by tactile imaging*. Int Urogynecol J, 2012. **23**(4): p. 459-66.
46. Walker, D.C., Brown B.H., Blackett A. D., Tidy J . S, Mallwood R. H., *A study of the morphological parameters of cervical squamous epithelium*. Physiological Measurement. **24**: p. 121–135.
47. Kieweg, S.L., et al., *Gravity-induced coating flows of vaginal gel formulations: In vitro experimental analysis*. Journal of Pharmaceutical Sciences. **93**: p. 2941-2952.
48. Hu, B. and S.L. Kieweg, *The effect of surface tension on the gravity-driven thin film flow of Newtonian and power-law fluids*. Computers & Fluids, 2012. **64**: p. 83-90.
49. Kheyfets, V.O. and S.L. Kieweg, *Experimental and numerical models of three-dimensional gravity-driven flow of shear-thinning polymer solutions used in vaginal delivery of microbicides*. J Biomech Eng, 2013. **135**(6): p. 61009-14.
50. D.J., A., *Elementary Fluid Dynamics*. 1990, New York: Oxford University Press.
51. Diez, J.A. and L. Kondic, *Computing Three-Dimensional Thin Film Flows Including Contact Lines*. Journal of Computational Physics, 2002. **183**(1): p. 274-306.
52. Zhang, W., H.Y. Chen, and G.S. Kassab, *A rate-insensitive linear viscoelastic model for soft tissues*. Biomaterials, 2007. **28**(24): p. 3579-86.
53. Kieweg, S.L., *Mechanical Analysis of Vaginal Gels Intended for Microbicide Application*. Department of Biomedical Engineering.2005, Duke University.